Coherent Spatial and Temporal Combining of Femtosecond Fiber Lasers at the Storage Energy Limit Enabling High-Power Drivers of Laser-Plasma Accelerators and Other Secondary Radiation Sources

by

Alexander Ward Rainville

A dissertation submitted in partial fulfillment
of the requirements for the degree of
Doctor of Philosophy
(Electrical and Computer Engineering)
in the University of Michigan
2023

Doctoral Committee:

Professor Almantas Galvanauskas, Chair
Professor Steven Cundiff
Research Scientist John Nees
Professor Theodore Norris
Professor Alexander Thomas

"The research worker is sometimes a difficult person because he has no great confidence in his opinions, yet he also is sceptical of others' views. This characteristic can be inconvenient in everyday life."

W.I.B. Beveridge, *The Art of Scientific Investigation*

Alexander Ward Rainville
rainvila@umich.edu
ORCID iD: 0009-0002-9866-8537

DEDICATION

This thesis is dedicated to my parents.

ACKNOWLEDGMENTS

There are many I must thank for supporting, advising and helping me throughout my PhD journey. Of course my parents, to whom this thesis is dedicated: my mom for constant, unwavering support, and my dad for allowing me to take things apart from the age I could hold a screwdriver and for the instilling in me an intuitive understanding of the physical world.

I must acknowledge my research advisor and mentor Professor Almantas Galvanauskas. Your passion for physics, innate curiosity and indefatigable drive have made me into the researcher I am today. Additionally, as an editor and reviewer who gives honest feedback and pushes for clear and accurate explanations, you have raised the quality of my presentations and written work and taught me how best to present my ideas and contributions. Thank you.

It may seem that academic research suffers from experienced students being replaced by inexperienced ones and it is true, especially on complicated projects, this can be frustrating. A major (and possibly overlooked) benefit of this cycle comes from progressing from a naive first year, receiving advice and instruction from senior students, to accidentally becoming a mentor yourself, all the time growing with those in the lab. I am especially thankful to Trey Ruppe, Hanzhang Pei and Siyun Chen for providing their knowledge, guidance, wisdom and humor while I surreptitiously became a mentor to others. Lauren Cooper, Christopher Pasquale, Tayari Coleman, Yanwen Jing and Yu Bai, I hope that my mentorship has been as useful to you as theirs was to me; I have learned much from you as well and am eager to see your work going forward. To those who started in the research group with me—some of whom have managed to escape before me—Mathew Whittlesey, Yifan Cui and Mingshu Chen, thanks for the commiseration and collaboration over the last 5.5 years. To Nicholas Peskosky—your energy, experimental grit and refusal to accept setbacks brought a new dimension to our lab; some of my favorite work has been our joint experiments.

Of course, those friends outside the laboratory make the time spent in a PhD less difficult. I must acknowledge Brandon Russell, with whom I spent the pandemic putting thousands of miles on our bikes, for being a great friend and roommate in more ways than words can describe. Colten Peterson, with whom I had and will have many adventures, thanks for always having my back and forcing me relax when I felt I should be working. Laura Andre, thank you for being the one who convinced me to come to UM and being a friend since then; your upbeat attitude and enthusiasm are always welcome.

TABLE OF CONTENTS

LIST OF FIGURES

FIGURE

LIST OF TABLES

TABLE

LIST OF ACRONYMS

ADC analog-to-digital converter

AOM acousto-optic modulator

AR anti-reflection

ASE amplified spontaneous emission

BBO beta-barium borate

CBC coherent beam combining

CCC chirally-coupled-core

CPA chirped pulse amplification

CPSA coherent pulse stacking amplification

CPS coherent pulse stacking

CSC coherent spectral combining

CW continuous-wave

DAC digital-to-analog converter

DCF double-clad fiber

DFG difference-frequency generation

DOE diffractive optical element

DPA divided-pulse amplification

EDPA electro-opticially controlled divided pulse amplification

EOM electro-optic modulator

FPGA field-programmable gate array

FWHM full-width at half-maximum

GDD group-delay dispersion

GMNA gain-managed nonlinear amplification

GTI Gires-Tournois interferometer

HOMs higher-order modes

HWP half-wave plate

HR high-reflection

LOCSET locking of optical coherence via single-detector electronic-frequency tagging

LMA large mode area

LPA laser-plasma accelerator

LWFA laser wakefield acceleration

MFD mode-field diameter

MOPA master-oscillator power-amplifier

MPE multi-pass extraction

NA numerical aperture

Nd:Glass neodymium-doped glass

NRMSE normalized RMS error

OAP off-axis parabola

OPCPA optical parametric chirped pulse amplification

PBS polarizing beam splitter

PCF photonic-crystal fiber

PID proportional-integral-derivative

PM polarization-maintaining

PR partial-reflector

PSP pulse shape parameter

RF radio-frequency

RMS root-mean square

SHG second harmonic generation

SMF single-mode fiber

SPGD stochastic parallel gradient descent

SPM self-phase modulation

SSG small-signal gain

TFP thin-film polarizer

TIR total internal reflection

Ti:Sa titanium-doped sapphire

TMI transverse-mode instability

Tm:YLF thulium-doped yttrium lithium fluoride

WPE wall plug efficiency

Yb:YAG ytterbium-doped yttrium aluminum garnet

ABSTRACT

This work demonstrates, for the first time, simultaneous operation of coherent beam combining (CBC) and temporal combining at the amplifier saturation limit. The techniques described and implemented in this thesis will enable fiber array size reduction and thus practical laser sources providing joule-level energies at 10–100 kHz repetition-rates, suitable for future laser-matter interaction research and applications. Through the use of coherent pulse stacking amplification (CPSA) at the storable energy limit, 9.5 mJ is extracted from a single fiber and temporally combined into a 345 fs pulse with 58% efficiency, achieving a record-high single-fiber energy in a femtosecond pulse. Through careful understanding and modeling of amplifier extraction the nonlinear phase accrual is minimized, and the effects of saturation in the 81-pulse burst are investigated and controlled. Further temporal efficiency increase will require control of individual pulse spectrum using a fast electro-optic modulator (EOM), and should increase stacked pulse energy even further while maintaining high-fidelity pulse compression. All techniques discussed are applicable to longer pulse bursts and future fibers that may store 20-50 mJ or more, energies far outside the operation regime of any other time-domain techniques.

Output energies are scaled up to 25 mJ by implementing a coherent beam combination (CBC) array of 4 spatially-combined amplifiers. The spatial combining efficiency, critical for future high-efficiency sources, exceeds 90% when the beams are phase-locked with a stochastic parallel gradient descent (SPGD) algorithm. The alignment procedures and tolerances for achieving this high efficiency are discussed, along with the future implementation of spatial and temporal auto-alignment for larger arrays. The 25 mJ burst is temporally combined with 70% efficiency while maintaining ultrashort pulses, showing that CBC does not adversely impact CPSA efficiency. Incomplete CBC phase stabilization is shown to degrade temporal combining stabilization slightly at the 7 mJ

/ channel amplifier set-point; rep-rate scaling and better fiber thermal management will be required in future designs to improve stabilization. This experiment achieves the highest per-channel energy in a spatio-temporal fiber-array system and provides important information for ongoing work on extending the array to 12 amplifiers capable of 100 mJ energies, and beyond, and for future power scaled systems as well.

The 4-channel CBC and CPSA system was used for the first demonstration of neutron generation from a fiber laser driver by irradiating free-flowing liquid streams of deuterated water. Late-time stream dynamics are imaged with a novel backlight probe beam that provides unique temporal resolution at delays approaching 1 ms. Neutron yield can be increased by increasing on-target energy and pulse repetition rate. In the future, high-brightness laser-driven sources applicable to medical and imaging fields may be available with this technology. Further integration of the computer-controlled probe with neutron statistics and high rep-rate operation will allow for active target and laser optimization using machine-learning, an important step for next generation high-rep rate science.

CHAPTER 1

Introduction and Background

1.1 Overview and Motivation

Since its invention 62 years ago the laser has become ubiquitous, a far cry from what it's inventor, Theodore Maiman, once called "a solution seeking a problem." That first red ruby rod has expanded to an eclectic mix of gain media from meter-long gas filled tubes to micron-long semiconductor heterostructures providing wavelengths from x-ray to terahertz and outputs as short as a single electric field oscillation to almost noiseless continuous-wave (CW) operation. The laser truly has become a solution for many problems from medical imaging to surgery, rangefinding, data storage and retrieval, cutting and welding, biomonitoring—the applications are almost endless.

Certain lasers output intense, short bursts of light that are measured in picoseconds to femtoseconds or 10^{-12} - 10^{-15} s. Pulse durations on this order are termed "ultrashort" and are the fastest man-made events, matching the dynamics of atomic transitions. While the energy of most laser pulses is meager compared to that of, for example, the 150 J carried in a 100 MPH baseball pitch, delivering this energy in femtoseconds leads to peak powers in excess of 10^{15} W, 12 orders of magnitude more power than the average toaster. Additionally, as lasers create highly directional, coherent beams their output can be focused to spots on the order of their wavelength, 10-20x smaller than human hair, leading to focal plane intensities up to $10^{22}\,\mathrm{W}\cdot\mathrm{cm}^{-2}$. In these foci the electric and magnetic fields reach levels that rip apart atoms, accelerate the subatomic particles to near the speed of light, and cause atomic nuclei to fuse together, among other effects. Beyond the

physics of the laser-matter interactions, ultrashort pulses are used in machining and surgery where they create very clean, precise ablative spots and in generation of ultrashort secondary radiation, useful for imaging and material interrogation.

Many lasers produce ultrashort pulses, but those that can achieve the Joule level of energy or higher are limited to repetition rates (laser shots in a given time frame) measured in shots/min or at best 1 shot/second. This was sufficient for many decades but it has become clear that laser technology must eventually provide 1000-100,000 shots/second (1-100kHz) to fully realize the potential of both scientific study and applications of laser matter interactions. This scaling requires new laser technology and is an active area of research across the world. Perhaps the most promising new technology is fiber-laser arrays, which will provide ultrashort, high-power pulses generated in highly efficient laser media. This thesis covers my work in coherent temporal and spatial combination of fiber lasers for future high-energy sources, demonstrating record levels of energy per fiber and the first system working at the amplifier extractible energy limit. This system, along with a novel fiber-integrated optical backlight diagnostic, is used for the first demonstration of neutron generation from a fiber laser. The work presented here provides a roadmap to high-energy, high-power laser sources of the future.

1.2 Some Applications of High-Power Ultrashort Pulses

1.2.1 Relativistic Laser Matter Interaction Regime

When dealing with laser matter interactions it is useful to have a normalized measure of laser strength so lasers of different pulse durations, wavelengths and energies and targetry with different focusing geometries can be compared. This can be done by normalizing the quantity eE, the work done by the laser electric field E on an electron of charge e over the distance of a meter, by the electron rest energy $m_e c^2$ and then scaling to the laser wavelength $\lambda/2\pi$. When the resulting parameter, known as a_0, is unity the laser electric field can accelerate an electron to a kinetic energy equal to its rest energy in the span of a laser wavelength.

$$a_0 = \frac{eE}{(m_e c^2)} \times \frac{\lambda}{2\pi} = \frac{eE}{m_e \omega c} \approx 8.5{\times}10^{-10} \times \lambda[\mu\text{m}] \times \sqrt{I_0[\text{W} \cdot \text{cm}^{-2}]} \tag{1.1}$$

Gaining this energy means the electron is traveling at ∼95% the speed of light, making it a relativistic particle. For this reason $a_0 \geq 1$ is usually referred to as the "relativistic regime" of laser intensities, with $a_0 < 1$ considered non-relativistic [1]. Thus this parameter not only allows for comparison of focal plane laser strength but gives information on the relativistic nature of the interaction.

1.2.2 Laser Wakefield Acceleration

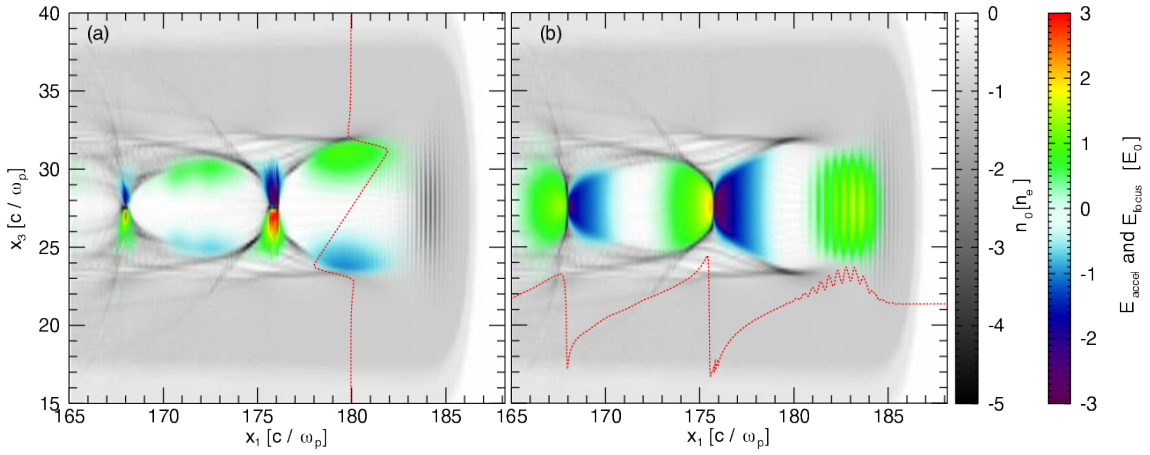

Figure 1.1 : Simulation of a laser wakefield for $a_0 > 1$ showing electron density in grey and field structure in blue-red for (a) transverse focusing fields and (b) longitudinal accelerating fields. The red dashed line shows a line-out of the fields in both cases. Reprinted from [2].

Intense laser pulses focused to small spots have large electric and magnetic forces, that, when traveling through plasma, push light charged particles such as electrons out of the way leading to areas of alternating high and low electron density. The electron density gradients induce electric field gradients that in turn serve as accelerating structures for some electrons that get trapped behind the laser pulse. The electric field gradients in these configurations can exceed 100 GeV · m^{-1} and have been used to accelerate electrons up to 8 GeV in 20 cm of plasma [3] in what is termed

laser wakefield acceleration (LWFA), as the electrons "surf" the wake behind the pulse similar to a surfer on a wave. The energy gain in such a small length excites those in the particle accelerator community who are used to energy gains of only $10\,\mathrm{MeV} \cdot \mathrm{m}^{-1}$ in radio-frequency (RF) cavity accelerators; additionally the linear accelerating nature of LWFA means that the particle energy gain is not limited by synchrotron radiation. For this reason considerable work has been done validating technology and physics with the goal of building a linear laser-plasma accelerator (LPA) which promises to be an order of magnitude smaller than conventional RF accelerators and provide much higher energy particles [4, 5].

In general the magnitude of a_0 distinguishes two regimes of LWFA. At lower focal intensities where $a_0 < 1$ the induced wake varies sinusodially behind the pulse and for acceleration requires external injection of electrons. For $a_0 > 1$ the interaction is nonlinear and leads to what looks like a "bubble" of positive charge following the pulse, as shown in Fig. 1.1. In this regime electrons blown out by the laser pulse can find themselves trapped in the wake (self-injection) with the downside that there is no control over the accelerated electrons leading to a large energy and emittance spread of the output beam.

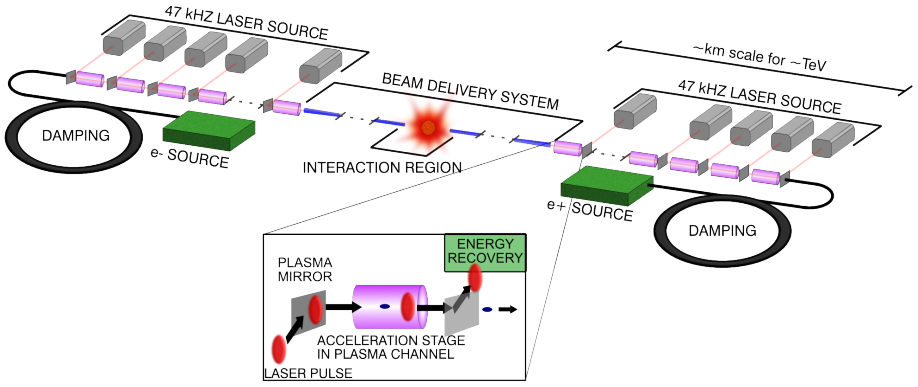

Figure 1.2 : Example TeV e^{-}-e^{+}collider. Reprinted from [5].

Fig. 1.2 shows a proposed design for a TeV center-of-mass electron-positron (e^{-}-e^{+}) collider [5]. Each stage is designed for 5 GeV energy gain though a plasma waveguide driven by a 50 TW (6.5 J, 135 fs) laser pulse with $a_0 \approx 1$ and requires 200 laser drivers, with the ability to upgrade to higher particle energies with more lasers. The critical parameter, however, is that this system must

run at 47 kHz or above to generate enough e^- and e^+ flux (particles/second) on target for meaningful experiments. This is 300 kW of average power per laser, much beyond the current technology.

1.2.3 Ultrashort X-ray Generation in LWFA

The transverse fields in LWFA, shown in Fig. 1.1a, cause the electrons to oscillate transversely while they accelerate longitudinally. The transverse acceleration releases bursts of x-rays, termed betatron radiation, which are ultrashort, coherent and of high brightness [6]. These x-rays have been used to create high-resolution 3D scans of biological samples [7] where the resolution is higher than conventional x-ray sources and the dose is lower. Scan times are limited by the laser rep-rate however—the scan in [7] took hours—meaning that for practical applications the laser rep-rate must be scaled.

1.2.4 Ion Acceleration and High-Energy Particle Generation with Lasers

For specific targets or very high a_0 the laser can accelerate ions and initiate processes that liberate energetic neutrons or protons. Ions have high momentum and distinct stopping properties and can be used for cancer therapy [8], while neutrons, due to their neutral charge, can affect the nuclei of secondary atoms for nuclear transmutation or contrast imaging. One application of neutron-induced nuclear transmutation is the generation of radioisotopes used in PET scans, a critical diagnostic technique in nuclear medicine. Currently some of these isotopes are made by colliding accelerated protons or deuterons with liquid or gas targets, necessitating nearby medical cyclotrons while others, such as ^{99}Mo used to make ^{99m}Tc, use the energetic neutrons emitted in research-grade nuclear reactors. Laser-matter interactions are a promising route for generation of energetic neutrons to mimic current ^{99}Mo production and for production of protons and γ-rays that can be used for alternate routes [9]. One benefit of laser-accelerated neutrons is the high directionality that potentially can give higher brightness for less overall flux than a conventional source. Once again, scaling laser rep-rate beyond current technology is critical to making this application practical.

1.3 Key Methods of Ultrashort Pulse Generation and Amplification

1.3.1 The Time-Bandwidth Product

Ultrashort pulses fundamentally require many frequency components due to a manifestation of the uncertainty principle. The shortest pulse duration achievable for a given spectrum is specified with a time-bandwidth product which can be derived using Fourier transforms and by using root-mean square (RMS) power-spectrum $\Delta\nu_{\text{RMS}}$ width and RMS temporal pulse width τ_{RMS} [10].

$$\Delta\nu_{\text{RMS}} \times \tau_{\text{RMS}} = \frac{c}{\lambda_0^2}\Delta\lambda_{\text{RMS}} \times \tau_{\text{RMS}} \geq \frac{1}{2} \tag{1.2}$$

If Eqn. 1.2 is an equality (that is, the minimum product) then the pulse duration is referred to as bandwidth limited and specifying its temporal duration or spectral width is equivalent; often this is used interchangeably. For pulses longer than this minimum product the ratio of the actual duration to theoretical limit can be specified as "times bandwidth limited" as a measure of residual dispersion or other effects.

The temporal duration usually is specified as full-width at half-maximum (FWHM) level instead of RMS, a convention which will be followed in this thesis and notated as τ_{p}. Additionally the spectral width $\Delta\lambda$ will be specified in FWHM which, for the ideally square spectra used, is very close to the edge-to-edge spectral width. Two conversion factors with these definitions and λ_0 =1035 nm may be useful: $\Delta\lambda$ = 10 nm $\leftrightarrow$ τ_{p} = 330 fs and $\Delta\lambda$ = 30 nm $\leftrightarrow$ τ_{p} = 110 fs. For comparison, a Gaussian spectrum centered at 800 nm with a FWHM bandwidth of 10 nm corresponds to a pulse duration of 100 fs.

1.3.2 Mode-locking

Large frequency content is a necessary but not sufficient condition for ultrashort pulses; in addition, there must be a fixed phase relationship between all the frequencies in order to generate pulses.

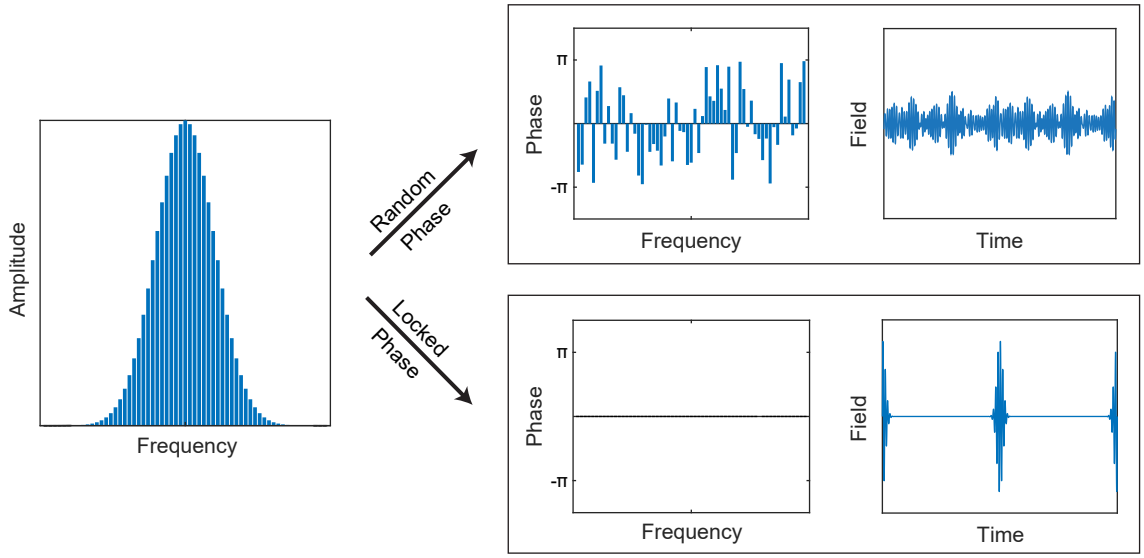

Figure 1.3 : Mode-locking in the spectral domain, where the the same frequency content can form noise or ultrashort pulses depending on the relative phases between the frequency components. In this simulation about 60 modes are used; in a real oscillator the mode number can exceed 10^3.

This is readily understood in the frequency domain where every part of the frequency content can be represented as a sine wave. When the phase of all these waves is random the result is just a superposition of fields that beat against each other. If the phase is fixed then at one point in time all the sine waves peak together, but away from that point they destructively interfere. A laser oscillator with multiple longitudinal modes, gain that can amplify them, and a method of locking the spectral phase is referred to as "mode-locked" and will produce a train of short pulses. The method of locking the phases can be understood in the time domain as a fast switch that allows only a single short pulse to circulate in the cavity, blocking all continuous and long-pulses from being amplified; this has the same effect as forcing the spectral phases to be locked. Most modern mode-locked lasers use the nonlinear refractive index, which has a response time of femtoseconds, to generate the ultrafast switch. This leads to oscillator pulse durations limited only by the gain bandwidth of the laser; for ytterbium-doped fiber this is at minimum 60 fs and for titanium-doped sapphire (Ti:Sa) it can be down to 5 fs [11].

1.3.3 Chirped Pulse Amplification

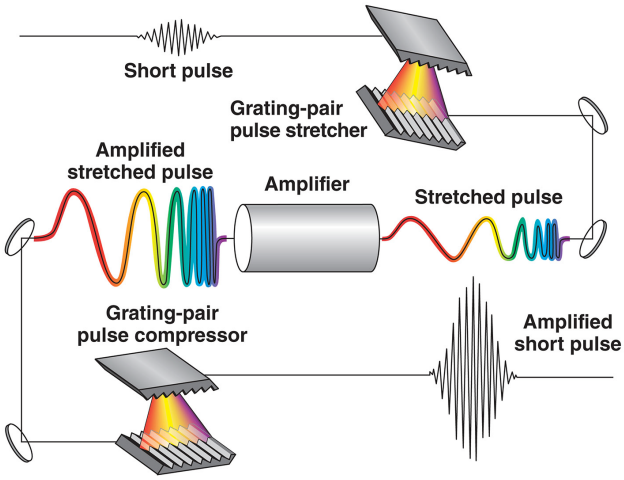

Figure 1.4 : Schematic showing principles of CPA. Reprinted from [12].

Usually the ultrafast output of these mode-locked oscillators contains pJ to nJ of energy, not enough for most applications. Amplification of the pulses generally follows their generation in the oscillator, in a scheme known as master-oscillator power-amplifier (MOPA). A major issue of amplification results from the same reason the pulses are useful: the high peak power. At such short durations the pulses very quickly reach damage thresholds of optical components and powers cannot be increased without transverse aperture scaling of the gain material (increasing the beam area and reducing the peak beam intensity). Historically this put a strong limit on achievable ultrashort laser energies until chirped pulse amplification (CPA), a technique from radar, was applied to optical amplifiers in 1985 [13]. The CPA principle simply involves reduction of the pulse peak power during amplification by lengthening (stretching) the pulse in time rather than in space. After amplification the pulse is made ultrashort again (or compressed) before being delivered to the target or application. Stretching and compressing is done using dispersion, exploiting the fact that ultrashort pulses contain a frequency spread and that optical setups can be arranged to provide varying delay with frequency. CPA typically uses reflective grating structures arranged such that the angular dispersion is coupled to temporal dispersion; depending on the exact structure and the path length difference the devices are called a stretcher or a compressor.

CPA has enabled a massive increase in ultrashort pulse peak powers since 1985 and allowed investigation into new areas of physics. As such CPA and its inventors were honored with a Nobel Prize in Physics in 2018.

1.4 Average Power Limitations of Current High-Energy Lasers

Current laser systems providing above a TW of peak power can use traditional solid-state gain media such as neodymium-doped glass (Nd:Glass) or Ti:Sa or use a nonlinear crystal in an optical parametric chirped pulse amplification (OPCPA) configuration [14]. All use CPA and usually amplify pulses from high rep-rate oscillator in a series of amplifiers while downcounting the rep-rate to 1-60 pulses/min at the final amplifier. Solid-state systems have regenerative amplifier(s) and multi-pass amplifier(s) while OPCPA systems replace these with nonlinear crystals that convert pump to signal through a χ_2 nonlinearity such as difference-frequency generation (DFG). Generally some type of dispersion management though (dazzler and/or mazzler) are used to optimize pulse duration at focus and deformable mirrors are used to optimize the beam profile. These PW-class systems are truly extraordinary—they usually fill whole cleanrooms, use compressor gratings on the meter scale, require amplifier crystals $>$10 cm in diameter and produce focused intensities approaching $10^{23}\,\mathrm{W}\cdot\mathrm{cm}^{-2}$.

The first PW demonstration was with a Nd:Glass laser at LLNL in 1996 with a pulse duration of 450 fs and 660 J [16] and Nd:Glass is still in use in some high-energy systems, including the Texas Petawatt Laser (186 J / 167 fs) [17]. The low thermal conductivity of glass requires that these large lasers only be shot 1/min maximum, enough time for the laser to fully cool, though recent advances in direct-diode pumping have achieved operation up to 10 Hz at 200 J in a highly specialized system [18]. The gain bandwidth of Nd:Glass only supports 450 fs pulses after large amplifications, which can be optimized slightly by using several different types of glass substrates (as in Texas PW Laser), requiring Nd:Glass lasers to have very high pulse energies to reach the PW regime. In contrast, Ti:Sa lasers have very broad bandwidth [19] allowing for 20-30 fs pulses

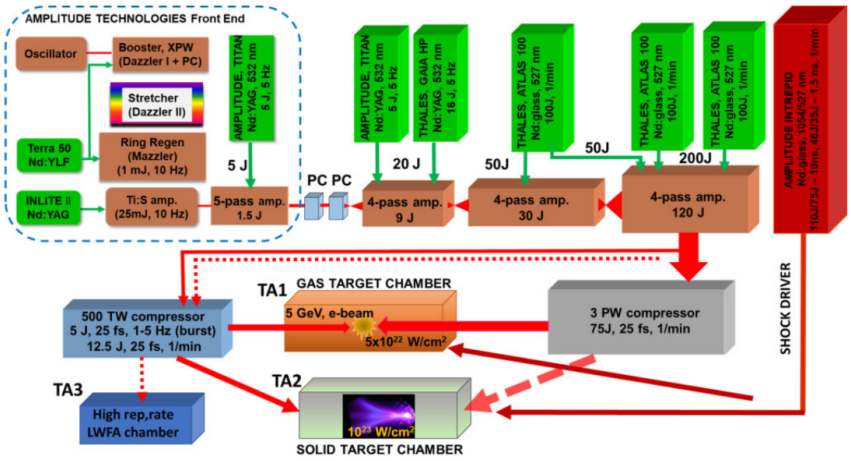

Figure 1.5 : The ZEUS Laser system at University of Michigan, designed around Ti:Sa laser amplifiers pumped with Nd:Glass lasers and specified to provide a 3 PW pulse at 1 shot per minute. Reprinted from [15].

after large amplification. Due to the short pulse duration the pulse energy to reach a PW is much lower than Nd:Glass, and this, along with the excellent thermal properties, means Ti:Sa dominates the PW-class laser field. Ti:Sa is limited by the available pumps [20], as the upper-state lifetime of 3.2 µs is very short and the quantum defect is large (32%) the pumps need to be high energy (10-100 J) in nanosecond pulses at 430-560 nm. The only lasers that can provide this are frequency doubled ytterbium-doped yttrium aluminum garnet (Yb:YAG) and Nd:Glass, both of which have serious heating issues – Nd:Glass, as covered above, can only run 1-6 shots/min at these energies; Yb:YAG can do up to 5 Hz reliably but provides lower energies. Heating of the Ti:Sa crystal itself is also a concern at high energies and as such complicated cooling is often employed, including with modifying by amplifiers such that helium can be flowed between thin plates of the crystal [21, 22]. Transverse amplified spontaneous emission (ASE) in the Ti:Sa crystal was, until recently, a strong limit on large final amplifier crystals but this problem has been solved by surrounding the crystal in a index matching absorbing material [23]. The highest rep-rate available for a PW system is currently the 1 Hz BELLA laser at Lawrence Berkeley National Lab – even at 40 J and 30 fs the average power is still only 42 W [24]. Progress on constructing a new 10 Hz, 1 PW laser is ongoing at ELI in the Czech Republic; this laser is based on direct-diode pumping Nd:Glass pump

lasers and using a multiple-thin slab architecture for the Ti:Sa laser crystal. If successful, the laser will be able to provide 300 W of average power at 1 PW [18].

1.4.1 Electrical Efficiency of High-Power Lasers

An important parameter for laser systems is the wall plug efficiency (WPE), defined as the ratio of output optical power to input electrical power. For overall laser systems this number ranges from 50% down to $\ll$1%. The best estimates for WPE of Ti:Sa lasers is around 0.1% [25], meaning that scaling a single moderate energy 6.5 J / 130 fs laser system to 47 kHz for the LPA driver shown in Fig. 1.2 (assuming the pump technology existed) would require 300 MW of electrical power, 6 times the amount of power produced by the University of Michigan campus power plant.

The most efficient laser media have: (1) pump bands in the range of high-power laser diodes, for "direct-diode" pumping and (2) low quantum defect, allowing for most of the pump light to be converted to signal. Ti:Sa unfortunately fails on both of these fronts. As a note, there has been some promising work on direct-diode pumping Ti:Sa at 450 nm but the pumps are low power ($<$100 W), run CW, and parasitic absorption in the crystal can decrease efficiency further [26].

1.5 Laser Technology Solutions for Scaling Average Power

Clearly new technology is needed for high-energy, high-average power lasers systems. Whatever approach is settled on fundamentally needs high WPE and large enough bandwidth for ultrashort pulses with good thermal properties. Three potential options are presented here.

1.5.1 Yb:YAG Thin Disk Technology

Thin disk lasers solve the heat extraction of solid-state crystals by reducing the longitudinal dimension and adding cooling on one face of the crystal. This is achieved by using a thin crystal that has an anti-reflection (AR) coating on one side and a high-reflection (HR) coating on the other. The HR coating side is then thermally bonded to a heatsink that can more efficiently remove heat.

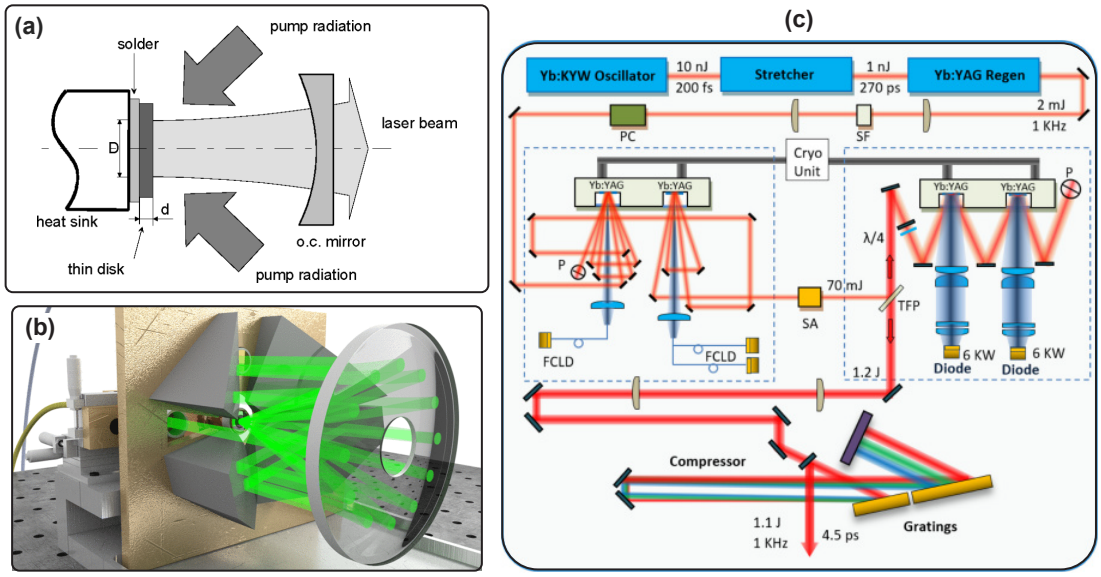

Figure 1.6 : Schematics showing: (a) the basics of a thin-disk amplifier or oscillator [27], (b) a 3D rendering of the multi-pass signal geometry [28], and (c) the schematic of the laser system used to achieve 1.1 J energies at 1.1 kW average power [29]. The final amplifier in (c) is pumped with 380 µs, 940 nm pump pulses of 6 kW power which are re-imaged once onto the 30 mm x 30 mm x 2 mm 3%-at Yb:YAG crystal. Liquid nitrogen cooling is used on the final 4 amplifiers.

Due to the small crystal length extraction of signal energy and absorption of pump requires the use of complicated multi-pass configurations. Yb:YAG is frequently used as a laser medium because of the good thermal properties, low quantum defect and availability of high-power pump diodes in the absorption region. However, the gain bandwidth is small, leading to pulses that are in the few picosecond range when highly amplified. The highest energy result to date is 1.1 J at 1 kHz (an average power of 1.1 kW) but with pulse duration of 4.5 ps [29]; the optical-to-optical efficiency of the final amplifiers was 36% but the overall WPE was not reported (pump diodes will reduce this by at least half). In theory use of nonlinear compression from self-phase modulation (SPM)-induced spectral broadening can be used to decrease the pulse duration, but currently methods do not exist that can reliably handle this much average power or energy.

1.5.2 Large-Aperture Thulium:YLF

Nascent research on thulium-doped yttrium lithium fluoride (Tm:YLF) suggests it may be a good candidate for a solid-state style laser amplifier at high energy and average power. Tm:YLF has emission centered around 1.9 µm with enough bandwidth for 100 fs pulses, a two-photon absorption process that allows for efficient pumping with diode lasers at 795 nm, and good thermal properties [30]. Characterization of the energy storage of a 35 mm-thick 6%-at doped Tm:YLF has shown 108 J extractible in a 3 ms long pulse after the medium has been inverted with a 40 ms pump pulse [31].

Efficient extraction of the energy stored in the laser crystal requires conversion of all the available upper-state atoms to signal energy through stimulated emission before spontaneous and non-radiative decay effects degrade the population inversion. In some materials this can be done with a single pulse, passing it though the inverted medium many times in a period shorter than the upper-state lifetime, as in a bowtie or regenerative amplifier. In Tm:YLF the saturation fluence is $21.6\,\mathrm{J}\cdot\mathrm{cm}^{-2}$, at least two times higher than the damage threshold, meaning effective single-pulse extraction cannot occur before the laser crystal is damaged. Transverse aperture scaling of the laser crystal will increase the achievable pulse energy by lowering the pulse fluence but will also increase the stored energy, keeping efficiency constant. The proposed regime of operation uses multiple pulses, each with a fluence below damage threshold, but with an integrated fluence large enough to saturate the medium. This is uniquely available in long upper-state lifetime materials as > 10 pulses must be used before the upper-state decays—this would require 3 MHz operation for Ti:Sa but only requires 700 Hz in Tm:YLF. The work on Tm:YLF refers to this operation regime as multi-pass extraction (MPE); the physical principle, however, is the same as the efficient conversion of pump to signal power in high-rep rate fiber lasers, the difference being that the intended purpose of MPE is to circumvent amplifier damage thresholds while maintaining efficient operation.

Use of a MPE burst containing 102 pulses/upper-state lifetime (6.8 kHz) has been shown to generate 19% optical-to-optical efficiency with a pump power of 18.2 kW [31]. The pulse energy in

this experiment is not explicitly mentioned but can be calculated from the provided data to be about 1.9 J. Scaling energies further would require increasing the crystal transverse dimension, leading to the full laser concept known as big-aperture thulium (BAT) [32]. However, much work has to be done to extend these results to bandwidth appropriate for ultrashort pulses and to proper CW pumping regimes (all current experiments have been done using 40 ms pump pulses). Additionally, while the reported optical-to-optical efficiency of 19% is very high for solid state lasers, taking into account other efficiency losses the overall system WPE will likely be lower than desired.

From an applications standpoint 1.9 µm laser has a more than twice higher a_0 than an equivalent intensity laser at 800 nm leading to stronger interactions at focus. Additionally the wavelength scaling changes the target dynamics, e.g. the plasma frequency in gas targets and the bubble size in LWFA. These can be both beneficial or detrimental and depend on the experiment.

1.5.3 Coherent Beam Combination of Fiber Lasers

Yb-doped fiber lasers already provide very high average powers with high WPE in the CW regime, providing output powers up to 100 kW at 50% WPE demonstrated [33]. The gain bandwidth allows for sub-100 fs pulses which, if proper techniques are used, can be preserved even at high levels of system gain [34, 35]. The low quantum defect of 6% or 12% (depending on the 976 nm or 915 nm pump band) leads to relatively low heat generation, and the small cylindrical geometry (most single-mode fibers have $<$1 mm diameter) gives a large amount of surface area to volume, allowing for efficient heat extraction even with the low thermal conductivity of glass. The long pump-signal interaction lengths provide high absorption and, along with pump bands in the region of high-WPE diode pumps, WPE efficiency can be higher than any other laser technology. Monolithic integration is another major benefit of fiber lasers, as common optical components such as polarizers, EOMs, AOMs and even pump coupling optics can be integrated into fusion-spliceable packages which eliminate alignment. The major drawback is the limited energy that can be extracted from a fiber using CPA which, for reasons that will be covered later, is a fraction of the stored energy.

This can be overcome by using coherent beam combining (CBC), a brightness scaling technique based on constructively interfering geometrically overlapped optical beams. CBC can be thought of as a type of transverse aperture scaling, analogous to how a solid-state gain crystal is made wider to access more inverted atoms to extract more energy. CBC can be broken down into two main categories: filled aperture and tiled aperture [36, 37] which both produce stable, locked beams in the far field. Filled aperture combining requires the beams to also be overlapped in the near field, and usually is done on cascaded beamsplitters while tiled aperture uses the multiple beams to form a near-field array that propagates to a single beam in the far-field as a type of plane-wave synthesis. The discrete fill factor of the near-field beams in tiled aperture adds side-lobes in the far field, limiting combining efficiency. Other modalities of coherent combining exist including coherent

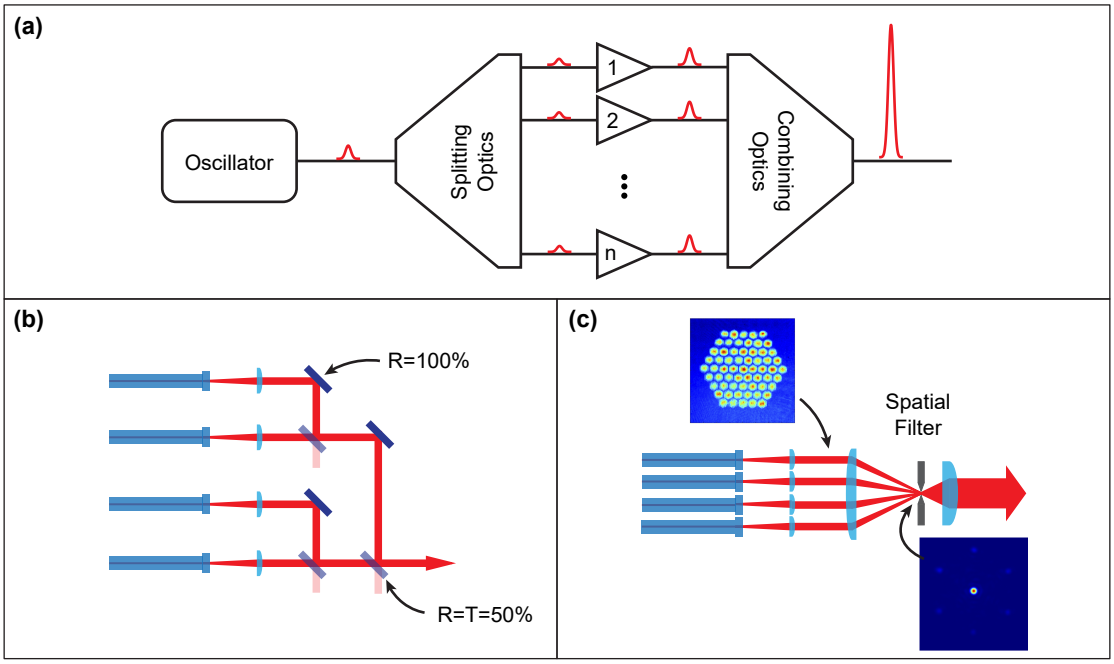

Figure 1.7 : Coherent beam combining principles: (a) General system design, which may include a pulse stretcher and compressor for CPA (omitted), (b) binary tree combining on beamsplitters, an example of filled aperture combining where the beams are overlapped in the near and far field, and (c) tiled aperture combining using a hexagonal near field array. In (c) spatial filter is required to remove the far-field side lobes created by the incomplete fill factor. Examples (b) and (c) modified from [38]; beam profiles in (c) from [39].

spectral combining (CSC) which synthesizes different spectral components before combining them on, for example, a dichroic mirror. This can add more bandwidth and thus decrease pulse duration

but also has additional challenges with amplification and compression [40].

Thus CBC of fiber lasers achieves the two objectives needed for next generation high rep-rate laser sources: high WPE and large enough bandwidth for 100 fs pulses. However, there is fundamental issue: traditional CPA in fibers is limited to a few percent of the fiber stored energy (practically about 100 μJ), requiring the array size in Fig. 1.7a to contain 10^4-10^5 fibers to reach 10 J of output energy. If the full energy of the fiber could be used the array sizes could be reduced to $\sim 10^3$, a much more achievable size. For CBC of fiber lasers to achieve its potential the limitations on stored energy must be understood and overcome.

1.6 Limits on Single-Pulse Extraction of Fiber Stored Energy

The guided-wave propagation in fiber allows for long pump-signal interaction lengths but also leads to large accrual of nonlinear phase due to self-phase modulation (SPM) which, in CPA systems, at first adds to the phase that must be compensated when compressing the pulses. This phase follows the intensity profile of the pulse and deviates from the compressor compensatable quadratic and cubic phase, adding at first "wings" to the compression and degrading peak power. The general effect of SPM on compression can be seen in Fig. 1.8; above about π the compression begins to degrade quickly. Techniques for maintaining compressible pulses at high phase, such as using a pulse shaper or a parabolic spectrum [41], require very high temporal contrast around the main pulse or risk amplifying pre or post-pulses through a SPM-induced phase grating [42, 43].

Note that as the phase accrual follows the temporal intensity profile (which mirrors the spectral profile of a strongly chirped pulse) the spectrum used matters massively in this calculation. In particular, asymmetric or modulated spectra add phase orders that are hard to compensate in a compressor—π is an approximate, experimental limit below which nonlinear effects will not cause issues.

A simple model can be used to see the limiting effect of SPM on fiber energies. First, the peak phase due to SPM can be characterized in fiber by using the pulse peak power P_0, the nonlinear

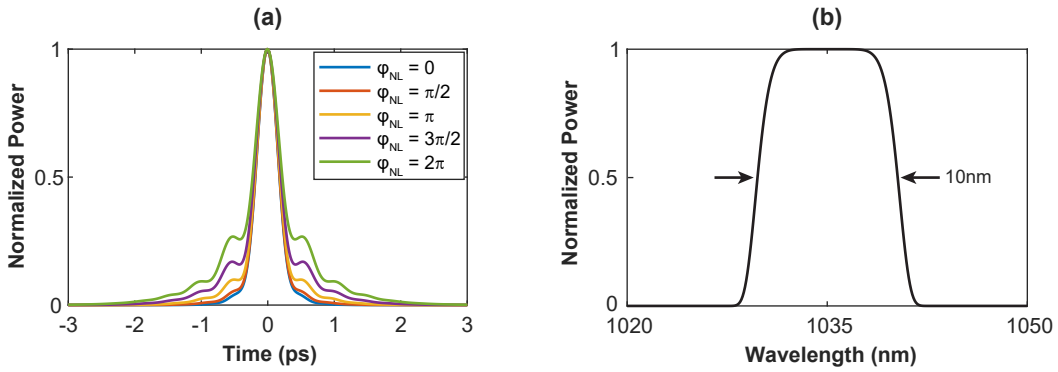

Figure 1.8 : Self phase modulation effects on pulse compression: (a) calculated autocorrelation traces for increasing nonlinear phase on (b) a 10 nm spectrum centered at 1035 nm. The SPM phase is accrued while the pulse is stretched to 1 ns using $\phi'' = -43\ \text{ps}^2$ and the ϕ'' used to compress the pulse is numerically fitted, deviating slightly from $43\ \text{ps}^2$ due to the nonlinearity.

refractive index $n_{2\text{I}}$, the fiber effective mode area $A_{\text{eff.}}$ and the effective length $L_{\text{eff.}}$ [44]. This parameter should should be kept $\leq \pi$ for good compression.

$$\phi_{\text{NL}} = \left(\frac{k_0 n_{2\text{I}}}{A_{\text{eff.}}}\right) P_0 L_{\text{eff.}} \tag{1.3}$$

Second, the stored energy in the fiber can be written in terms of the doping density N_d, the fiber length L and the photon energy at the transition center $\hbar\omega_0$. The overlap of the mode with the doped core is represented by the parameter Γ; for a tightly confined mode smaller than the doped core the product ΓA_{core} reduces to the mode area.

$$E_{\text{stor.}} = \frac{1}{2} N_{\text{d}} L \Gamma A_{\text{core}} \hbar\omega_0 \tag{1.4}$$

This gives the total number of invertible ions in the mode volume times the energy of the transition and is a simple estimate of the maximum stored energy, neglecting effects such as ASE that in practice reduce the value. The factor of $\frac{1}{2}$ comes from the 2-level nature of the transition.

The term $L_{\text{eff.}}$, known in fiber optics as the "nonlinear effective length", expresses the length of fiber with no gain or loss that would impose the same nonlinear phase on a pulse as a longer or shorter fiber with gain or loss, respectively [44]. The definition can be referenced to the input or

output pulse power, leading to some confusion. Here $L_{\text{eff.}}$ will be referenced to the output pulse power, with value < 1 for a fiber with gain, opposite to the normal convention for passive fibers with loss. In a heavily saturated amplifier $L_{\text{eff.}}$ generally requires a numerical model to solve; however, for this simple model exponential gain will be assumed under which $L_{\text{eff.}}$ can be simply written in terms of the pulse gain G and the real fiber length L.

$$L_{\text{eff.}} = \frac{L}{\ln(G)}\left(1 - \frac{1}{G}\right) \approx \frac{4.34L}{G_{\text{dB}}} \tag{1.5}$$

Combining Eqns. 1.3, 1.5 and 1.4 and setting $\phi_{\text{NL}} = \pi$, the extractable percentage of the fiber energy can expressed, where $P_0 \approx E_p\tau_p^{-1}$ is used to relate output peak power to output pulse energy.

$$\%\text{ extr. SPM} = 100 \times \frac{2\lambda_0}{\hbar\omega_0}\frac{G_{\text{dB}}}{4.34N_{\text{d}}L^2n_{2\text{I}}}\tau_{\text{p}} \tag{1.6}$$

This equation is independent of mode area, showing that while scaling the mode area may increase the extracted energy the associated increase in stored energy keeps the fraction of extractible energy fixed. The linear dependence on pulse duration suggests that the longest possible stretched pulses should be used to maximize extracted energy.

It is useful to also understand the stored energy limit from bulk damage, which limits extraction in solid state laser amplifiers. In a similar fashion the damage threshold can be written in terms of the damage fluence $U_{\text{dam.}}$ measured in $\text{J}\cdot\text{cm}^{-2}$ and the pulse duration τ_1 at which the damage threshold is measured. Estimates of $U_{\text{dam.}}$ vary; $800\,\text{J}\cdot\text{cm}^{-2}$ measured at $\tau_1 = 6$ ns is used here [45].

$$\%\text{ extr. Damage} = 100 \times \frac{2}{\hbar\omega_0}\frac{U_{\text{dam.}}}{N_{\text{d}}L}\sqrt{\frac{\tau_{\text{p}}}{\tau_1}} \tag{1.7}$$

A plot showing Eqn. 1.6 and 1.7 plotted vs. pulse duration τ_p is given in Fig. 1.9. The limit $\phi_{\text{NL}} < \pi$ is stricter than damage at all pulse durations and to extract all the stored energy a pulse duration of $>$40 ns is needed. In CPA stretching a 300 fs pulse to 40 ns would require a 3.5 m

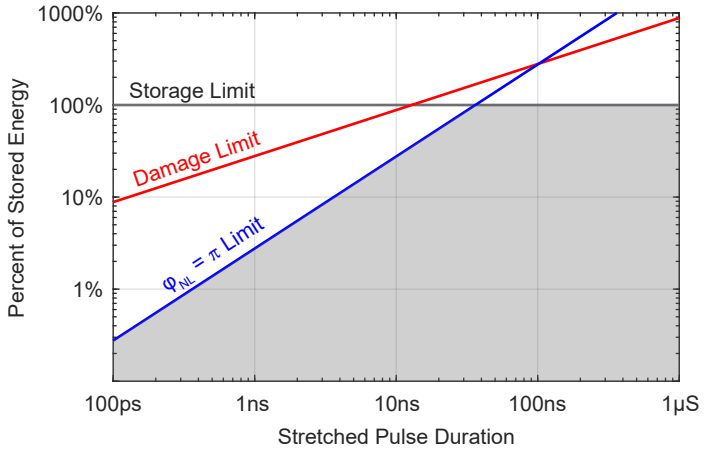

Figure 1.9 : Plot showing the limits on fiber CPA energies. The restriction on single pulse nonlinearity limits the CPA extractible energy to the shaded grey region and bulk damage never forms a limit. The parameters used are: N_d = 5×10^{25} m^{-3}, L = 1 m, λ_0 = 1035 nm, n_{2I} = 2.5×10^{-20} m^2 · W^{-1} and G_{dB} = 17.

grating, 3x what is achievable in manufacturing and 20x what is achievable at reasonable cost. For commercially available gratings stretched pulse durations are around 1 ns, limiting extractible energy to 3% of stored energy. To leverage the high WPE, modularity and great thermal properties of fiber lasers in ultrashort CBC, full use of the fiber stored energy must be realized and will reduce fiber array sizes by 50-100x.

1.7 Temporal Combining for Effective Extension of Pulse Duration

The solution to the limit of single pulses extraction is fundamentally simple: use multiple pulses. Of course, this only helps if the multiple pulses can be combined into one before being used at the application, requiring some type of coherent temporal combining. This then invites the question: how to generate and then combine the multiple pulses? The two main approaches to this question will be discussed here along with a brief review of their development. The first, divided-pulse amplification (DPA), relies on delay lines to generate and then temporally combine the pulses and has seen much development and integration with CBC systems despite its limited

pulse number scaling. The second, coherent pulse stacking (CPS), uses successive pulses from an oscillator that are appropriately modulated such that they temporally combine in cascaded resonant interferometer cavities; when combined with a CPA system it is referred to as coherent pulse stacking amplification (CPSA) and can be scaled to arbitrarily large number of pulses. Modern versions of DPA, inspired by CPSA, also use modulated pulses from an oscillator to generate the burst in what is termed electro-opticially controlled divided pulse amplification (EDPA). Both of these techniques use a burst consisting of multiple chirped pulses to extract energy; in this thesis the term "burst" will be used to refer to the overall set of chirped pulses while the term "pulse" will be used to refer to an individual pulse in the burst. Then for example 10 individual chirped pulses spaced 1 ns apart create a 10 ns long burst. Terms like chirp, spectrum, etc., refer to the properties of a single pulse in the burst. From the point of view of amplifiers, however, the burst can sometimes be treated as a single, long "pulse" as will be done in later chapters.

1.7.1 Divided Pulse Amplification

DPA is a temporal combining technique that combines pulse pairs using a delay line matched to the pulse separation; at the output of the delay line the pulses overlap and combine into a single pulse. Fundamentally then each delay line reduces the overall number of pulses in a burst by ½, requiring use of 2^N pulses for N delay lines. This was first implemented with ultrashort pulses in 2008 using a birefringent crystal stack for the pulse splitting and combination in a double-pass configuration [46, 47].

Despite the same acronym the modern implementation of DPA for chirped pulses in a high-energy fiber system is quite different. Much development has been done since 2008, first moving to chirped pulses with polarizing beam splitter (PBS) splitters/combiners [48], then using different delay lines for splitting and combination [49, 50], followed by integrating with CBC systems [51, 52] using a burst of 4 pulses and 2 delay lines. The current implementation, EDPA, using bursts generated by modulating successive pulses from an oscillator [53], has scaled to 8 pulses and 3 delay lines in an experiment that generated 23 mJ, 674 W pre-compression, with compressibility

to 235 fs [54].

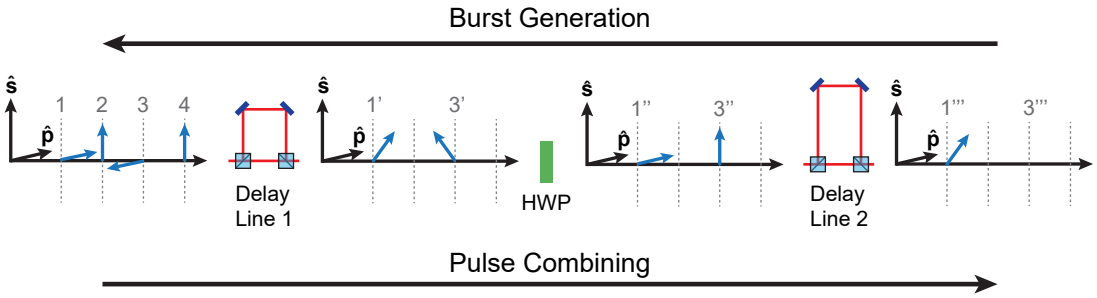

Figure 1.10 : 4 Pulse DPA explanation: traveling left-to-right explains pulse combination while right-to-left explain pulse splitting (modified from [53].) Delay line 1 has length equal to the pulse spacing and delay line 2 has length equal to twice the pulse spacing.

However, DPA is not scalable to the number of pulses needed to access the full energy storable in most large-core fibers; the reason is quite simple but is best illustrated through example. Fig. 1.10 shows a 4-pulse DPA schematic; for EDPA the burst generation is done slightly differently but the principle is the same. For each set of pulses to be combined, for example (1 & 2) and (3 & 4) in the first step, the input pulses must be aligned to either ŝ and p̂ polarizations; this is trivially done using polarization-maintaining (PM) amplifier fibers. The output pulses from the first combining step (1' and 3', respectively) are a vector sum with double the amplitude $A_{1',3'} = (A_{1,2} + A_{3,4})$ and a polarization angle dependent on amplitude ratios $\theta_{1',3'} = \arctan\left(\frac{A_{1,2}}{A_{3,4}}\right)$. For the second combining step the ŝ and p̂ constraint is once again enforced; however, there is only one degree of freedom, the half-wave plate (HWP), to manipulate one polarization angle $\theta_{1'}$ *or* $\theta_{3'}$. By adding freedom on one pulse amplitude the orthogonality of 1' & 3' can be ensured in all cases. This is a general scaling rule in DPA: for 2^N pulses and N delay lines there are only $N-1$ HWP degrees of freedom requiring an additional $2^N - N$ pulse amplitudes for high-efficiency temporal combining. Equal amplitude pulses form a special, symmetric case where the pulse degrees of freedom are not needed.

In saturated amplifiers this becomes a major issue as the pulse amplitude degrees of freedom are required to equalize inter-pulse nonlinear phase; to make matters worse this equalization leads to a strongly varying amplitude shape. Failure to equalize nonlinear phase leads to high degradations in

temporal combining efficiency and pulse compression. DPA does not have the degrees of freedom to compensate nonlinear phase accrual with burst shaping and efficiently combine the shaped burst. This limits temporal combining pulse number, making DPA unsuitable for extracting full storable energy from fiber amplifiers.

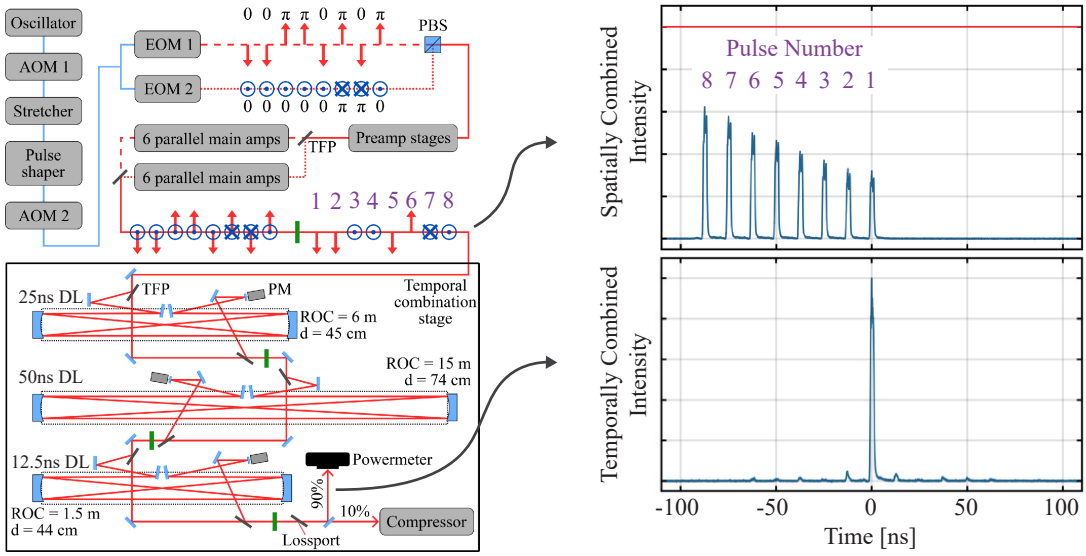

Figure 1.11 : Experimental results from [54] including the pulse bursts before and after temporal combining. The pulse number is notated in purple and the arrows in the diagram notate polarization direction. The green elements are HWPs.

For low pulse numbers and low saturation, situations exist where maintaining efficient temporal combining while matching nonlinear phase is possible. An instructive example is the 23 mJ 8-pulse result from [54]; the setup along with input and output bursts are shown in Fig. 1.11. The individual amplitudes of pulses 1-8 are varied to match their autocorrelation traces to ensure equal nonlinear phase accrual; this burst shape also happens to lead to pulse amplitude ratios that combine well temporally, provided that for the pulse period T_p the first delay line length is $2c \times T_p$, the second delay line length is $4c \times T_p$, and the last delay line length is $c \times T_p$. Critically, however, the energy extracted from each amplifier is only 3.6 mJ; the fiber stored energy is not provided but at least 3x more energy is available from comparable technology. Either way, moving to extracting $>$10 mJ would result in much higher saturation (pulse reshaping), breaking the equilibrium used here, and would probably require at least 3x more pulses to maintain low individual pulse

nonlinearity, reducing the likelihood that an similar equilibrium could be found. Thus this result and the associated DPA technology, while demonstrating a substantial increase over single-pulse extractible energy, will fail to scale to the full fiber potential and therefore will not make a good basis for future high-energy systems.

1.7.2 Coherent Pulse Stacking Amplification

CPSA uses cascaded resonant Gires-Tournois interferometer (GTI) cavities to combine the burst of pulses which does not have the limited degrees of freedom of DPA. Pulse energy is deposited into each cavity depending on the beamsplitter reflectivity, the phase of the pulse circulating in the cavity and the phase of the incoming pulse. In ideal temporal combining of N pulses the first $N-1$ pulses have phases that allow for all their energy to be left in the cavities such that the N^{th} pulse will fully constructively interfere and extract all the energy. This means that no single cavity must be any longer than the pulse separation in the burst and the degrees of freedom are large—the pulse phases, the cavity phases and the cavity beamsplitter reflectivity are all available.

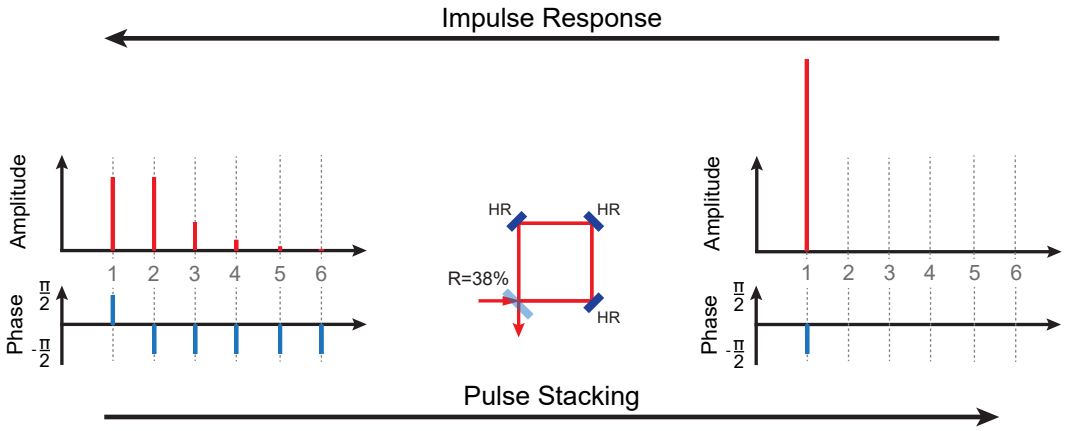

Figure 1.12 : Single cavity coherent pulse stacking example showing the required pulse amplitudes and phases for stacking and how this can be viewed as a reversed impulse response. In this example R=38% is chosen so that the two main pulses are equal amplitude and contain 74% of the overall energy. Only relative phase, not absolute phase matters; the phase shift between reflection and transmission is assumed to be π on the reflected beam. The impulse response is technically infinite, but by the 6^{th} pulse there is $< 1\%$ of the energy remaining in the cavity.

A simple example of a single cavity is given in Fig. 1.12 where the amplitude and phases of

the pulses are shown. To understand the principle of stacking, first consider the impulse response of the cavity as shown by taking the pulse and phase on the right side and propagating it through the cavity. The input pulse partially reflects and partially enters the cavity, after which the pulse circulating in the cavity continues to ring down, transmitting part of its amplitude with additional round trip. This process continues theoretically forever; however, at some point the field remaining in the cavity is negligible—for the example in Fig. 1.12 after 6 total output pulses there is $<1\%$ of the energy still circulating. CPS relies on time-reversing this ring-down and sending it through the cavities. As each successively larger amplitude pulse encounters the field circulating in the cavity it has phase such that it fully constructively interferes and enters the cavity. The final pulse has an opposite phase such that when it interacts with the circulating pulse it constructively interferes to *exit* the cavity. In this example the specific choice of R=38.2% means there are two equal-amplitude pulses that contain 76.6% of the total energy, termed the "stacking burst", and a series of smaller pulses containing the rest, termed the "pre-burst". As more GTIs are added the number of pulses in the stacking burst increases, scaling as $2N + 1$ pulses for N GTIs, and the fraction of energy in the pre-burst decreases. As will be shown later, high stacking efficiency can be maintained using only the main burst (truncating the pre-burst) in many situations.

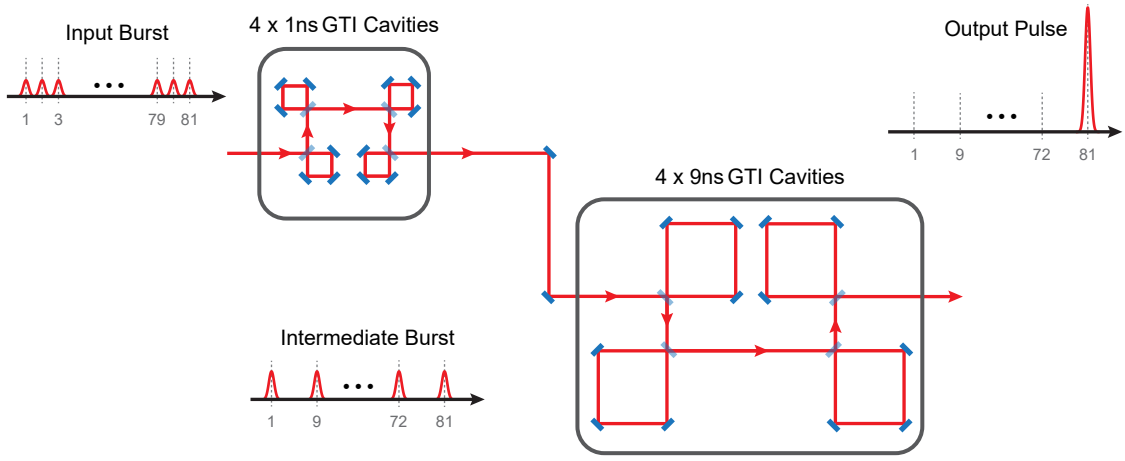

Figure 1.13 : 4+4 Multiplexed GTI example showing stacking of 81 pulses. The pulse spacing is 1 ns which is matched to the delay in the first 4 cavities. The intermediate burst consists of 9 pulses with 9 ns delay, matched to the second set of 4 cavities. The numbers indicate the pulse number relative to the input burst; the amplitude is not to scale.

To stack 50-100 pulses using the equal-length cavity scaling of $2N + 1$ pulses for N cavities would require 25-50 stacking cavities, quite a trade-off to increase fiber energy. Using sets of non-equal cavities allows faster pulse number scaling by stacking subsets of pulses. For example, 4 cavities of length T_{rt} stack 9 equal-amplitude pulses with spacing T_{rt} into a single pulse—if a burst of 81 pulses with individual pulse spacing T_{rt} is incident on this cavity system it will stack to 9 pulses with $9 \times T_{\text{rt}}$ spacing, which can then be stacked by another set of 4 cavities with $9 \times T_{\text{rt}}$ length into a single pulse. In this way only 8 cavities can be used to stack 81 pulses, as shown in Fig. 1.13. This scheme is referred to as "length multiplexing" or just "multiplexing" and the example above would be called a "4+4 GTI multiplex".

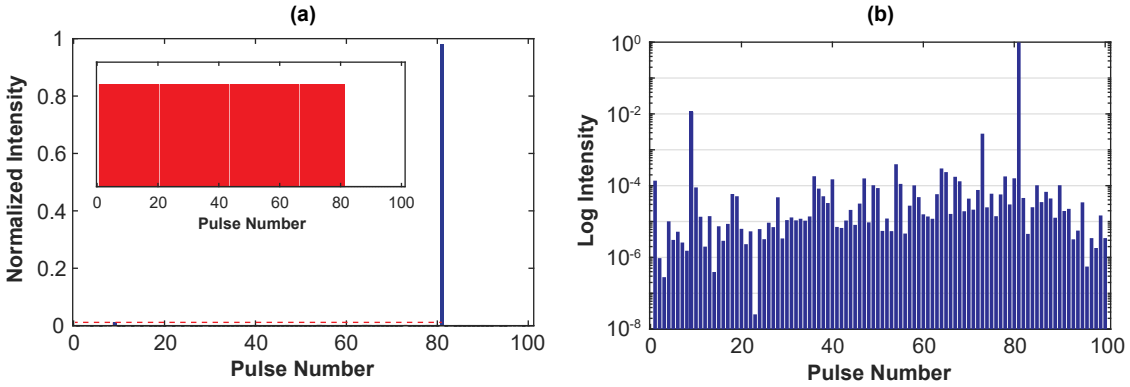

Figure 1.14 : Calculated stacking trace for 81 → 1 pulse stacking in a 4+4 GTI cascade: (a) stacked pulse in linear scale with inset showing input burst, (b) log scale showing pulses that limit pre-pulse contrast. The amplitude of each pulse on the input burst is about 0.0123 if plotted on the stacked pulse scale. The addition of a pre-burst can increase the pre-pulse contrast further.

Though these cavities are initially designed for equal-amplitude pulses they are quite tolerant to amplitude variation in the pulses because of both the large parameter space and the general intolerance to amplitude mismatch in beamsplitter combining (Sec. 3.2.7). Results from simulations confirming this will be shown in Sec. 2.4.4. Even with the beamsplitter reflectivites designed for an equal amplitude burst, free parameters include each individual cavity phase as well as individual pulse phase, which can be changed dynamically during the experiment. Further optimization for a given burst shape using cavity beamsplitters makes the situation even better.

CPSA was first demonstrated in 2015 [55] using 5 pulses (2 equal amplitude, 3 pre-burst) in a

single GTI. The reported stacking efficiency was 97.4% with 15 dB pre-pulse contrast and pulse stacking was shown not to degrade compression compared to the input pulses. The stacking burst was generated by using successive pulses from a mode-locked fiber oscillator and amplitude and phase modulating them with electro-optic modulator (EOM)s; GTI cavity locking was done with the Pound-Drever-Hall method. Multiplexing was first demonstrated in 2016 [56] using 27 pulses in a 4+1 cavity scheme and the extension to 81 pulses in a 4+4 multiplex was demonstrated in 2017 [57], both using stochastic parallel gradient descent (SPGD) as a cavity stabilization method. The first energy-extraction experiment was in 2018 and showed that $81 \rightarrow 1$ temporal combining was feasible [58]. However, this result did not include stabilization, the temporal combining efficiency was low, and the pulse duration was much longer than the bandwidth limit.

1.8 Contributions of this Thesis

This work represents critical progress towards high-energy, high-average power laser systems by demonstrating the first simultaneous spatial and temporal combining with full access to fiber storable energy, achieving 25 mJ spatially combined from four amplifiers with 70% temporal combining efficiency. The use of this first-of-a-kind fiber laser in plasma experiments, combined with a novel target backlight, showcases the capability of CPSA and provides a direct path, in the near future, to a 100 mJ, 1 kW fiber system with only 10-12 parallel amplifiers. In the long term, scaling to a 10 J-class system will only require 10^3 fiber amplifiers—a potential revolution in laser technology.

To achieve high stability and efficiency the single amplifier results were refined utilizing extensive amplifier modeling to understand and minimize nonlinearity, with reduction of optical noise through proper system design and active stabilization. Then, a four-channel CBC array was constructed around this basis, scaling the energy by achieving above 90% combining efficiency at 7 mJ/channel through comprehension and compensation of spatial misalignments and active control of temporal phase drift. Careful design of the stacker and compressor power and energy

handling enabled use of the output of the spatio-temporally combined system for generation of neutrons, a first from a fiber-laser system. A novel off-band, ultrashort target backlight based off fiber technology facilitates high-resolution imaging of the plasma channel at adjustable time delays in excess of 1 ms, viewing target dynamics at ranges previously inaccessible and without contrast-degradation from plasma self-emission. Future work will scale array size to 10 channels for 100 mJ, increase average power to the kW range and decrease pulse duration to 100 fs, further improving average and peak power for next-generation laser systems.

1.8.1 Relationship to Others' Work

This work, like many cutting edge engineering projects, has been a joint effort between generations of students and fundamentally relies on collaboration and teamwork. My contributions are based on high-energy amplification in fibers, from a single fiber channel to the four-channel CBC system, which I built from the ground-up, and integrated with the temporal combining experiments led by Hanzhang Pei and Mathew Whittlesey. I took over laser modeling, burst design and stretcher/compressor duties from Siyun Chen, including designing and optimizing the new compressor and modifying her Offner stretcher design. For a complex experimental system the upkeep and maintenance is not trivial; for the past three years these duties have been shared by Mathew Whittlesey and me and includes everything from oscillator adjustments to RF electronics troubleshooting. The controls system was designed by Qiang Du at LBNL, who provided hardware, hardware level code and support. Specific control code and implementation for the CBC system was designed, written and tested by me. In addition, I have participated in training the next generation of students, specifically Christopher Pasquale and Yanwen Jing, who are now both equal contributors to our work.

The neutron generation experiment is led by Nicholas Peskosky. I, with help from Christoper Pasquale, handle the laser front end, CBC system and compressor and assist with any beam delivery into the chamber, while Yanwen Jing runs temporal combining. The fiber backlight was conceived and designed by me and Nicholas Peskosky; experimental work has been led by Christoper

Pasquale with assistance from me and Nicholas.

CHAPTER 2

Temporal Combining in a Highly Saturated Amplifier

2.1 Introduction

As a technique for maximizing fiber energy and minimizing CBC array sizes CPSA first requires validation using a single amplifier to elucidate the effects of high saturation on temporal combining and pulse compression. This requires an understanding of the limits of energy storage and extraction in a fiber amplifier, along with the effects of nonlinear phase and spectral reshaping on a burst of chirped pulses. This chapter contains analysis of energy extraction from a 85 μm-core chirally-coupled-core (CCC) fiber, showing energy storage above 10 mJ, and subsequently uses this fiber at varying levels of extraction to study the effects and limits of saturation on temporal combining and compression. Ultimately the experiments show 10 mJ extracted from the final amplifier with 58% temporal combining efficiency and compression to 340 fs, limited by spectral reshaping induced nonlinear-phase accrual. While this result is done at extracted energies 3x higher than any other previous work, the goal is to improve temporal combining efficiency to 80-90% at these energy levels by adding active control of the pulse spectrum and compensation of residual nonlinear phase accrual.

The work in this chapter not only represents a significant step in increasing fiber energy and thus decreasing future array sizes but also provides a experimental and theoretical road map for future work on higher-storage fiber.

2.2 Key Ytterbium Doped Fiber Technology

2.2.1 Single Mode Large Core Fiber

The most simple design fiber design is a cylindrically-symmetric waveguide consisting of a core of radius a surrounded by a cladding of lower refractive index. Light is guided through total internal reflection (TIR) with an acceptance numerical aperture (NA) into the core determined by the index contrast $NA = \sqrt{n_{\text{core}}^2 - n_{\text{clad}}^2}$. A normalized parameter $V = k_o a(NA)$ combines radius and NA with the angular wavenumber k_o to express modal content; for $V < 2.405$ the fiber only guides the fundamental mode, which to a high approximation resembles a Gaussian [59], and for high V the mode number scales as $N = \left(\frac{2}{\pi}V\right)^2$ [60]. Standard single-mode fiber (SMF) uses a core diameter $2a = 6$μm and an $NA = 0.12$ to keep $V < 2.405$ for wavelengths above 940 nm. For amplification the core can be doped with rare-earth atoms [61] and the coupled pump is also guided, giving large absorption and efficient energy transfer to the laser signal. These fibers enable telecommunications, precise frequency combs, and low-energy laser systems. However, for generating high power beams these fibers are not sufficient for several reasons: (1) the small core size requirement for single-mode guidance limits available energy and enhances nonlinear effects, and (2) pump beams from diode lasers matching the single mode core profile are limited to about 1 W.

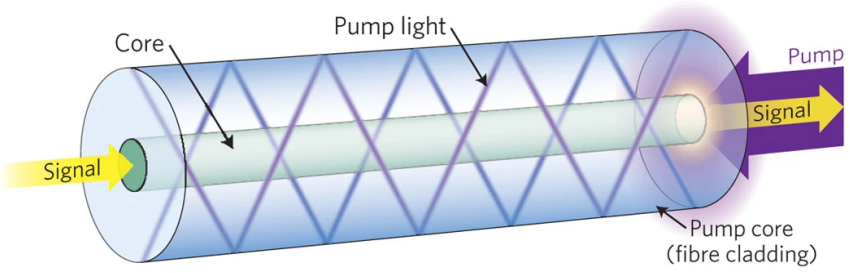

Figure 2.1 : Signal amplification in a double-clad fiber in counter-pumped configuration. The core (green) guides the signal and the cladding guides the pump. Reprinted from [62]

The pumping problem is readily solved by using the cladding as a second, large core for the pump with the final cladding formed by a low-index acrylate coating that doubles as the fiber

jacket, as shown in Fig. 2.1. This creates a double-clad fiber (DCF) where the pump core supports hundreds of modes, relaxing coupling requirements to simple etendue matching to the area and acceptance solid angle, allowing for use of lower brightness, higher power pumps in a configuration known as "cladding pumping" [63]. Pump absorption results from the overlap of the cladding modes with the core doped area and, despite the relatively small area ratio, can be very high in only several meters of fiber.

Solutions to scaling the core diameter while maintaining single mode guidance are far more complicated; the most common techniques use nominally multi-mode cores that either strip higher-order modes (HOMs) through coiling [64], through some fiber-integrated structure [65, 66], or through resonant coupling structures [67, 68] . Coiling is usually done in large mode area (LMA) fibers which a core and cladding strongly resembling SMF but with a $V > 2.405$ leading to guidance of a few HOMs. The confinement of the HOMs to the core is smaller than the fundamental, and with the linear index perturbation introduced by coiling they can be forced to radiate through frustrated-TIR with, at the proper bend radius, losses orders of magnitude above the fundamental loss. However, as the core scales above 30 µm diameter, the bend radius range required to make HOMs lossy while maintaining high fundamental transmission becomes impractically small. For this reason coiling for single-mode guidance is practically limited to $\leq$30 µm core diameters.

For core sizes above this region most approaches rely on effective-single mode operation whereby some structure of the fiber inhibits or suppresses HOMs. This broad category includes many different fibers but only two types are commercially available: (1) polygonal CCC that relies on an index-guiding core with a helical perturbation that couples HOMs to the cladding, and (2) photonic-crystal fiber (PCF) rods that rely on a band-gap structure to limit core guidance to a single mode. An important consequence of PCF structures is that the band-gap guided core modes can overlap with the index-guided cladding modes; in cladding-pumped DCFs this means significant gain can be seen by cladding modes, requiring modifying the cladding inclusions to de-localize the overlapping modes and strongly confine the fundamental to the doped core [69]. This has the effect of creating strong gain-differentiation and "gain-guiding" the fundamental which can break down

at very high gains, limiting the stored energy of these fibers. These complex cladding inclusions and delicate gain equilibrium also mean that the fiber cannot be fusion spliced or tapered and generally must be held straight to avoid perturbations, removing the packaging advantages inherent to index-guiding silica fibers.

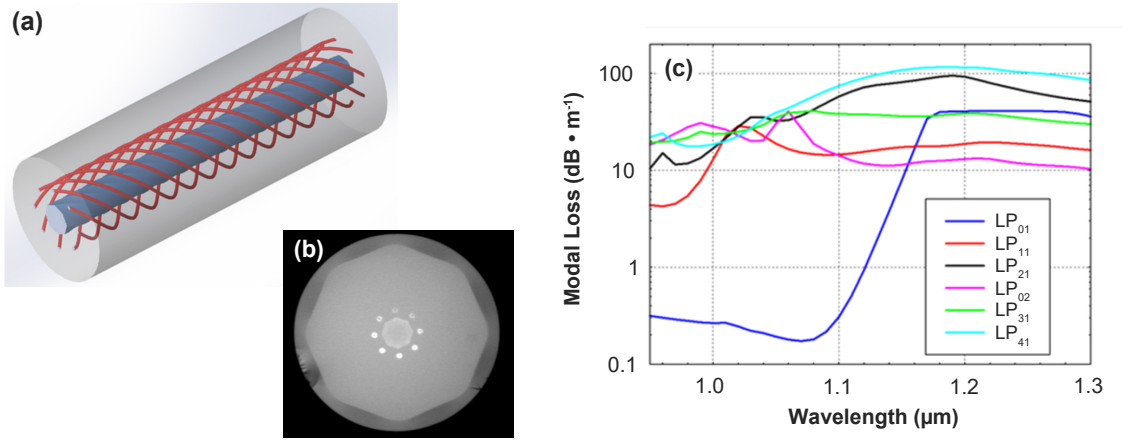

Figure 2.2 : CCC Fiber: (a) Isometric view showing spun side cores around central core, (b) microscope end-face view showing octagonal central core and cladding, and (c) numerically calculated loss spectrum for the lowest order modes. Effective single mode guidance is preserved between 1020 nm and 1120 nm where the fundamental mode has loss of about 0.2 dB · m^{-1}. Reprinted from [67].

In contrast, CCC fibers, shown in Fig. 2.2, use a normal index-guiding structure with a helical perturbation that makes it lossy to HOMs and, like any index-guiding DCF, does not see coupling between core and cladding modes [67]. This means standard cladding-pumping can be used, the fiber can be coiled, tapered or spliced, and the gain and as such stored energy can be very high. For all of these reasons CCC fibers are suitable for packaging into pump-combiners, a fiber device that monolithically integrates a passive signal fiber with active fiber and pump delivery fibers, allowing for high-power pumps to be coupled to active fiber with no alignment [70]. This also means core-size and thus stored energy scaling is not limited, and there is potential for fibers that store 20-50 mJ in the future [71]. For all these reasons CCC is strongly preferred over other fiber for the basis for high-energy CBC arrays and thus they are used in this work.

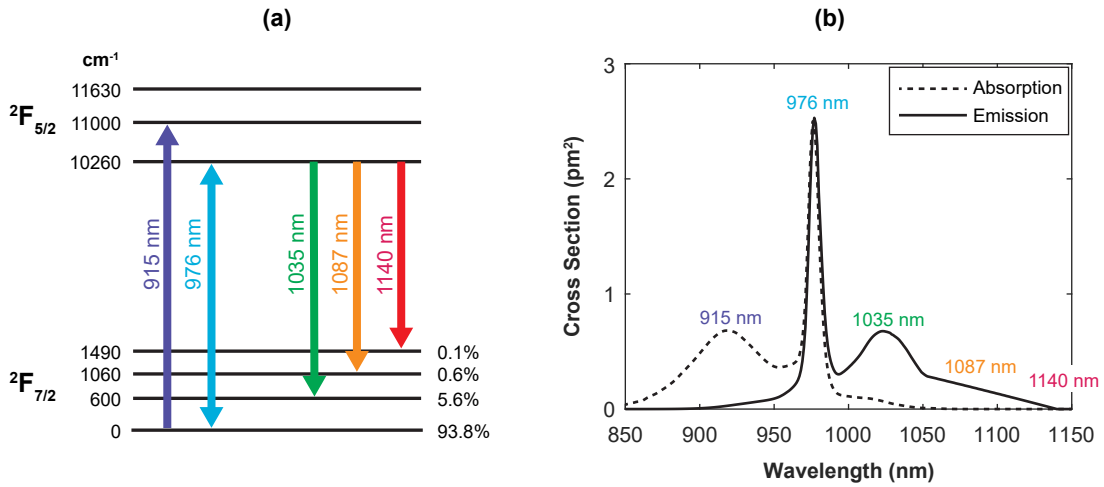

Figure 2.3 : Diagram showing (a) the Yb:Glass level structure along with the thermal occupancy of the lower levels at 300 K and (b) the resulting absorption and emission spectra (data provided by nLight, Inc.).

2.2.2 Yb:Glass Level Structure

Laser action in Yb^{3+} embedded in glass comes from the stark-split $^2F_{7/2}$ and $^2F_{5/2}$ levels as shown in Fig. 2.3a [72]. The specific laser action is dependent on the pump and emission wavelength; for 915 nm pump and 1087 nm or 1140 nm emission the system is four-level; for the common 976 nm pump and 1035 nm emission the system is known as "quasi three-level". In this configuration pumping is done directly to the upper laser level, meaning that no more that 50% overall inversion can be achieved, and the lower laser level maintains some thermal occupation, meaning that a certain inversion must be achieved before the system will provide gain. In this work, wavelength-stabilized 976 nm pump diodes are used for the lower quantum defect and high absorption; this means the laser action is quasi three-level.

2.2.3 Effective Mode Area and Nonlinear Interactions

When deriving the nonlinear Schrodinger equation for pulse propagation in a fiber the term governing the strength of the nonlinear interaction γ is inversely proportional to an integral that has units of area. This is termed the "effective area" $A_{\text{eff.}}$ with general form shown in Eqn. 2.1 where

$E(x, y)$ is the field profile in the fiber [44].

$$A_{\text{eff.}} = \frac{\left(\int\int_{-\infty}^{\infty} |E(x,y)|^2 dxdy\right)^2}{\int\int_{-\infty}^{\infty} |E(x,y)|^4 dxdy} \tag{2.1}$$

For a Gaussian with mode-field diameter (MFD) defined at the e^{-2} point this reduces to $A_{\text{eff.}} = \frac{\pi}{4}(\text{MFD})^2$, notably 2x larger than the area of a Gaussian $\frac{\pi}{8}(\text{MFD})^2$. This leads to some confusion in the literature when calculating the nonlinear phase. Another important distinction is that the waveguiding means temporal phase applies to the whole mode, eliminating spatio-spectral coupling that may be seen in free-space.

The peak nonlinear phase is typically calculated by the B-integral [73], which tracks the maximum on-axis phase shift based on peak, on-axis intensity $I(z)$. This can be extended to a time-varying B-integral using $I(z, t)$ which, for a Gaussian mode in fiber, can be related to peak power $P(z, t)$ using the effective area $P(z, t) = I(z, t) \times A_{\text{eff.}}$.

$$B = \frac{2\pi}{\lambda_0} n_{2\text{I}} \int_0^L I(z)dz = \frac{2\pi}{\lambda_0} \frac{n_{2\text{I}}}{A_{\text{eff.}}} \int_0^L P(z,t)dz \tag{2.2}$$

A common technique for solving this integral in fiber optics is to assume exponential gain or loss in the form $P_{\text{out}}(t) = P_{\text{in}}(t) \exp(g_0 z)$ where g_0 is the gain in m^{-1}; evaluation then leads to a term dependent on L and g_0 known as the *effective* length $L_{\text{eff.}}$. As discussed in Sec. 1.6 this approximation can be referenced to the either the input or output power and allows for a simple expression for the nonlinear phase $\phi_{\text{NL}}(t)$ along the fiber, as given in Eqn. 1.3. For any situation where the gain cannot be expressed analytically a numerical model will be needed to first solve the $P(z)$ evolution and thus calculate the B-integral.

Counter-intuitively fibers exhibit self-focusing at around 4-5 MW (for linear polarization) [74], similar to free space, with some variation as the value of $n_{2\text{I}}$ can include large contributions from electrostriction for pulses above 1 ns duration [75].

Limits on B-integral of <2-5 rad are often given for solid-state lasers [10, 73] to define regions of "safe" operating without beam breakup or self-focusing, but should be avoided when dealing

with optical fibers. The long interaction length and small area means peak powers can remain far below self-focusing threshold while the pulse can also accrue B $\gg 5$. In general, for fiber CPA B-integral will always limit pulse compression before any spatial effects occur.

2.2.4 Gain Recovery Time in Highly-Pumped Fiber

Pulse amplification and energy extraction at high repetition-rates is determined by how fast the inversion, and thus the gain, recovers between pulses. For pulsed amplifiers where the pulse period is lower than the gain recovery time the gain reaches the maximum, unsaturated value between pulses; when pulse period is larger than than the gain recovery time the peak gain is saturated to a lower value. Thus the full stored energy of the amplifier is available only if the gain can fully recover between pulses—achievement of this is critical for high rep-rate, high energy amplification.

Mathematically the gain recovery time T_1 can be defined as the time it takes for the gain to reach $1 - e^{-1} \approx 63\%$ of its maximum value after a step-response pump pulse is applied. Intuitively gain recovery should be dependent on pumping intensity; however, in most solid state gain media the pump intensity is not high enough for gain recovery to deviate from the asymptotic value of the upperstate lifetime τ_u [10]. In optical fibers guiding of pump can lead to large lengths of very high intensity that require the full expression for the gain recovery time T_1. The derivation is easily done using rate equations for a pump transition center frequency ω_p and in addition to τ_{u} it is dependent on the pump intensity I_p, and the emission and absorption cross sections at the pump frequency σ_e^p and σ_a^p, respectively.

$$\frac{1}{T_1} = \frac{I_p}{\hbar\omega_p}\left(\sigma_e^p + \sigma_a^p\right) + \frac{1}{\tau_{\mathrm{u}}} \tag{2.3}$$

The pump intensity needed to reduce T_1 by 50% can be solved for in a transition where $\sigma_p^a = \sigma_p^e$; unsurprisingly this is in the same form as the saturation intensity for CW amplification given in [10]. For Yb:Glass pumped at 976 nm where σ_a^p =2.3 pm^2 and $\tau_{\mathrm{eff.}}$ = 770 µs [72] this yields a value of about 5.6 kW $\cdot$ cm^{-2} corresponding to about 1.9 mW of pump in a SMF and about 7 W of pump

in a 400 µm cladding pumped fiber laser.

$$I_p = \frac{\hbar\omega_p}{2\sigma_a^p \tau} \tag{2.4}$$

Fig. 2.4 shows the dependence of T_1 on pump power for several different types of fiber pumping

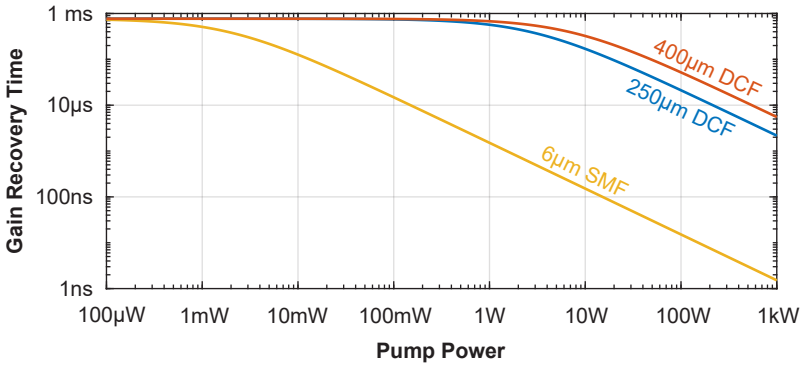

Figure 2.4 : Calculated Yb fiber gain recovery time vs. pump power for 6 µm SMF core pumped fiber, 250 µm and 400 µm cladding-pumped fiber.

geometries. As a rule of thumb for a pulse period 2-3x smaller than the gain recovery time no reduction in pulse energy will be seen; for CCC fiber with 400 µm cladding 10 kHz operation will require 30-50 µs recovery time or pumping in the region of 100-160 W. Of course, the pump intensity decreases along the fiber length so this is likely a slight underestimate.

2.3 Energy Extraction From Optical Amplifiers

Minimizing CBC array sizes requires maximizing fiber stored energy and the fraction extracted; efficient temporal combining requires understanding any effects that occur when the amplifier is heavily saturated. This section reviews the theory of energy storage in amplifiers and then connects to measurement of 1.8 m of 85 µm-core CCC fiber, showing in excess of 10 mJ stored and that, with the appropriate seed level, greater than 90% can be extracted. Two methods of calculating stored energy are discussed along with sources of potential errors in both.

2.3.1 Frantz-Nodvik Model of Amplifiers

The classic model for a saturated amplifier is derived from two coupled differential equations describing the temporal and spatial change of the pulse intensity $I(t, z)$ and the inversion $\Delta N(z, t)$. Two simplifying assumptions are made: (1) the pumping does not change the inversion along the pulse, a good assumption for pulse duration less than the gain recovery time $\tau_p \ll T_1$, and (2) spontaneous emission effects are negligible, again a good assumption for pulse duration much less than the upperstate lifetime $\tau_p \ll \tau_u$. The following analysis is written for a single value of the emission cross section σ_e but is fully valid still in situations where the cross section varies across the bandwidth, for example in a heavily chirped pulse it can be written as $\sigma_e(t)$. This model is known as the Frantz-Nodvik amplifier analysis after the authors who first derived it [76].

Spatial integration of the z coordinate removes the longitudinal dependence, effectively lumping the inversion into a single, time varying slice described by the total inversion $N_{\text{tot.}}(t)$, with initial value $N_{\text{tot.}}(t = 0) = N_0$. The gain then is written $G(t) = \exp\left(\sigma_e N_{\text{tot.}}(t)\right)$, with initial value $G(t = 0) = G_0$, final value after the pulse $G(t = \tau_p) = G_f$, and the accumulated energies in the input and output signal are written $E_{\text{in, out}}(t) = A_{\text{eff.}} \int_0^t I_{\text{in, out}}(t)dt$. After lumping constants together into a term know as the saturation energy $E_{\text{sat.}} \equiv \left(\frac{\hbar\omega}{\sigma_e+\sigma_a}\right) \times A_{\text{eff.}}$, the time varying gain can be written in a concise manner.

$$G(t) = e^{\sigma N_{\text{tot}}(t)} = 1 + (G_0 - 1)\exp\left(\frac{-E_{\text{out}}(t)}{E_{\text{sat}}}\right) = \frac{G_0}{G_0 - (G_0 - 1)\exp\left(\frac{-E_{\text{in}}(t)}{E_{\text{sat}}}\right)} \tag{2.5}$$

This time varying gain governs pulse reshaping through $I_{\text{out}} = G(t)I_{\text{in}}$ and gives insight into how the amplifier upper-state empties during amplification, as shown in Fig. 2.5. In general, higher saturation leads more emptying of the inversion and thus a strongly-varying gain across the pulse, which leads to pulse reshaping, an inevitable consequence of saturated amplification. This equation can be used to design input or output burst shapes if desired.

The pulse energy gain in the amplifier is dependent only on the difference between the initial

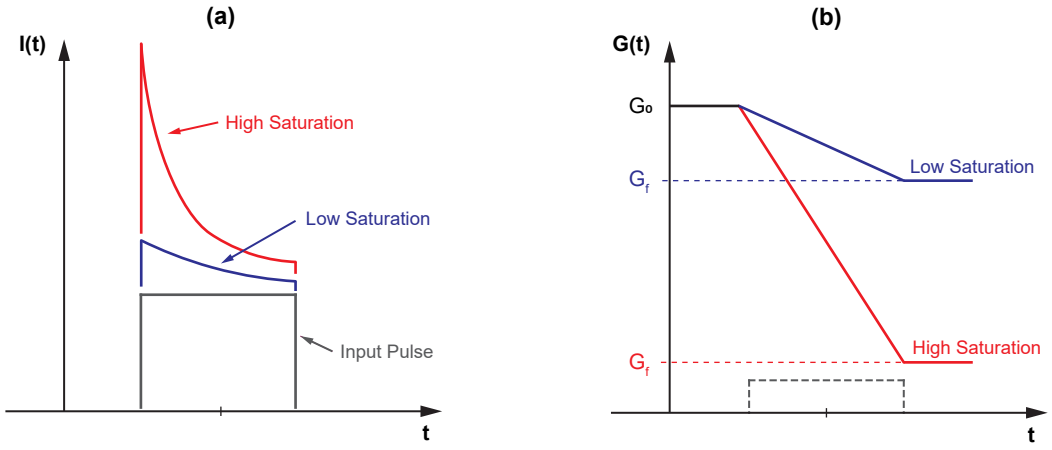

Figure 2.5 : Amplifier saturation effects: (a) reshaping of a initially flat input pulse and (b) corresponding time-varying gain across the pulse.

and final gain, as can be seen in Eqn. 2.6.

$$G_{\text{pe}} = \frac{E_{\text{out}}}{E_{\text{in}}} = \frac{\log\left(\frac{G_0-1}{G_f-1}\right)}{\log\left(\frac{G_0-1}{G_f-1}\right) - \log\left(\frac{G_0}{G_f}\right)} \tag{2.6}$$

Unsurprisingly then the energy stored in the amplifier is simply related to the initial gain before the pulse. Thus for a given gain medium with fixed cross sections measuring G_0 is a direct measurement of the stored energy and maximizing G_0 maximizes stored energy.

$$E_{\text{stor.}} = E_{\text{sat}} \times \ln(G_0) \approx 0.23 \times E_{\text{sat.}} \times G_0^{\text{dB}} \tag{2.7}$$

The final important parameter is the fraction of the stored energy that the amplified pulse extracts, denoted as η_e, which is calculated from the difference of the output and input energy divided by the stored energy and is only dependent on the overall change in the inversion along the pulse.

$$\eta_e = \frac{E_{\text{out}} - E_{\text{in}}}{E_{\text{stor.}}} = 1 - \frac{\ln(G_f)}{\ln(G_0)} = 1 + \frac{\ln\left(1 - \frac{G_0-1}{G_0 \exp(E_{\text{in}}/E_{\text{sat.}})}\right)}{\ln(G_0)} \tag{2.8}$$

The direct interplay of G_0, input energy, pulse gain G_{pe} and extraction efficiency η_e is shown in

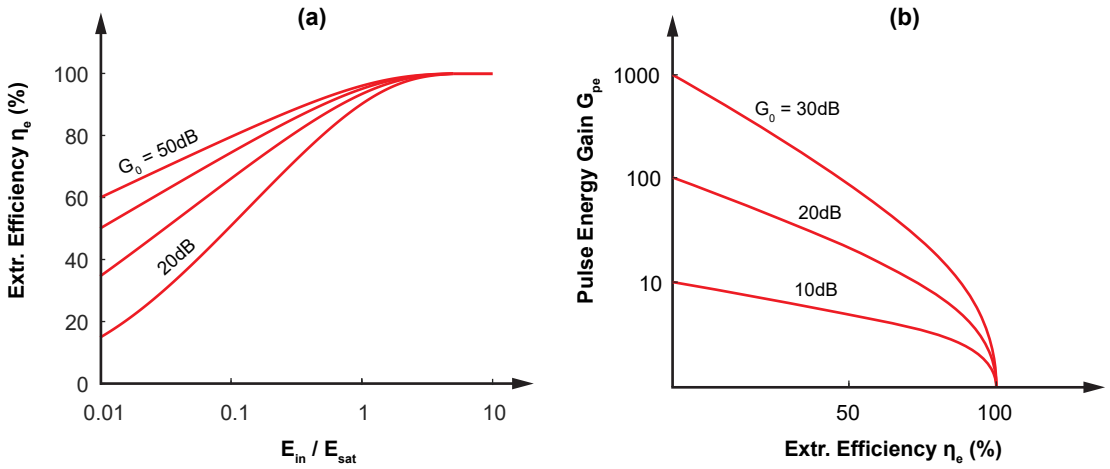

Figure 2.6 : Amplifier efficiency and pulse gain plots. (a) Extraction efficiency for the input energy as a fraction of the saturation energy and (b) pulse energy gain vs extraction efficiency, both for varying levels of initial gain G_0.

Fig. 2.6; there are three important consequences: (1) for high energy extraction an input energy comparable to the saturation energy must be used, (2) the real pulsed gain appears lower at higher saturation, and (3) measuring pulsed gain at low extraction/small input signal gives a good estimate of G_0. This final point leads to G_0 being called the small-signal gain (SSG) and gives a practical approach to measuring this critical amplifier parameter.

In this model of amplifier for a given material and transition wavelength there are only two free parameters: (1) the total inversion before the pulse as measured by G_0, (2) the pulse input *or* output intensity $I_{\text{in,out}}(t)$. The second parameter can be written in terms of input or output energy and input or output shape; either way, trying to control more than these parameters for a given amplifier is not possible.

2.3.2 High Energy Amplifier Characterization

The theory of the previous section proves very useful for connecting to real amplifiers because it contains parameters dependent only on input and output signals, which can easily be measured. Stored energy and extraction efficiency can be calculated just knowing the SSG G_0, the cross sections and the pulsed gain G_{pe}. Cross sections are generally available from the optical fiber

manufacturer; however, measurement uncertainty is usually large.

Measurement of G_{pe} at low extraction ($\eta_e \ll 1$) approximates G_0. The energy level of the seed for this measurement can be calculated from the theory but can also be experimentally validated by using the ASE from the amplifier as a proxy for saturation. In the low extraction limit the pulse will not change the amplifier gain at all, meaning parasitic amplification of the spontaneously emitted photons will remain constant. If the pulse begins to extract energy it will reduce the gain in the amplifier and thus lower the ASE. In fact, because the signal in this measurement does not change the inversion at all it can be measured by calculating the gain of either a CW or pulsed seed. For our amplifiers (1.8 m of 85 µm core CCC fiber) this means seeding with <5µW at 1MHz (5pJ) and measuring output signal powers of about 200mW (200nJ) with $G_0 \approx 45$dB. Fig. 2.7 shows

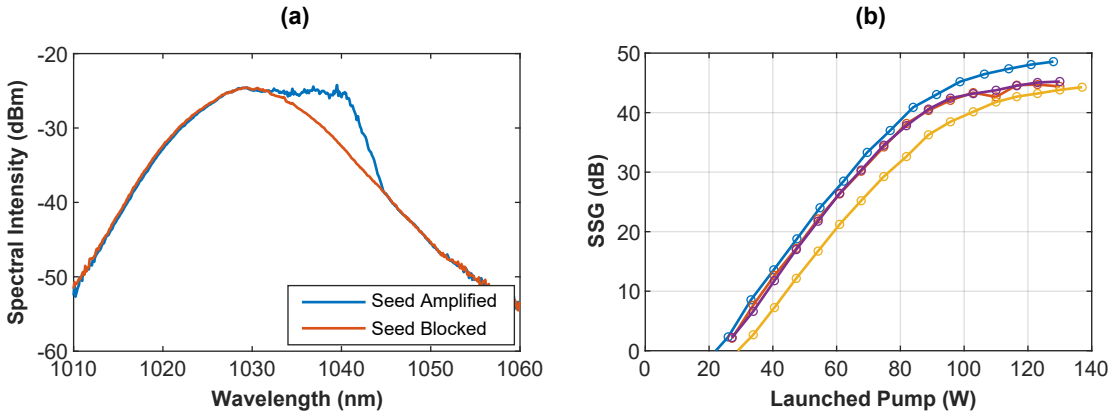

Figure 2.7 : Small signal gain measurements of CCC amplifiers: (a) Output spectrum with small (5 µW) seed blocked and unblocked, showing the seed does not deplete the inversion and (b) 4 measurements of SSG for 1.8 m of fiber selected from different sections along the 80 m draw length.

experimental results of this measurement, with the unchanging ASE spectrum indicating that the amplifier is not saturated. Fig. 2.7b shows several different curves measured on different fibers along the 80 m draw length; some variations in drawing condition when fabricating the fiber lead to slightly different MFD and helical pitches, changing the fiber waveguiding and small signal gain slightly.

Only knowledge of the transition cross sections are needed to use Eqn. 2.7 to calculate the stored energy. While the cross sections are easily available in practicality the McCumber relations

that are used to calculate the emission cross section have limited validity in amorphous glass hosts such as Er^{3+}:Glass or Yb^{3+}:Glass [77] and often overestimate the true value; this will then underestimate the saturation energy. Additionally the measured cross sections reported in the literature vary, likely due to differences induced by secondary dopants in the fibers as well as measurement uncertainty. This uncertainty means that the actual value of $E_{\text{sat.}}$ likely needs to be tweaked by comparing experiment to model, adding yet another free parameter. This comparison, done by matching burst shapes from theory and measurement and shown in Fig. 2.8, results in a value of $\sim$1mJ that fits the data fairly well, predicting an emission cross section $\sim 70\%$ of the measured value. This then allows for a direct estimation of the stored energy using Eq. 2.7; for 45 dB SSG the stored energy is $0.23 \times 1\,\text{mJ} \times 45 \approx 10.4\,\text{mJ}$.

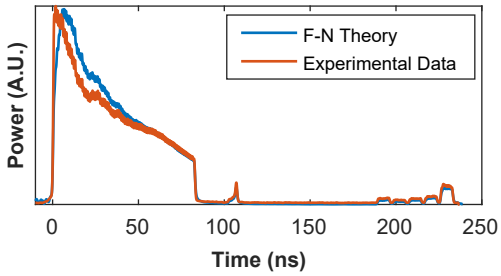

Figure 2.8 : Matching of Frantz-Nodvik model to real data for G_0 = 32dB and E_{out} = 5 mJ, showing that a value of $E_{\text{sat.}}$ = 1 mJ is needed to properly match the data.

Measurement of amplified energy at different seed levels is used to calculate extracted energy and extraction efficiency. The results of amplification measurements are shown in Fig. 2.9, where amplified energies approach the 10.4 mJ storage limit and the amplified energy is maximized for seed levels above 230 µJ. At the maximum pump level of 105 W, corresponding to 45 dB SSG, the extracted energy is 9.2 mJ for a 250 µJ seed, giving an extraction efficiency of 88%, showing good agreement with the theoretical predication of 85%.

A separate method for measuring stored energy without reliance on crosssections σ_e and σ_a

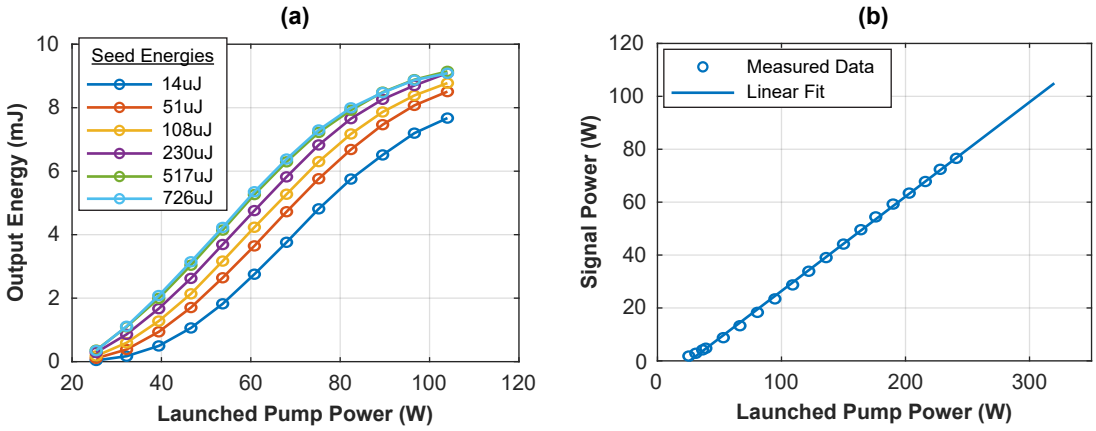

Figure 2.9 : Energy and average power measurements from a 1.8 m CCC fiber amplifier: (a) energy vs. pump for many seed levels, showing 230 µJ is sufficient for full energy extraction and (b) amplified power vs. pump power at 10 kHz showing 35% slope efficiency with respect to launched power. About 300 W of pump will be needed for 100 W operation.

uses Eqns. 2.8 and 2.6 re-written in terms of G_{pe}, G_0 and η_e only.

$$G_{\text{pe}} = \frac{\log\left(\frac{G_0-1}{G_0^{1-\eta_e}-1}\right)}{\log\left(\frac{G_0-1}{G_0^{1-\eta_e}-1}\right) - \log(G_0^{\eta_e})} \tag{2.9}$$

This requires use of a numerical solver such as fzero in MATLAB to calculate the extraction efficiency η_e for given G_{pe} and G_0, after which Eqn. 2.8 can then again be used to relate the stored energy to the extracted energy and extraction efficiency $E_{\text{stor.}} = (E_{\text{out}} - E_{\text{in}}) \times \eta_e^{-1}$. The results of this calculation are given in Fig. 2.10. The large variance in the plot suggests that this measurement is highly susceptible to measurement errors in SSG and G_{pe}.

Systematic error in these measurements comes from the seed coupling efficiency η_c that can vary from 25% to 90% and will effect the measurements of G_0, G_{pe} and $E_{\text{extr.}}$—by applying one final condition this parameter can be determined. The extracted energy $E_{\text{extr.}} = E_{\text{stor.}} \times \eta_e$ is linearly dependent on the extraction efficiency and has a y-intercept of zero. Generating a plot using the numerically solved η_e for different stored energies (lower pumping levels) and applying a linear fit will generate a y-intercept that can be forced to zero by varying η_c, thus backing out the coupling efficiency. This technique has been used successfully in the past for other fiber but requires data

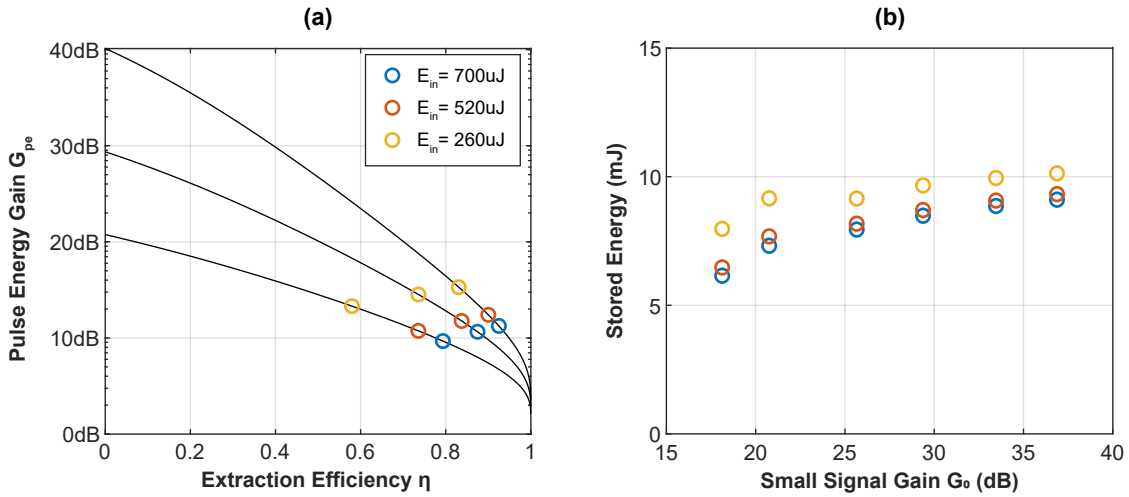

Figure 2.10 : Results of stored energy calculation showing: (a) numerical fit of extraction efficiency η_e for a given small signal gain and pulse gain, and (b) the corresponding stored energy calculated from the values of η_e and the extracted energy $E_{\text{extr.}}$. The legend in (a) applies to both figures.

free of random errors and as such is omitted here for the data presented above.

The analysis of Sec. 2.5.1 indicates 100-150 W of pump is required to reduce gain recovery sufficiently for 10 kHz operation with full stored energy. Measurement of the same 1.8 m section of fiber from above at 10 kHz rep-rate yields 8 mJ / 80 W of output at 250 W of pump, with a slope efficiency of 40%, shown in Fig. 2.9. This predicts that 300 W of pump will be needed to extract 10 mJ at 10 kHz, larger than the theoretical value—this is expected as the theory gives a rough estimate without considering pump absorption along the fiber. The current measurement is limited to 250 W of pump by heat extraction from the fiber, a technical problem that will be solved by epoxying the fiber to the groove it currently lies in, increasing contact to the water-cooled aluminum base. The slope efficiency of 40% represents a larger, not fully understood trend in large-core fiber design: even for the same fiber preform with same doping concentration and refractive index, fiber drawn to a larger core will have lower slope efficiency. Current LMA fibers can reach 80% slope efficiency and ongoing work aims to bring large-core fiber to this standard.

2.4 Design of Equal-Nonlinearity Bursts in the Monochromatic Limit

In the heavily saturated regime required for full energy extraction the amplifier induces large temporal pulse reshaping. Controlling the input burst shape provides control of amplified burst shape, at the cost of inducing a large, temporally-varying B-integral along the burst. However, controlling the input burst shape can both equalize and minimize the B-integral, at the cost of a large variation in output amplitude. The first pulse sees the smallest B-integral and by equalizing all the following pulses to this value the nonlinear phase is minimized.

This section explains the process of designing equal-nonlinearity burst shapes under the narrow bandwidth approximation by first showing an analytical derivation and then a numerical calculation. Stacking simulations are then shown for the designed equal-nonlinearity burst shapes confirming high temporal efficiency; some additional methods for increasing pre-pulse contrast of the stacked burst are described along with simulations.

2.4.1 Validity of Simplifying Assumptions

Initial analysis can be done using the Frantz-Nodvik theory of the preceding section while additionally assuming that the pulses are monochromatic, allowing for use of constant values of σ_e and σ_a. This is not fully valid for ultrashort CPA in Yb:glass as the cross sections change over the bandwidth. However, in the absence of pulse *spectral* reshaping, matching the peak nonlinear phase of each pulse in the burst will also match the spectral phase of each pulse. This assumption breaks down for high gain and high bandwidth, as will be discussed later; however, this initial analysis will again show that solutions are possible and valid in the monochromatic limit.

The second assumption used here is that the burst of 81 1 ns pulses in CPSA can be approximated as a single smooth burst of 81 ns in length. For pulses that are spectrally flat and nearly stretched into each other this assumption is valid; a numerical model for propagating each chirped pulse in the burst will be needed to cover more complicated situations.

2.4.2 Analytical Approximate Solution

Use of the nonlinear effective length concept from Eqn. 1.5, combined with the Frantz-Nodvik gain equations, gives an equation for the output power of the amplifier of SSG G_0 given a desired ϕ_{NL}, fiber length L, and nonlinear coefficient $n_{2\text{I}}$ [78].

$$P_{\text{out}}(t) = \frac{\beta \times \ln(G_0) \times \exp\left(\frac{-\beta t}{E_{\text{sat.}}}\right) \times G_0^{\exp\left(\frac{-\beta t}{E_{\text{sat}}}\right)}}{G_0^{\exp\left(\frac{-\beta t}{E_{\text{sat.}}}\right)} - 1} \qquad (2.10)$$
$$\beta = \frac{A_{\text{eff.}}}{k_o n_{2\text{I}} L} \phi_{\text{NL}}$$

This is connected to the input pulse shape by $P_{\text{in}}(t) = [G(t)]^{-1} P_{\text{out}}(t)$. This equation contains G_0 and E_{sat} and prescribes $P_{\text{out}}(t) \propto I_{\text{out}}(t)$ for a given ϕ_{NL}, thus fixing all the free parameters of the system for a given nonlinear phase value. While the use of $G(t)$ from the Frantz-Nodvik theory accurately accounts for burst reshaping and connects directly to amplifier parameters, the effective length assumes exponential longitudinal gain, a regime that is only valid in for low saturation amplifiers. Nonetheless this result shows that varying the output burst shape can control pulse nonlinearity accrual.

2.4.3 Numerically Calculated Solutions

Limitations of the effective length concept require a numerical model for calculating nonlinear phase under saturated amplification. For pulse propagation the same assumptions of the Frantz-Nodvik model, that pumping and spontaneous emission effects are neglected, are still valid and simplify the analysis into a two-step process: (1) solve the amplifier inversion $\Delta N(z)$ for a given pump under no-seed steady-state conditions, then (2) propagate the pulse $P(t)$ through this inversion, neglecting any pump or spontaneous emission.

The amplifier inversion is calculated using a standard technique for modeling rare-earth doped fiber lasers where rate equations for the upper and lower manifold are used and the sub-levels are

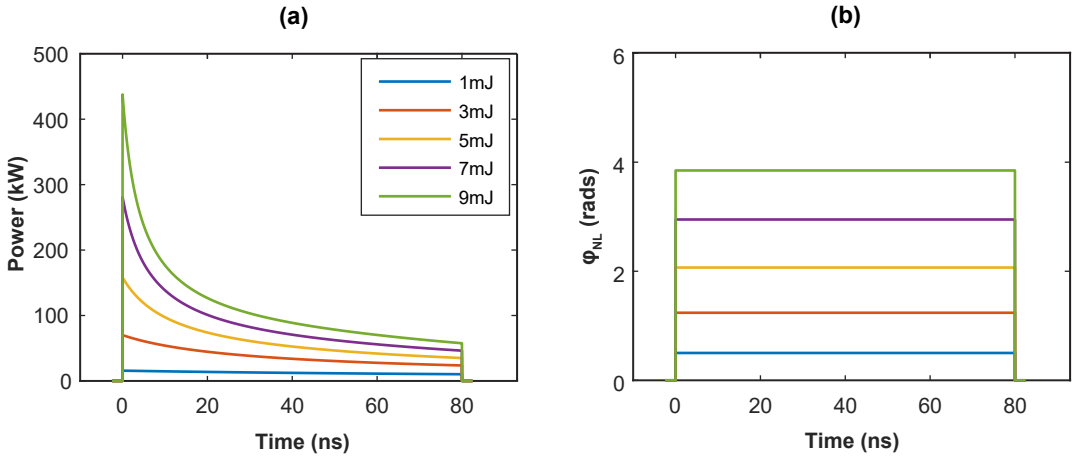

Figure 2.11 : Numerically calculated equal nonlinearity bursts: (a) burst shapes out of the amplifier, and (b) the corresponding optimized phase profiles.

encoded using the effective cross sections [79]. An iterative method is required to solve for the ASE in the forward (co-propagating with respect to pump) and backward (counter-propagating w.r.t. pump) directions and is done using the boundary conditions that the backwards propagating ASE is zero at the end of the fiber $P^{-}_{\text{ASE}}(z = L) = 0$ and the forward propagating ASE is zero at the pump end of the fiber $P^{+}_{\text{ASE}}(z = 0) = 0$ [80], where the pump enters at $z = 0$ point of the fiber of length L. This generates a steady-state discretized inversion $\Delta N(z_i)$, $1 < i < N$ that can then be used to calculate pulse gain.

Pulse propagation is done using rate equations describing the power added to the signal $P(t_j)$, $1 < j < M$ at each amplifier step z_i due to the power $P(z_i, t_j)$ inducing stimulated emission and reducing the inversion $\Delta N(z_i, t_j)$. Tracking the power of the signal at each longitudinal point z_i allows for numerical calculation of the B-integral. For equalization of B-integral along the burst the derivative $\frac{d\phi_{\text{NL}}(t_j)}{dP_{\text{in}}}$ is numerically approximated and then used to optimize the phase to the target value. To match the experimental data the model used in this section matches the input and output energies for a given G_0 to experimental values while varying the *shape* of the burst to equalize phase accrual. As a note, the pulse propagation of M time steps and N spatial steps will have $M \times N$ time complexity requiring propagation code to be properly written in a fast, compiled language such as C++ for all but the simplest cases. Figure 2.11 shows the result of this

optimization for several different output energy levels matched to levels used in experiment. The analysis is done using the same monochromatic assumption of the analytical theory but the model is fully valid for extension to separated chirped pulses and can calculate individual pulse reshaping and nonlinear phase accrual, at the cost of longer simulation time.

2.4.4 Stacking of Shaped Bursts

Effects on pulse stacking of the equal-nonlinearity bursts can be calculated using stacking simulation code [78, 81]. The effects of truncated stacking as well as pre-burst optimized stacking are shown in Fig. 2.12 for the 3 mJ burst shape; the scaling trends are shown in Fig. 2.13. Stacking can maintain 90% efficiency even at the 9 mJ burst shape, however pre-pulse contrast suffers and does not benefit nearly as much from pre-burst optimization as the equal-amplitude burst.

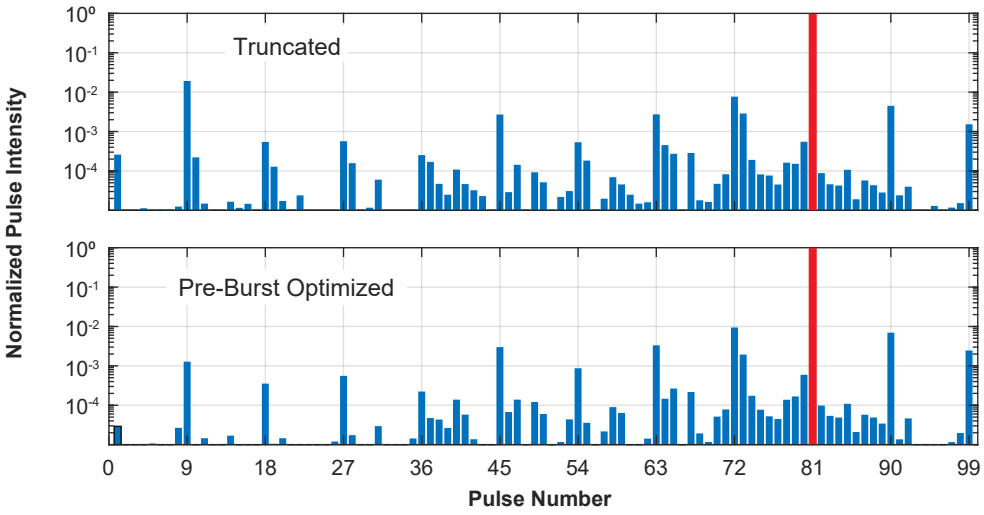

Figure 2.12 : Theoretical stacking traces in logarithmic scale for the 3mJ burst shape shown in Figure 2.11 with and without a pre-burst added. The main pulse is shown in red and for the pre-burst case the pulses before the 1st are omitted for clarity; they are all more than 60 dB back behind the main pulse.

For a stacking approach to increasing pre-pulse contrast (as opposed to external pulse cleaning) the large parameter space of cavities phases, pulse phases and beamsplitter reflectivities can be leveraged. By allowing all parameters to vary pre-pulse contrast can be optimized while sacrificing some stacking efficiency; this has the effect of trading pre-pulse and stacked pulse power into the

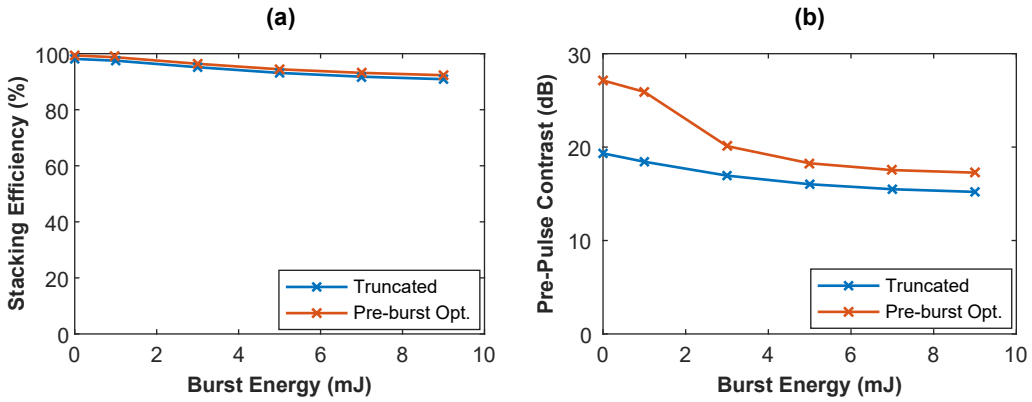

Figure 2.13 : Theoretical stacking efficiency and pre-pulse contrast vs. energy for the burst shapes shown in 2.11 both with and without pre-burst optimization.

post-pulses, which are generally not an issue in laser-matter interaction experiments. For this reason this is referred to as "post-pulse" optimization and simulation results for a 4+4 multiplexed stacker are shown in Fig. 2.14, for both the R = 57% current implementation as well as a single cavity with a R = 75% beamsplitter. The linear, time-invariant nature of stacking means any cavity can be chosen to have the different reflectivity beamsplitter.

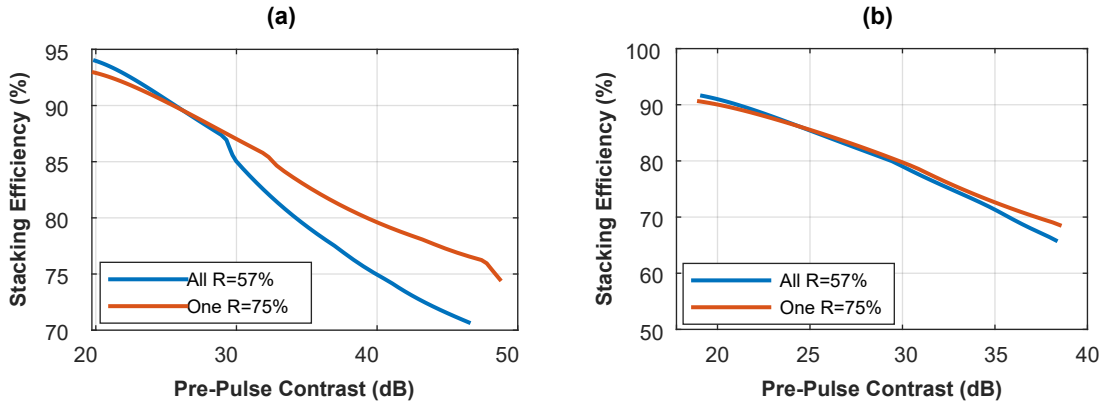

Figure 2.14 : Post pulse optimization for: (a) the 5 mJ equal-nonlinearity burst shape, and (b) the 9 mJ equal-nonlinearity burst shape.

These results show that pre-pulse contrasts above 30 dB are theoretically possible with only a 10% reduction in stacking efficiency. In addition, letting all the cavity beamsplitters vary reflectivity can lead to further optimization, applicable for systems that will be run only at one power level and burst shape. For further discussion of these calculations and implications for stacking see [81].

With recent development of high-efficiency pulse-cleaning techniques that increase contrast by at least 40 dB and can handle Joule-level energies, pulse stacking will be optimized for efficiency over pre-pulse contrast in all but the most stringent applications, such as solid or gas targets where 60-80 dB contrast is needed.

2.5 Further Effects in Saturated Amplifiers

The equal nonlinearity optimization at the monochromatic limit becomes inaccurate at high gain due to spectral reshaping resulting from the quasi-three level characteristics of the gain medium. The splitting of the lower manifold into three sublevels with varying thermal occupation creates inversion-dependent spectral gain where at lower inversion the less occupied, weaker transitions at 1087 nm and 1140 nm can have higher gain than the many-times stronger transition at 1035 nm. This uniquely affects CPSA because the energy extracting burst: (1) changes the gain significantly, from the small signal limit to full depletion, (2) consists of many pulses, each with a full CPA spectrum, that see the changing gain, and (3) requires all those pulses to preserve the same spectral amplitude and phase for temporal combining. The changing gain spectrum is coupled to a changing refractive index and thus phase through the Kramers-Kronig relations, which further complicates the picture.

2.5.1 Temporally Dependent Spectral Gain

Fig. 2.15 shows the effect of inversion on gain spectrum and the gain-reshaping effect on a 10 nm bandwidth and 30 nm bandwidth. The difference between 50% inversion seen by the first pulse and 10% inversion seen by the last pulse corresponds to 80% extraction efficiency, representative of the saturated amplifiers discussed in this work. For the narrower bandwidth the spectral reshaping is minor and compensatable given the large amplitude tolerances of stacking. For the 30 nm bandwidth, however, the pulse experiences very large reshaping and loss of spectral content, which will lead to a large degradation in stacking efficiency and lengthening of the compressed pulse. Beyond

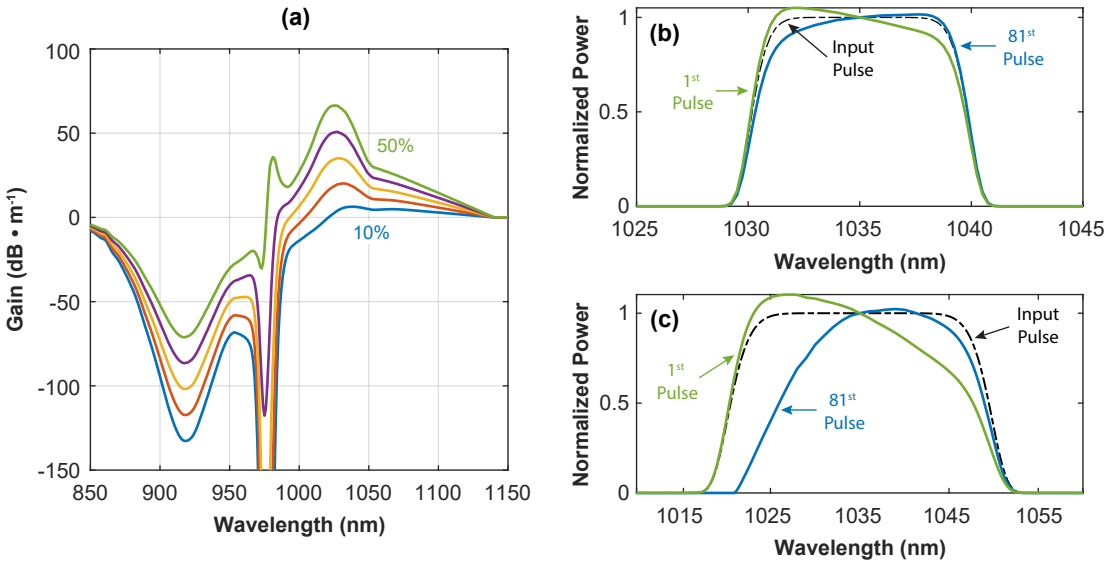

Figure 2.15 : Effect of inversion on gain spectrum in Yb:Glass: (a) Gain for different increasing fractional inversion from 10% to 50% in steps of 10%, (b) and (c) gain reshaping effects on 10 nm and 30 nm spectra, respectively, for 10% (blue) and 50% (green) fractional inversion shown normalized to the amplitude of the 1035 nm center wavelength. The initial spectrum is shown as a dashed black line in both.

the change in spectrum itself this effect complicates the equal-nonlinearity burst shape by introducing intra-pulse varying effective length and thus nonlinear phase. More than spectral shaping this effect degrades stacking, even for small changes in spectrum, and cannot be compensated for by changing the burst shape. It is important emphasize that this phase shift is separate from the Kramers-Kronig phase shift induced by the resonant refractive index.

Control of individual pulse spectrum is necessary to compensate spectral reshaping, requiring at least 1 GHz control speed, far beyond the capabilities of current pulse shaping which controls integrated spectrum. However, in a CPA system the spectral-temporal mapping means that a fast temporal modulator could be used for the same purpose: amplitude and phase EOMs are commercially available up to 30 GHz with 10 ps rise/fall time giving up to 100 points of control across the spectrum of each pulse. Integrating 30 GHz control electronics is possible but very expensive; work has been done showing that the current 5 GHz electronics provide sufficient control of a 1 ns chirped pulse containing 10 nm of spectral content; when feedback on the pulse shape (measured with a 50 GHz oscilloscope) was implemented the gain-induced spectral reshaping was compen-

sated along a 81 ns CPSA burst [35]. For spectral content of 30 nm or above in the same 1 ns chirped-pulse duration faster electronics will be needed.

Simulations show that equalizing the pulse shape (spectrum) at the output of the amplifier has a major reduction on the nonlinear phase accrual but some residual nonlinear phase remains [35]. Further control can be done utilizing the same spectro-temporal mapping of the chirped pulses, just with a fast phase modulator to directly pre-compensate the residual nonlinear phase. Instead of spectral shape, stacking efficiency or compressed pulse duration would be used as a merit function. With control over the burst shape, pulse spectrum and pulse phase high stacking efficiency and bandwidth limited compression is achievable even at full amplifier extraction.

2.5.2 Effect of the Resonant Refractive Index

Amplifier gain is intrinsically linked to refractive index through the Kramers-Kronig relations [10]. A varying gain spectrum creates a varying refractive index and thus phase shift, which could potentially affect temporal combining under high saturation. In the literature this changing phase with inversion is known as "resonant nonlinearity" and has been theoretically analyzed and experimentally measured but not in a temporal combining context.

Experimental investigations of resonant phase shifts in fiber amplifiers discovered a large, spectrally independent phase that did not fit the theory from the 976 nm transition [82]. This was eventually attributed to the Yb^{3+} resonances in the UV which have oscillator strengths several orders of magnitude larger than those in the near IR [83]; the theory based on this assumption matches the data fairly well [84]. This is the dominant effect over all others and the refractive index change is directly proportional to the occupancy in the upper laser level N_2 [84], where Q is a constant and S encodes the oscillator strength and the transition line-widths for the transitions of interest.

$$\Delta n(t) = QS \times N_2(t) \tag{2.11}$$

The phase shift is calculated by integrating this Δn along the fiber; however, there is not accurate

spectroscopic data for Yb:Glass relating the UV transitions to the 976 nm transition, making calculating the absolute magnitude difficult and error prone. For single mode fiber estimates give about a $3\,\mathrm{rad}\cdot\mathrm{m}^{-1}$ phase difference between fully inverted and un-pumped fiber for a signal at 1035 nm [84].

The lack of dispersion of this phase shift at 1035 nm leads to a simple disruption of the stacking phase profile. This can be easily compensated through the degrees of freedom in stacking. As the phase shift follows the depletion of the upper laser level the main effect will be a linear ramp along the pulse burst, which is simply a cavity timing change. This can be compensated for by adjusting either all the stacking cavities or offsetting the induced phase ramp by changing the oscillator cavity length. Phase deviations from the linear ramp can be compensated by changing the phase applied to each pulse in the stacking burst. This can be done actively by dithering the individual pulse phases while using the stacked pulse intensity as a merit function. With these two methods of compensation the spectrally-independent phase can be fully compensated.

The dispersive phase shift due to the transition and split levels at 976 nm are likewise hard to estimate but is expected to be an order of magnitude lower than the non-dispersive phase shift. This spectral phase adds to any induced by spectral amplitude reshaping and implementation of a fast phase EOM, as described above for correction of residual spectral phase after spectral amplitude correction, will also correct this phase.

2.6 Experimental Design of a CPSA System

The design of a laser system for validation of the CPSA technique consists of several building blocks: (1) burst generation and pulse stretching, (2) amplification and down-counting, and (3) temporal combining and pulse compression. The goal is to create a low-energy burst of individual pulses with appropriate phases, stretch the pulses form an continuous burst, amplify the burst to high energy while preserving the individual pulse phase and spectra, temporally combine to a single pulse and compress this single pulse to the bandwidth limit. The general design is shown in

Fig. 2.16; each building block for a 81→1 pulse system will be described in detail here though it is important to note this general structure can be used for an arbitrary number of pulses.

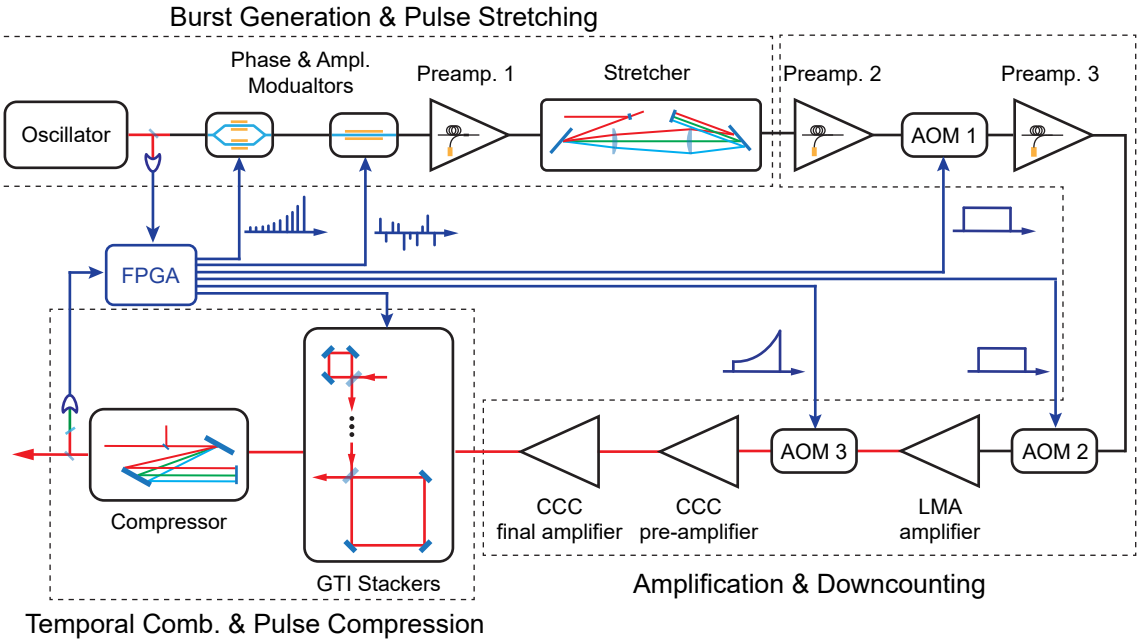

Figure 2.16 : CPSA system layout with dashed lines showing the building blocks.

2.6.1 Burst Generation and Pulse Stretching

Pulses are generated in a 1 GHz fiber oscillator [85] that provides 400 pJ, 75 fs pulses with a slight negative chirp which are then coupled into single-mode fiber and then spread to 10 ps (to lower peak power) over 10 m of propagation. These pulses then enter an amplitude EOM that picks a 81-pulse burst at 1 MHz burst repetition rate, suppressing all the other pulses, after which a phase EOM applies a specific phase to each pulse. The modulator speed is limited to 5 GHz by the field-programmable gate array (FPGA) applying the voltages but the pulses are short enough to appear as delta functions that see no intra-pulse variation in amplitude and phase. After modulation the 3 dB insertion loss of each modulator and a fiber coupled isolator is compensated for by a single mode fiber pre-amplifier. The pulses are then stretched to 900 ps using 43 ps^2 of dispersion from a Martinez-style pulse stretcher with a 1800 $l \cdot mm^{-1}$ grating imposing a 11 nm hard spectral cut

centered around 1035 nm. The pulses are stretched nearly into each other, forming a nearly 81 ns long burst.

Amplitude shaping to prescribe the equal-nonlinearity burst is partially done with the amplitude EOM; however, care must be taken to maintain pulse peak power several orders of magnitude above the background ASE. If the amplifier is unsaturated at any point in the burst in-band ASE will be imprinted on the pulse train and cannot be rejected until the temporal combining step, after it has consumed stored energy from the final amplifiers. This requires the lowest-energy pulse in the burst to have above 1 pJ; due to losses in modulators the pulse with maximum transmission will have only 30 pJ, limiting the burst front-to-back contrast safely applied in the modulator to 13 dB, requiring further shaping downstream.

2.6.2 Amplification and Down-counting

Following stretching, the pulse burst is amplified in two SMF pre-amplifiers and down-counted to 100 kHz. At this point the burst energy is 3 µJ—too high for the 6 µm core single-mode fiber—so the following acousto-optic modulator (AOM) that downcounts to 10 kHz and associated isolators are in free-space. The next amplifier is a 25 µm-core LMA fiber amplifier that increases the burst energy to 15 µJ which is then down-counted again in a 1 ns rise-time AOM to the final rep-rate of 1-10 kHz. This AOM cuts CW ASE as well as doing final burst shaping. At this point a 1 m length of 85 µm-CCC fiber amplifier increases the burst energy to the seed level required for the experiments, from 100 µJ to 2 mJ.

The final amplification stage is 1.8 m of CCC fiber free-space counter-pumped with a 400 W, 976 nm fiber-coupled, wavelength-stabilized diode laser. Circular polarization is used in the amplifier to reduce nonlinearity. The output energy is controlled by varying the pumping level, with output up to 10 mJ.

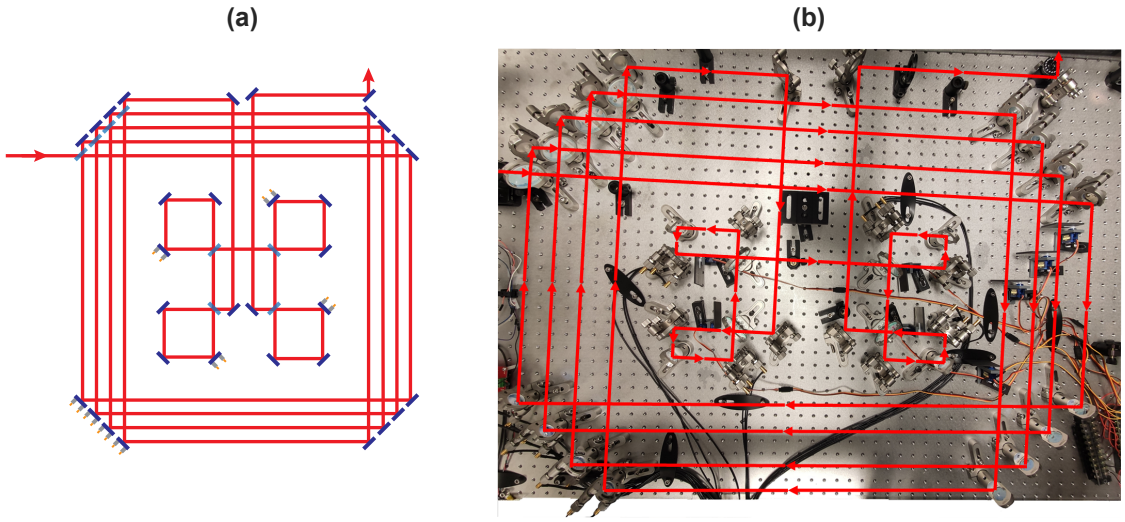

Figure 2.17 : 4+4 multiplexed nested stacker configuration: (a) schematic and (b) picture from the laboratory. The beamsplitters are all R = 57% and the last mirror in each cavity has a 3-axis piezo mirror. The setup fits on on 5' x 4' breadboard.

2.6.3 Temporal Combining and Pulse Compression

The temporal combining system, as described in Sec. 1.13, is a 4+4 multiplex for combining 81 pulses and is nested to reduce footprint, as shown in Fig. 2.17. The last mirror in each stacker cavity has a 3-axis piezo mount for controlling cavity phase and far-field alignment. The pointing into the stacker system is stabilized using a quadrant-photodiode.

The compressor is in Treacy configuration utilizing two 1740 $l \cdot mm^{-1}$ dielectric reflection gratings in double pass. The compressor is additionally folded with a flat mirror to optimize table space. The measured efficiency is 84%, and with a beam diameter of 1 cm the damage threshold approaches 100 mJ. The precise average power handling of the gratings is unknown but they are expected to handle a kilowatt, two orders of magnitude more than gold gratings [1].

2.6.4 Control System

A FPGA-based control system provides triggers and waveforms to the AOMs and EOMs, locks the amplitude EOM bias and and controls the stacking cavities. This FPGA is clocked directly off the

[1] Private communication with Jay Dawson, LLNL

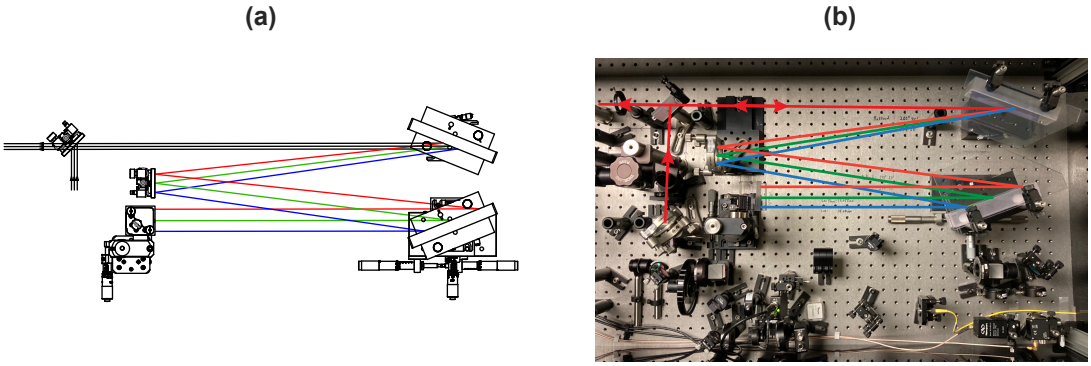

Figure 2.18 : Dielectric Grating Compressor. (a) AutoCAD design, (b) picture from the laboratory showing compressor with associated diagnostics. The compressor and diagnostics fit on a 2' x 4' breadboard.

oscillator, providing perfectly synchronous waveform application and data acquisition. A 1 $Gs \cdot s^{-1}$ analog-to-digital converter (ADC) provides direct reading of the stacking burst so that the peak-power of the 81^{st} pulse can be optimized to stabilize stacking. For future optimization the pre-pulse amplitudes may be used with machine-learning algorithms to optimize stacking efficiency. Further information about the control system can be found in [81, 86].

The oscillator rep-rate is locked by heterodyning a sine wave generated by low-pass filtering a photodiode at the output of the oscillator cavity with a up-counted 10 MHz rubidium frequency standard. The beat note is filtered from the RF mixer and then locked by a proportional-integral-derivative (PID) controller that modulates the oscillator pump power. The pump power modulation is small enough to have no impact on the oscillator output power or modelocking quality. This locking removes all phase noise on the pulses slower than 100 kHz, in effect reducing stacker cavity stabilization to compensating thermal drifts of optomechanics, which are much slower than the 150 Hz stacker cavity stabilization bandwidth.

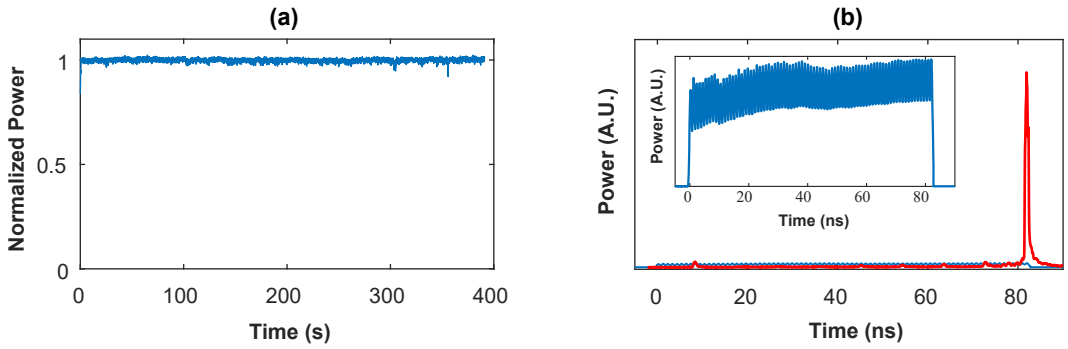

Figure 2.19 : Results of stacking at low power using the signal from a single-mode preamplifier: (a) stability trace showing stacked pulse amplitude over 375 s, and (b) stacked pulse photodiode trace with inset showing the input burst. The stacking efficiency is 84% and the temporal stability is 0.7% NRMSE.

2.7 Experimental Results

2.7.1 Low Power Validation Experiment

Validation of stacking is done at low-power with a burst energy of 3 µJ using the signal from the last single-mode pre-amplifier. This energy is low enough to avoid any significant nonlinear phase accrual so an equal-amplitude burst shape can be used. This experiment gives a upper bound for high-energy stacking and allows benchmarking of alignment procedures. Alignment of the stackers is not within the scope of the thesis—in brief, the initial alignment is done with a camera measuring the near-field and far-field beam overlap from each cavity. The far-field alignment is then fine-tuned using an automated algorithm, and the cavity timing is manually set by using spectral interference of chirped pulses. To engage the stabilization loop first the parameter space is scanned using a Lissajous scan; once the global maxima is found a SPGD algorithm is used to climb the peak and maintain stabilization.

The most important parameter for stacking is the stacking efficiency η_{stack}, defined as the energy in the stacked pulse (in this case, the 81$^{\text{st}}$) divided by the total energy after stacking. Measurement requires resolving energies of pulses 1 ns apart, which is best done post-compression with a fast photodiode. All the pulses are much shorter than the photodiode rise time, creating a signal directly proportional to the energy in the pulse regardless if the pulses vary slightly in compression or

spectral shape. The signal on the photodiode must be small to avoid eliciting a nonlinear response, and for this reason it is sometimes difficult to resolve the pre-pulses below the photodiode noise floor. In this experiment the stacking efficiency is measured up to 84%.

$$\eta_{\text{stack}} = \frac{E_{stacked}}{\sum_i E_i} \tag{2.12}$$

Results are shown in Fig. 2.19. The stabilization of the GTI cavities removes all phase drift and brings the output noise to the amplitude noise limit, achieving near-perfect stabilization. The pre-pulse contrast is 16 dB, very close to the maximum theoretical 18 dB for a truncated burst. The difference between the theoretically predicted stacking efficiency of 96% and the experimentally measured value of 84% could have several potential causes, including small alignment and collimation errors. The most likely, however, is the phase profile applied by the phase EOM, which currently is set to the theoretical values calculated from stacking simulations. Work is ongoing to introduce an optimization loop that will optimize the phase profile using stacked pulse intensity as a metric. This optimization will also correct for any resonant refractive index differences introduced by saturated amplification at high energy.

$$\eta_{\text{throughput}} = \frac{P_{\text{out}}}{P_{\text{in}}} \tag{2.13}$$

The throughput efficiency of the stacker system $\eta_{\text{throughput}}$, defined as the fraction of the average power that exits divided by the fraction that enters, is independent of stacking efficiency or even coherence of the input beam; GTI cavities impose periodic phase variation but have unity power reflection, with loss coming from deviations from "perfect" HR and AR coatings. The AR coatings on the partial-reflector (PR) mirrors face outward from the cavity, interacting with the beam twice per element, and to first order the HR mirrors in the cavity interact with the beam once. In addition to the 3 HR coatings and 1 PR coatings in each cavity there are 9 external HR mirrors, leading to a total of 16 AR coating interactions and 33 HR coating interactions for the 4+4 GTI multiplex used in this work. For standard quality R = 99.5% HR mirrors and R = 0.5% AR coatings the stacker

transmission will be $\eta_{\text{throughput}} \approx 0.995^{16} \times 0.995^{33} = 78.2\%$; for high quality R = 99.9% HR coatings and R = 0.2% AR coatings this improves to $\eta_{\text{throughput}} \approx 93.7\%$, illustrating the need for high-quality coatings. Scattering loss from the PR coating can additionally reduce the transmission but this is generally negligible for ion-beam sputtered coatings [87]. Currently we use high-quality coatings and measure a throughput of 90.5%, close to the estimated value.

2.7.2 Energy Scaling Results

The effect on stacking efficiency of increasing amplifier saturation is experimentally tested by increasing the energy level from 1 mJ to 9.5 mJ in the final amplifier stage by increasing the pump level from the final pump diodes. Compared to the low-power experiment this requires traversing several more pre-amplifiers which are kept at constant current to keep the seed level constant, and another AOM, which is used to downcount to 2 kHz for this experiment and to help shape the burst. The burst at each set-point is shaped by measuring the amplified burst with a 22 GHz photodiode and a 50 GHz oscilloscope and then adjusting the amplitude EOM and last AOM to match to the theoretical burst shape for equal nonlinearity. Once these burst shapes are adjusted the EOM and AOM profiles are stored in the FPGA and are repeatable day-to-day as long as the pre-amplifiers are all run at the same pump power. The results of this is shown in Fig. 2.20; the deviation from the proper burst shape at the highest set-point of 9.5 mJ is purposefully done as the spectral shape is narrowing and thus the peak power is increased above what is predicted by the monochromatic model. At highest energy of 9.5 mJ with a 250 µJ seed the extraction efficiency is $\eta_e = 88\%$, representing near complete energy extraction.

The stacker alignment must be adjusted slightly from low power. First the large-scale timing is adjusted to compensate for the resonant refractive index effect by moving the oscillator cavity slightly, after which each cavity timing is fine tuned. Finally, the automated far-field alignment is run by using a single-cavity stacking profile that is appended after the main bursts. For highest efficiency this alignment is done at each current set-point, after which stacking is ready to be engaged, using the same algorithm as at low-power. The results from the stacking are given in Fig.

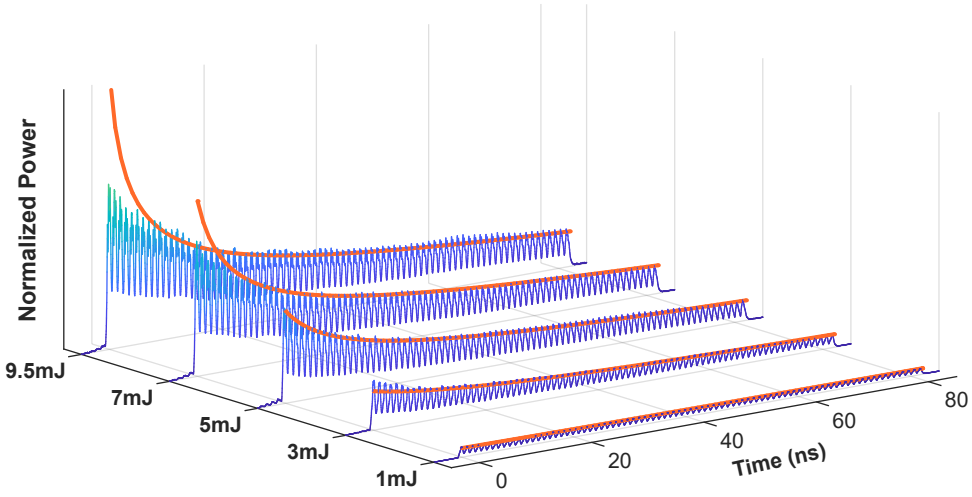

Figure 2.20 : Measured input burst shape to stackers and proper designed burst shape (orange) for the energy levels tested in this experiment, normalized to peak power to show the relative difference between the shapes.

2.21, all normalized to the peak of the 81st pulse to illustrate how the pre-pulses evolve at each set-point.

The compressor spacing and angle is adjusted at each energy set-point to compensate for any residual phase; the angular adjustment is generally small, around 0.1-0.2°. The pulses are measured with a homemade non-collinear second harmonic generation (SHG) autocorrelator and detection is done with a amplified photodiode. Due to the low rep-rate of the signal the scan must be very slow (1 Hz) and a 2nd order low-pass RF filter with 500 Hz cutoff must be used to smooth the signal measured on the oscilloscope. Results from the autocorrelation are shown in Fig. 2.22 along with the calculated nonlinear phase at each set-point; stacking does not change the traces. The pulses all remain ultrashort, increasing the pulse duration only slightly from 320 fs at 1 mJ to 345 fs at 9.5 mJ, but the large growth of the wings indicates the presence of nonlinear phase.

Additionally, the use of a fast photodiode for measuring the pre-stacking bursts allows for direct viewing of the spectrum of each individual chirped pulse, which cannot be done with a spectrometer that integrates and gives an average burst spectrum. Plotting the first and last pulse in the burst overlapped gives time-resolved viewing of spectral effects, as shown in Fig. 2.23.

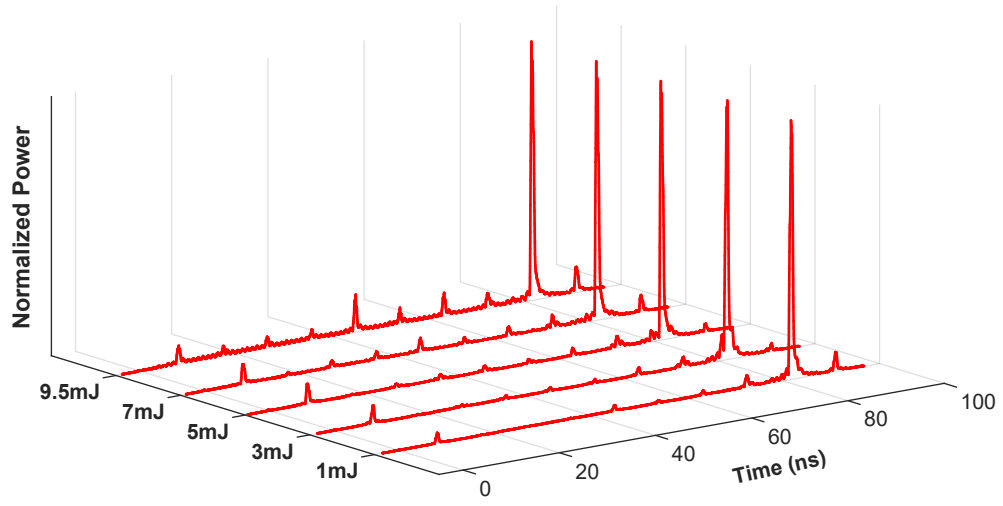

Figure 2.21 : Measured results of stacking at multiple energy levels. Each trace is normalized to the peak of the 81st pulse and not to the contained energy.

2.8 Discussion

The results from the energy scaling experiment are summarized in Table 2.1, along with the low-energy result. Stacking efficiency at 1 mJ is comparable to that at low power and maintains above

Burst Energy	Stacking Efficiency	Compressed FWHM
3 µJ	84%	270 fs
1 mJ	79%	321 fs
3 mJ	77%	316 fs
5 mJ	73%	313 fs
7 mJ	71%	317 fs
9.5 mJ	58%	335 fs

Table 2.1 : Table showing stacking efficiency and compression as fiber output energy increases. The reduction in pulse FWHM at 3 mJ and 5 mJ is attributed to a ±3 fs measurement uncertainty in the autocorrelator.

70% up until the 9.5 mJ set-point, where it drops off substantially. The loss in stacking efficiency comes largely from energy left in every 9th pulse, indicating performance degradation in the long GTIs. This is expected for any phase or alignment errors, as the long cavities are far more sensitive than the short cavities due to their 9x longer round trip time. Compression follows a similar

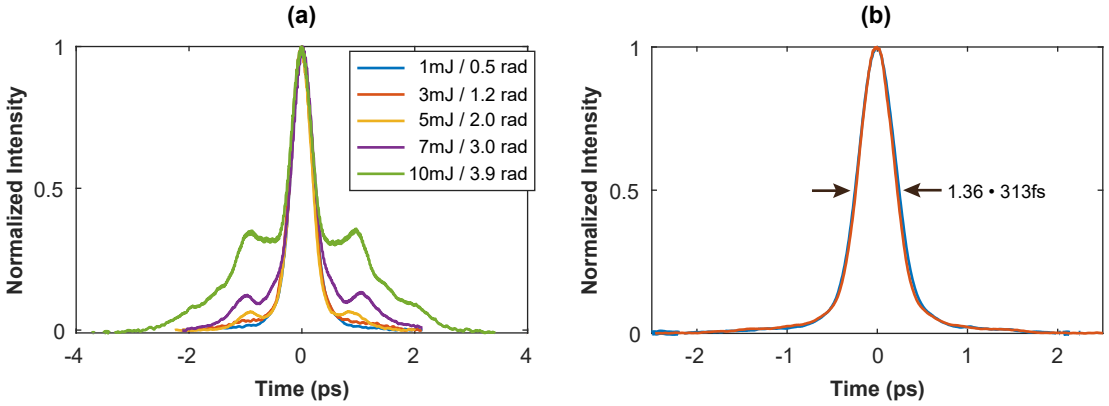

Figure 2.22 : Measured autocorrelation traces for: (a) the energy levels tested in the stacking experiment, along with the calculated nonlinear phase, and (b) a comparison of stacked and un-stacked traces at 3 mJ.

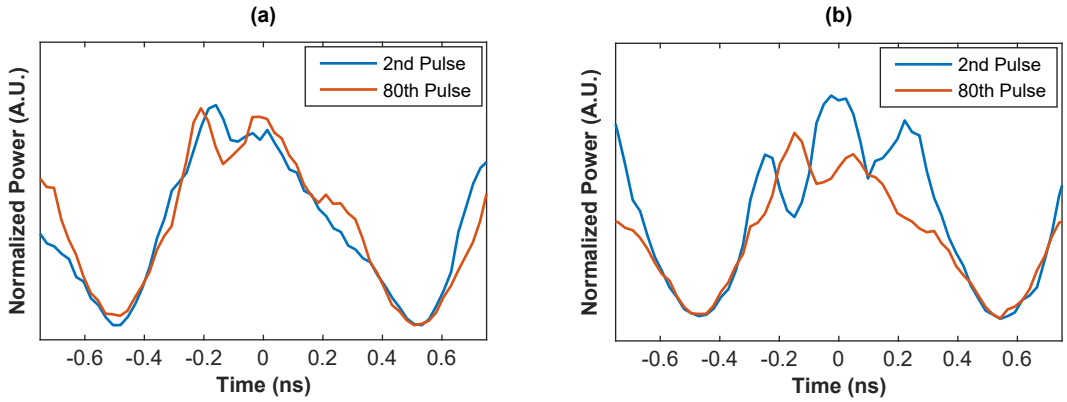

Figure 2.23 : Overlay of 2nd and 80th pulses with normalized amplitude for: (a) 5 mJ burst shape and (b) 9.5 mJ burst shape showing significant spectral reshaping. Note that as the pulses are up-chirped the later times contain the shorter wavelengths.

trend to stacking efficiency, with the difference that the 3 µJ low power pulse is shorter—this is just due to gain-narrowing in the high-energy amplifiers and is expected in this experiment. The compressed pulse FWHM does not tell the whole story, however, as the wings generated at 9.5 mJ are substantial and indicate nonlinear phase accrual higher than the 3.9 rad predicated from the designed burst shape in Sec. 2.4.3. The spectral reshaping seen in the chirped pulses in Fig. 2.23 indicates that the monochromatic assumption used for the equal-nonlinearity burst calculation is no longer valid at highest level of gain, even for the relatively narrow 10 nm of bandwidth. Use of a fast amplitude modulator to control the pulse spectral reshaping will be needed at the highest

level of gain and extraction.

Nonetheless this result shows a record amount of energy from a fiber amplifier into a single pulse, far above what is achievable in single-pulse fiber CPA and surpassing the DPA results.

2.9 Ongoing and Future Work

The results in this section validate the CPSA technique in a heavily saturated amplifier and indicate the points at which stacking degrades. The future work on this experiment can be broken into two thrusts: (1) refining the results with the goal of achieving high stacking efficiency and cleaner compression at 10 mJ and (2) extending the results to broader bandwidth (shorter pulse duration) and higher average power.

It is clear that the nonlinearity due to spectral reshaping degrades stacking efficiency and compression; there are three approaches to reducing this effect. First, as mentioned several times, the use of a fast EOM on the chirped pulses can compensate the reshaping and thus a large fraction of the induced nonlinear phase deviation from the monochromatic equal-nonlinearity calculation. Second, the gain fiber should be reduced to the shortest length possible without significantly reducing the stored energy—this will reduce overall phase accrual. Measurements indicated that this fiber length was appropriate for balancing ASE and stored energy, but further investigation is needed. Third, reducing overall nonlinearity can be done by increasing the burst length and thus reducing the individual pulse energy. For example, doubling the burst length to 162 ns (162 pulses) would effectively half the nonlinear phase accrual. While this has no effect on the saturation-induced spectral reshaping, it decreases the accrued nonlinearity and, given that the actual change in spectrum is small, would likely improve temporal combining and compression significantly. All of these paths are valid and must be investigated, especially as there is potential for refining this fiber design to store up to 20 mJ and for the advent of larger-core CCC fiber that stores > 50 mJ [71].

The next steps for this experiment consist of moving to 30 nm of bandwidth, enough for 110 fs

pulses. This bandwidth will require compensation of spectral reshaping using a fast EOM at energy levels much lower than the 10 nm experiment, and thus all of the above-mentioned optimizations to fiber and burst length should be done first. For the CPA aspects an Offner stretcher that preserves this bandwidth while stretching to 900 ps has been built and validated; the current compressor will also accommodate this bandwidth with just changing the grating spacing. A broadband dispersion compensator leveraging the spatial-spectral coupling in the Fourier plane of a grating pair with cubic (coma) and quadratic (spherical) aberrations has been shown to compensate residual 3rd and 4th order dispersion from 50 m of fiber [35]. Compensation of gain-narrowing at this broadened spectrum will require both the fast EOM mentioned above as well as potentially additional gain-flattening filters in-between high amplification stages, a common technique in high-gain fiber systems [34].

The last step for these experiments is to extend to 10 kHz rep-rate for 100 W of average power from the fiber. This only requires thermal management in the final amplifier stage; the control system and pre-amplifiers can all be adjusted easily. As average power in the fiber amplifier scales the transverse-mode instability (TMI) thresholds must be investigated, especially for rep-rates approaching the 50 kHz desired for LPAs.

With these improvements we expect a single fiber to provide in excess of 10 mJ at 110 fs or about 90 GW of peak power with 100 W of average power, forming a basis of CBC multi-TW peak, multi-kW average power laser systems with low number of combined fibers.

CHAPTER 3

Energy Scaling of CPSA using Coherent Beam Combining

3.1 Introduction

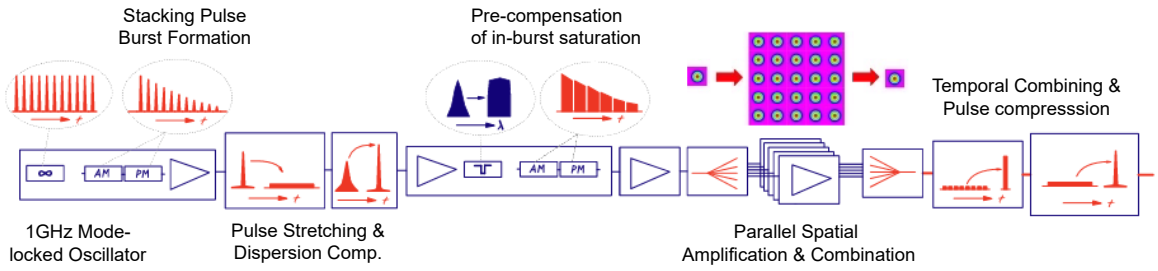

Figure 3.1 : Conceptual design of spatio-temporally combined CPSA and CBC system, with dispersion and saturation compensation for pulse durations below 100 fs. Figure courtesy of Almantas Galvanauskas.

Increasing energy in a CPSA system past the single-fiber storage limit requires parallel array scaling using coherent beam combining (CBC). This is shown conceptually in Fig. 3.1, where dispersion compensation and saturation control are included to preserve bandwidth for pulse durations below 100 fs. The CBC array splits and amplifies many parallel beams before coherently recombining them using either filled-aperture or tiled-aperture methods. Tiled-aperture combining has succeeded in combining large numbers of amplifiers but has a theoretical maximum achievable efficiency of 62% [36], with values closer to 50% in practice [39], and thus is not suitable for future high-efficiency laser systems. Filled aperture combining using amplified beams from optical fibers

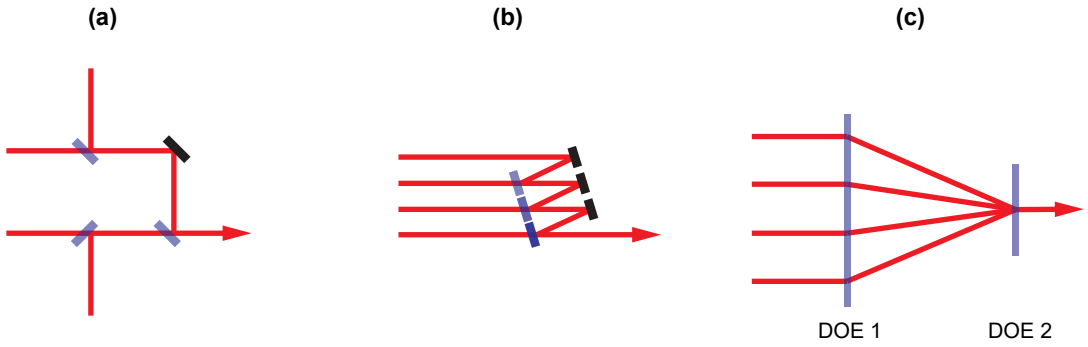

Figure 3.2 : Spatial arrangements for filled aperture combining: (a) binary-tree, shown for 45° intensity beamsplitters but applicable for TFPs, (b) segmented-mirror setup using R/T 50/50, 70/30, and 80/20 beamsplitters, and (c) two DOEs for ultrashort pulses.

regularly achieves efficiencies above 90% and as such is appropriate for this work. Filled-aperture combining is typically done in one of three ways: (1) polarization combining [88], (2) intensity combining, or (3) diffractive optical element (DOE) combining [89].

Polarization combining relies on orthogonally-polarized beams incident on PBS or thin-film polarizer (TFP) elements that transmit/reflect all the incident power into the combined port but only generate a stable combined polarization when the phases are locked. The required binary tree beamsplitter arrangement consumes a large tabletop area, and in most implementations balanced detector after each element are used for phase locking, complicating stabilization [90].

Intensity combining uses intensity beamsplitters that reflect/transmit a fixed fraction of the field and only maximize the power in the combined port when the phase is locked. This can be arranged in a binary-tree fashion like polarization combining but also has the potential to be packaged into a much smaller segmented-mirror combining element [91], reducing table-top space significantly; additionally analysis suggests that intensity beamsplitters are more amenable to 100 kW-level average powers than TFPs [92]. Phase-locking is done with a single-detector at the output using LOCSET or SPGD algorithms with the potential to add photodiodes in each dump-port to generate multiple-parameter information for machine-learning algorithms.

DOE combining is successfully used at high average power (many -kW) for narrow-band (CW) beams [93] for directed energy applications. With ultrashort pulses the angular-dispersion induced

pulse-front tilt requires two DOE elements [89] and can theoretically maintain achromaticity required for pulses down to 30 fs duration [94]. In the two-element design, efficiency loss due to improper beam phasing results in a unique pattern in the far field that can be used for machine-learning stabilization approaches [95, 96]. However, the separation between DOE elements needed for ultrashort, high-energy combining of many channels is large, and the peak-power handling is not yet fully known.

In this work intensity beamsplitters are used in the binary-tree arrangement with the understanding that in the future more compact layouts will be used. The binary-tree arrangement allows for easy proof-of-principle alignment and provides necessary insights to system design without changing any fundamental physics. This chapter first presents the alignment tolerances and procedures for high-efficiency CBC, then presents several methods of automatic spatial alignment, necessary for future high-channel count systems, along with experimental measurement of phase shifting piezos. Finally the experimental design and integration of a 4-channel CBC array into the existing CPSA system is described, culminating in results achieving 89% spatial combining efficiency from 4 parallel amplifier channels each operating at 7 mJ, near the extractible-energy limit. The output beam, containing 25 mJ / 50 W in an 81-pulse burst, is then temporally combined into a single pulse with 70% efficiency, maintaining the single-channel efficiency results. A slight increase in temporal stabilization amplitude noise at the highest energies indicates that incomplete CBC phase stabilization under high phase noise conditions can detrimentally influence the convergence of the stacking algorithm, giving an experimental understanding of the requirements for CBC algorithm speed and indicating that faster loop-speed may be needed for future experiments. This will be achieved by increasing pulse repetition-rate which also accomplishes power scaling towards 100 W / channel. This result is the first step in scaling the energy from a fiber laser system operating at the extractible energy limit, establishing the way for a 12-channel system that can provide 100 mJ of energy and, in the future, a 10 J-class system with only 10^3 amplifiers.

3.2 Analysis of Efficiency Errors and Alignment Procedures

Efficient combining of the amplifiers in the CBC array is required not only for achieving high WPE but also because interference errors manifest themselves as deviations from a ideal beam, adding noise at the input of the temporal combining. It is then essential to understand efficiency errors, their impact on the temporal and spatial output of the array, and methods of active control.

In a coherent combination system N beams with different electric field profiles $E_i(x, y, z, \omega, t)$, $1 < i < N$, are added together such that when the beam is directed onto a target or measured with a square law detector it is indistinguishable from a single beam of N times the amplitude. In general the beams to be combined can be written in terms of the electric field and separated into spatial (x, y) parts and spectral/temporal (ω, t) parts. To accurately include propagation effects both must have z dependence; in the time domain this describes dispersion and in the spatial domain this describes diffraction.

$$\hat{\mathbf{E}}(x, y, z, \omega, t) = [E_{0x}\hat{\mathbf{x}} + E_{0y}\hat{\mathbf{y}}] \times \tilde{u}(x, y, z) \times \tilde{a}(\omega, t, z) \tag{3.1}$$

For high quality interference the beams must be matched in all their parameters in (x, y, z, ω, t) to a sufficient tolerance. Simple scaling laws for small misalignments of each parameter can be derived individually, along with tolerances for high-efficiency combining [97].

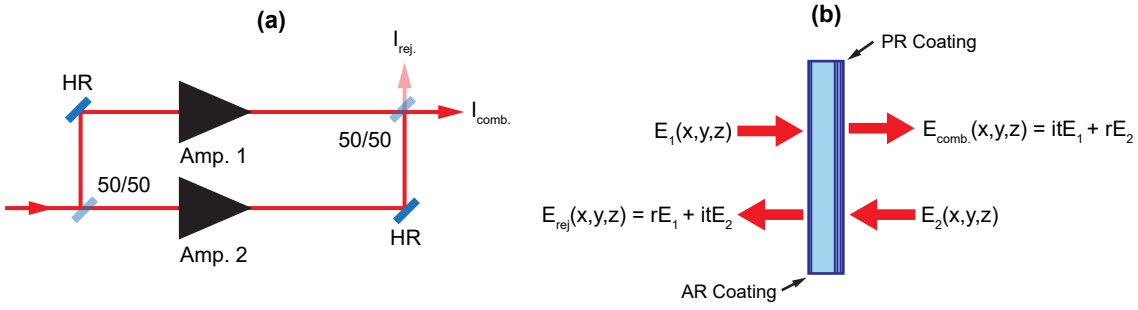

Figure 3.3 : Theoretical basis for error analysis: (a) a Mach-Zehnder interferometer with an amplifier in each arm, and (b) the model of the output beamsplitter as a four-port interference device with fields entering and exiting from each side.

In the following analysis an amplifying Mach-Zehnder interferometer will be used as the con-

ceptual basis; each arm contains an amplifier that can, in the fashion of the Sec. 2.5.1, shape the spectrum and add phase of its own. It will be assumed that the amplifiers act identically so that they, along with any phase shift on reflective elements, can be ignored. The interference on the output beamsplitter can be analyzed in a "four-port" device format, where the each side has a entering and exiting field. This leads to the same final result without the nuisance of having to rotate k-vectors by 90°. Additionally the vector dependence is dropped, assuming the polarization is linear along one axis.

Following each analysis the current alignment procedure will be discussed, with the exception of active alignment methods which will be covered later. For the tolerances the bandwidth for a 330 fs, $\lambda_0 = 1035$ nm pulse will be used along with the current of $2w_0 = 1.8$ mm beam size.

3.2.1 Phase Errors

First consider the effect of a phase difference $\Delta\phi$ between the two amplifier arms, neglecting any group delay differences, valid for path lengths that are matched to well within the coherence length. Additionally dispersion is neglected and the spatial fields $\tilde{u}(x, y, z)$ are assumed to be identical and are left off the analysis. The combined field after the 50/50 power beamsplitter can be written in terms of the fields out of the amplifier.

$$E_{\text{comb.}}(\omega) = \frac{E_0}{\sqrt{2}}\tilde{a}(\omega) + \frac{E_0}{\sqrt{2}}\tilde{a}(\omega)e^{-i\Delta\phi} \tag{3.2}$$

The combined intensity $I_{\text{comb.}}$ can be written as the magnitude squared of the combined field times a constant term $\frac{1}{2\mu_0 c}$ converting electric field to intensity.

$$I_{\text{comb.}} = \frac{1}{2\mu_0 c}|\tilde{a}(\omega)|^2\left[1 + \cos(\Delta\phi)\right] \tag{3.3}$$

To understand the degradation in combining efficiency due to a phase error $I_{\text{comb.}}$ can be divided by its maximum value to get a normalized parameter η, from here on known as the combining

efficiency. For small errors around a peak a Taylor expansion $\cos^2(x) \approx 1 - x^2$ is valid.

$$\eta = \cos^2\left(\frac{\Delta\phi}{2}\right) \approx 1 - \frac{(\Delta\phi)^2}{4} \tag{3.4}$$

For maintaining a combining efficiency of $\eta > 99.9\%$ the phase error must be < 63mrad; at λ = 1035nm this is $\Delta z < 10$nm.

Maximizing the combining efficiency requires finding a location where $\Delta\phi = 2\pi n$, $n \in \mathbb{Z}$. Generally the phase varies in time due to air currents, thermal drifts, changing amplifier pump levels, etc. requiring active stabilization of $\Delta\phi(t)$ to maintain proper combination.

3.2.2 Group Delay Errors

Temporal mismatch of pulse envelopes, or group delay mismatch, causes degradation in interference quality even if the phase is matched $\Delta\phi = 2\pi n$. Even for a strongly chirped pulse the group delay tolerance is dependent on the frequency content of the bandwidth-limited pulse, for femtosecond pulses requiring path length mismatches $\ll$100 fs, even for pulses that are stretched to 1 ns.

The effect of group delay in one arm of the interferometer can be written by adding a term $\exp\left(-i\Delta t(\omega - \omega_0)\right)$ to the spectral domain representation of the pulses which has the effect, when transformed into the time domain, of moving the peak of the pulse envelope by Δt [97]. Assuming all the other terms are constant then the combined field can be written

$$E_{\text{comb.}}(\omega) = \frac{E_0}{\sqrt{2}}\tilde{a}(\omega) \times \left\{1 + \exp\left[-i\Delta t(\omega - \omega_0)\right]\right\}, \tag{3.5}$$

which can then be written in terms of intensity, which varies with a sinusoidal pattern on the spectrum.

$$I_{\text{comb.}}(\omega) = \frac{|E_0|^2}{2\mu_0 c}|\tilde{a}(\omega)|^2 \times \left\{1 + \cos\left[\Delta t(\omega - \omega_0)\right]\right\} \tag{3.6}$$

To analyze the combining efficiency this must be integrated over ω to find the total power in the

combined port $P_{\text{comb.}}$. This requires an analytic form of the spectral shape $\tilde{a}(\omega)$; here a square spectrum centered at ω_0 with full width $\Delta\omega$ is used.

$$\begin{aligned} P_{\text{comb.}} &= \int_{-\infty}^{\infty} I_{\text{comb.}}(\omega) d\omega \\ &= \frac{|E_0|^2}{2\mu_0 c} \int_{-\infty}^{\infty} |\tilde{a}(\omega)|^2 \times \{1 + \cos[\Delta t(\omega - \omega_0)]\} \, d\omega \\ &= \frac{|E_0|^2}{2\mu_0 c} \int_{\omega_o - \frac{\Delta\omega}{2}}^{\omega_0 + \frac{\Delta\omega}{2}} \{1 + \cos[\Delta t(\omega - \omega_0)]\} \, d\omega \\ &= \frac{|E_0|^2}{2\mu_0 c} \Delta\omega \left[1 + \text{sinc}\left(\frac{\Delta t \Delta\omega}{2}\right)\right] \end{aligned} \tag{3.7}$$

Dividing by the maximum value (when $\Delta t = 0$) the combining efficiency can be found. The Taylor expansion $\text{sinc}(x) \approx 1 - \frac{x^2}{6}$ is valid for small errors.

$$\eta = \frac{1}{2}\left[1 + \text{sinc}\left(\frac{\Delta t \Delta\omega}{2}\right)\right] \approx 1 - \frac{\left(\frac{\Delta t \Delta\omega}{2\sqrt{3}}\right)^2}{4} \tag{3.8}$$

This shows that the combining efficiency from group delay mismatch is dependent only on the bandwidth limited pulse duration and the temporal mismatch of the pulses. For a square spectrum this can be further simplified by using the uncertainty principle to relate $\Delta\omega$ to τ_{p0}, the bandwidth limited pulse duration (specified in FWHM fashion), in the form $\tau_{p0} \times \Delta\omega_{\text{FWHM}} \approx 5.565$. The coherence time T_c, defined as the temporal mismatch needed to reduce the combining efficiency from peak to half the incoherent limit $\eta = \frac{1}{2}[\eta(\Delta t = 0) - \eta(\Delta t \to \infty)]$, is $T_c = 0.68 \times \tau_{p0}$. This value for a Gaussian spectrum is $T_c = \frac{1}{2} \times \tau_{p0}$; however, for the same bandwidth-limited pulse duration the Gaussian spectral FWHM is $\sim$2x smaller than the square spectrum.

Using $\eta \geq 99.5\%$ as a criterion for tolerable efficiency loss the group delay can be written in

terms of temporal, free space or phase mismatch.

$$
\begin{aligned}
|\Delta t| &\leq 0.088 \times \tau_{p0} \\
|\Delta z| &\leq 0.088c \times \tau_{p0} \\
|\Delta \phi| &\leq 0.088 \left(\frac{2\pi c}{\lambda_0}\right) \times \tau_{p0}
\end{aligned}
\tag{3.9}
$$

For a 330fs pulse this is a path-length mismatch of $\pm$ 8.7 µm; for a 110 fs pulse it is $\pm$2.9 µm.

For the 330 fs pulse the phase can be locked to any of 17 different peaks and the interference quality will be high. The group delay alignment is fairly tolerant then, and can be done by scanning one arm of the interferometer over a set range and optimizing the fringe contrast by moving the other arm with a translation stage. This is shown after optimization in Fig. 3.4, where a piezo phase shifter is scanned over 11 fringes, the extent of its movement, and the fringe contrast stays constant. The phase control will lock to one of these peaks; if the phase stabilization loses one peak and finds another there will be no interference degradation.

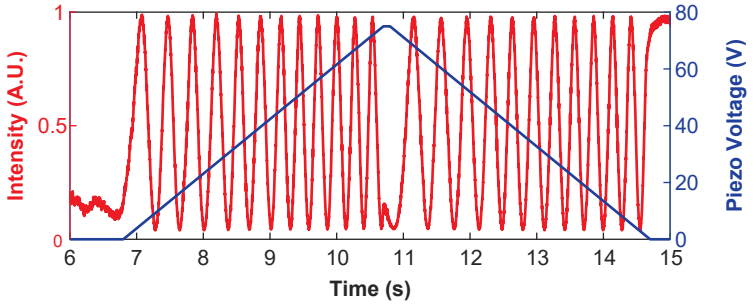

Figure 3.4 : Experimentally measured phase fringes and applied piezo voltage. The alignment is proper in this case and no interference degradation is seen.

Experimentally (for 10 nm bandwidth) once the group delay alignment is set the relative amplifier path length drift does not exceed the 17 fringe limit for high quality interference, even at pumping powers approaching 150 W. This is due to water-cooling of all the amplifier fibers such that their thermal environment is stable, as thermal effects are the most likely to cause large magnitude phase drifts (as opposed to air currents or mechanical vibrations). The refractive index temperature coefficient in fused silica is $\frac{dn}{dT} \approx 1.1{\times}10^{-5}\,^{\circ}\mathrm{C}^{-1}$ for $\lambda = 1$ um [98], so a change of

1 °C along a 1.8 m amplifier will induce a phase difference of 40π rad or 20 fringes, enough to significantly degrade interference quality due to group delay.

For situations where the thermal environment is less stable, such as higher pumping or large amplifier numbers, or for narrow bandwidth where path length tolerance is tighter, automatic alignment of group delay is essential. This will be discussed later.

3.2.3 Group Delay Dispersion Errors

Potentially important for ultrashort pulses is the effect of mismatched group-delay dispersion (GDD) in the amplifier arms. The most likely source is differences in gain fiber length between channels, with small contributions from other sources like differing number of mirror reflections. The analysis is done by applying a phase term $\exp\left[-i\phi''(\omega-\omega_0)^2\right]$ to one of the fields in the amplifier arms, where ϕ'' is the accumulated GDD difference in s^2. The combined intensity can be written as:

$$I_{\text{comb.}} = \frac{|E_0|^2}{2\mu_0 c}|\tilde{a}(\omega)|^2\left\{1+\cos[\,\phi''(\omega-\omega_0)^2\,]\right\} \tag{3.10}$$

Integration over the ω variable requires knowledge of the spectral shape $|\tilde{a}(\omega)|^2$. Assuming a square spectrum of center frequency ω_0 and full width $\Delta\omega$.

$$\begin{aligned} P_{\text{comb.}} &= \frac{|E_0|^2}{2\mu_0 c}\int_{-\Delta\omega/2}^{\Delta\omega/2}\left\{1+\cos\left[\phi''(\omega')^2\right]\right\}d\omega' \\ &= \frac{|E_0|^2}{2\mu_0 c}\Delta\omega\left\{1+\sqrt{\frac{2\pi}{\phi''\Delta\omega^2}}\mathbb{C}\left[\sqrt{\frac{\phi''\Delta\omega^2}{2\pi}}\right]\right\} \end{aligned} \tag{3.11}$$

Where $\mathbb{C}\left[z\right]=\int_0^z\cos\left[\frac{\pi t^2}{2}\right]dt$ is the Fresnel C-integral. Like for the other parameters this can be converted to a combining efficiency by dividing by the maximum value at $\phi''=0$.

$$\begin{aligned}\eta &= \frac{1}{2}\left\{1+\sqrt{\frac{2\pi}{\phi''\Delta\omega^2}}\mathbb{C}\left[\sqrt{\frac{\phi''\Delta\omega^2}{2\pi}}\right]\right\}\\ &\approx 1-\frac{(\phi'')^2\Delta\omega^4}{320}\\ &\approx 1-\frac{\left(2\sqrt{3}\frac{\phi''}{\tau_{\text{p0}}^2}\right)^2}{4}\end{aligned} \tag{3.12}$$

In the last step the relationship for square spectrum $\Delta\omega_{\text{FHWM}} \times \tau_{\text{p0}} \approx 5.565$ is again used. The tolerance for $\eta = 99.5\%$ is $\phi'' \leq 0.0408 \times \tau_{\text{p0}}^2$. Given the GDD of fused silica is 18.6 $\text{fs}^2 \cdot \text{mm}^{-1}$ for a 330 fs pulse centered at 1035 nm the allowable fiber length difference is 24 cm. This is much less than the typical variance of the fiber lengths in the experiment and as such will not have a noticeable effect.

3.2.4 Transverse Overlap (Near-Field) Errors

The effect of spatial errors can be analyzed using the four-port geometry shown in Fig. 3.3. This requires use of an analytical form of the spatial field $\tilde{u}(x, y, z)$. Gaussian beams match the fiber fundamental mode well and are easily mathematically manipulated, making them appropriate for this analysis [10].

$$\begin{aligned}\tilde{u}(x,y,z) &= \frac{w_0}{w(z)}\exp\left[-\frac{(x^2+y^2)}{w^2(z)}\right]\exp\left[-ik_0z-ik_0\frac{(x^2+y^2)}{2R(z)}+i\Psi(z)\right]\\ w_0(z) &= w_0\sqrt{1+\left(\frac{z}{z_R}\right)^2}\\ R(z) &= z\left[1+\left(\frac{z_R}{z}\right)^2\right]\\ z_R &= \frac{\pi w_0^2}{\lambda}\\ \Psi(z) &= \arctan\left(\frac{z}{z_R}\right)\end{aligned} \tag{3.13}$$

In this equation $w(z)$ is the e^{-2} half-width with a minimum w_0, known as the beam waist, $R(z)$ is the phase radius of curvature, z_R is the Rayleigh range and Ψ is the Guoy phase parameter.

In analyzing spatial errors, like temporal errors, it is necessary to integrate over the whole beam profile in the combined port to find the combined power $P_{\text{comb.}}$ and the overall efficiency. For a single Gaussian beam of amplitude E_0 this integration gives a power of $P = \left(\frac{E_0^2}{2c\mu_0}\right) \times \left(\frac{\pi w_0^2}{2}\right)$, which is independent of z.

The first error to analyze is beam displacement in one dimension; this can be done by shifting one beam center by x_0 and assuming the interference is at the beam waist ($z = 0$) [78, 97]. The combined field distribution is

$$E_{\text{comb.}} = \frac{E_0}{\sqrt{2}} \exp\left[-\frac{x^2+y^2}{w_0^2}\right] + \frac{E_0}{\sqrt{2}} \exp\left[-\frac{(x-x_0)^2+y^2}{w_0^2}\right] \tag{3.14}$$

which can be integrated over the spatial variables to find the power in the combined beam as a function of x_0.

$$P_{\text{comb.}} = \left(\frac{E_0^2}{2\mu_0 c}\right) \times \left(\frac{\pi w_0^2}{2}\right) \left[1 + \exp\left(-\frac{x_0^2}{2w_0^2}\right)\right] \tag{3.15}$$

This shows that a mismatch of x_0 in the x-direction degrades the combined power as a Gaussian function. Normalizing the combined power by the maximum achievable when $x_0 = 0$ gives the combining efficiency η.

$$\eta = \frac{1}{2}\left[1 + \exp\left(-\frac{x_0^2}{2w_0^2}\right)\right] \approx 1 - \frac{\left(x_0/w_0\right)^2}{4} \tag{3.16}$$

The use of a Taylor expansion $e^{-ax^2} \approx 1 - ax^2$ is valid for small errors and shows the parabolic nature of the efficiency peak. This tolerance, while fixed relative to the size of the beam, gets easier to achieve in the laboratory frame as beams get bigger; this is a general scaling rule and is opposite of the beam angular alignment.

For the $\eta \geq 99.5\%$ criterion the displacement of the beam x_0 can be $\pm 14\%$ of the beam waist size; for a $2w_0$ =1.8mm beam this is a displacement of $\pm$126μm.

Current laboratory alignment is done using incoherent beams of ASE from the amplifiers (to remove any fringing effects) and overlapping the beams at the combining element on a beam-profiler camera (Dataray WincamD-LCM). The camera has pixel pitch of 5.5 µm, making resolving a displacement of 126 µm easy. Near-field misalignments come from drifts of optomechanical mounts in the system which, as they are close to the combining elements, affect far-field (angular) alignment much more than near-field. This, coupled with the relatively loose tolerances of overlap alignment, means optimization is needed only at the beginning of the experiment and frequently doesn't drift daily unless the laboratory temperature changes significantly. Later, a method for automatic alignment of beam overlap will be given, but is currently of lower priority than angular alignment.

3.2.5 Beam Pointing (Far-Field) Errors

The effect of a k-vector angular mismatch can be analyzed next by rotating Eqn. 3.13 around the x-axis and once again assuming that the beam waists are at the beamsplitter [78, 97].

$$E_{\text{comb}} = \frac{E_0}{\sqrt{2}} \exp\left[-\frac{x^2 + y^2\cos^2(\theta)}{w_0^2}\right] \exp\left[iky\sin(\theta)\right] + \frac{E_0}{\sqrt{2}} \exp\left[-\frac{x^2+y^2}{w_0^2}\right] \tag{3.17}$$

This can be solved through and converted to a combining efficiency, again using Taylor expansions to second order, and using $\theta_{\text{ff}} = \frac{\lambda}{\pi \text{w}_0}$ as the far-field divergence angle of the Gaussian beam.

$$\eta \approx 1 - \frac{\left(\frac{kw_0\theta}{2}\right)^2}{4} = 1 - \frac{\left(\theta/\theta_{\text{ff}}\right)^2}{4} \tag{3.18}$$

For the $\eta = 99.5\%$ criterion the angular tolerance is $\theta \leq \pm 0.14 \times \theta_{\text{ff}}$, or $\pm$ 14% of the far-field divergence angle. This inverse dependence on w_0 means the θ tolerance gets tighter for larger beams; it is harder to align the pointing of larger beams for high efficiency. For $\lambda_0 = 1035$nm and a beam size of $2\text{w}_0 = 1.8$mm the tolerance is $|\theta| \leq 51$ µrad.

Current initial alignment is done by overlapping the beams on a camera 4 m away from the com-

bining element. Given that the displacement (near-field) alignment sets the beams to be $<$126 µm center-to-center at the combining element, aligning all the beam centers within 50 µm in the far field 4 m away puts the maximum angular deviation at 44 µrad, achieving the tolerance. Fine alignment can also be done using the amplified signal (not ASE) and scanning the temporal phase of one of the amplifier arms while watching the spatial fringes in the near-field, where the phase-fronts are flat. For improper angular alignment the fringes will scan left-right or up-down; when aligned properly the beam interferes fully across its width, leading to a spot that 'blinks" in and out uniformly. The precise tolerances achievable with this visual method are not quantified but in practice it can be used to achieve combining efficiencies as high as the camera alignment; it can also be done mid-experiment without switching the beams to ASE and without attenuating heavily for the camera. This principle of near-field fringes can be used to generate an error signal for angular alignment that can be algorithmically optimized, as will be discussed later.

3.2.6 Beam Size and Beam Collimation Errors

The efficiency loss due to beam size mismatch can be written in terms of the ratio of the beam waist sizes, assuming well collimated beams and the beamsplitter at the beam waist [78, 97]. The analysis follows the procedure outlined in the preceding sections.

$$\eta = 1 - \frac{\left[\sqrt{2}\left(\frac{w_{01}}{w_{02}} - 1\right)\right]^2}{4} \tag{3.19}$$

Using the $\eta = 99.5\%$ criterion the tolerance on beam size is $0.9 < \frac{w_{01}}{w_{02}} < 1.10$ or a variance of $\pm 10\%$. Beam size is set by the MFD of the fiber and the focal length f of the lens used for collimation, in the approximate form $\mathrm{w}_0 \approx \frac{2\lambda}{\pi(\mathrm{MFD})} \times f$. The use of experimental fiber with $\sim$10% variation of MFD along the draw length, meaning some efficiency loss may occur.

Calculation of the efficiency loss due to mismatched beam collimation involves more mathematical work than the others as the assumption of the beamsplitter at the beam waist is no longer valid, requiring maintaining many terms dependent on z in the evaluation of the integral over x

and y. The result, however, is quite simple and just depends on the Rayleigh range z_R and the mismatch between the waist locations Δz [78].

$$\eta = 1 - \frac{\left(\frac{\Delta z}{\sqrt{2} z_R}\right)^2}{4} \tag{3.20}$$

For the $\eta = 99.5\%$ tolerance Δz can vary by $\pm 20\%$ of the Rayleigh range; for a $2\mathrm{w}_0 = 1.8\,\mathrm{mm}$ beam at $\lambda_0 = 1035\,\mathrm{nm}$ this is $\pm 50\,\mathrm{cm}$.

Collimation alignment is currently done by using the beam profiling camera to track the beam, setting the waist to be equidistant from each collimator. The differential distance between the combining elements is about 50 cm, on the edge of the tolerance and likely requiring larger beams in the future. Additionally, low-NA cladding light from the fiber can distort the near-field beam shape and interfere with the beam size measurement, lowering collimation accuracy. More accurate techniques include shear plates, which require narrow-band signals, or wavefront sensors, which are very expensive.

3.2.7 Beam Power Mismatches

The efficiency loss due to beam power mismatches can be analyzed by following a similar procedure using different field amplitudes $E_{1,2} = \sqrt{P_{1,2}}$ and once again placing the beam waists at the beamsplitter.

$$\eta = 1 - \frac{\left(\frac{P_1}{P_2} - 1\right)^2}{4} \tag{3.21}$$

Using the same $\eta = 99.5\%$ efficiency calculation the tolerance is $0.85 < \frac{P_1}{P_2} < 1.15$, or a variation of 15%. Beam power mismatches can come from many sources, but in practice matching seed and nonlinear phase profiles of all the amplifiers will keep the power well within the 15% tolerance. Other sources of loss, such as imperfect HR mirrors, are small and will not noticeably affect combining efficiency.

3.3 Automatic Control of Temporal and Spatial Parameters

Constant, active control of critical parameters such as temporal phase is required to offset environmental drift. Automated control uses a *control signal* (in this case, channel phase) either to minimize an *error signal* or to optimize a *metric signal*. Generation of the error or metric signal and the algorithmic method of minimization or optimization are separate domains; in some control systems generation of the appropriate error or metric signal can form most of the challenge. This section will briefly introduce the common methods of actively controlling spatial phase and then show how the chosen method, stochastic parallel gradient descent (SPGD), is implemented. Additional methods for controlling group delay and spatial drifts will be presented along with their integration into the current control structure.

3.3.1 Active Locking of Temporal Phase

The three types of control typically used for phase stabilization in coherent combining are: (1) Hansch-Couillard [99], (2) locking of optical coherence via single-detector electronic-frequency tagging (LOCSET) [100], and (3) stochastic parallel gradient descent (SPGD) [101].

Hansch-Couillard is used in polarization combining [90] where, when the differential channel phase is locked, the output polarization is stable. The error signal proportional to the phase difference is generated through a balanced detector where the optimum input state is 45° polarization. Locking the error signal to zero can be done with a simple, dither-free algorithm such as PID, at the cost of requiring detection after each combination element, complicating scaling to high numbers of channels.

LOCSET uses a single error detection metric at the output of the system but *tags* each amplifier with a different sinusodial dither such that the output signal can be frequency-domain post-processed to generate error signals for each amplifier. The phase error for each channel can be minimized by locking the error signal to zero with any applicable algorithm. While this has the simplicity of single-detector phase locking, the dither frequencies must be significantly slower

than the rep-rate of the laser and, for high-channel count systems, become densely spaced in the frequency domain, complicating stabilization.

Gradient-descent algorithms are the last class typically used. The metric signal is generated by calculating the derivative (in 1D case) or gradient (in multidimensional case) and traveling along it until the metric signal is optimized. Using randomly distributed dithers the gradient can be numerically approximated in parallel, making the algorithm converge over time [101, 102]. Like LOCSET this only uses one detector at the output of the system but, unlike LOCSET, no sinusoidal dither frequencies must be applied, making this approach appropriate for large CBC array scaling. For its simplicity and scalability we chose SPGD as the optimization algorithm for CBC. Here a description of the algorithm will be given, along with some common modifications to improve performance. While in CBC the algorithm is technically used as a gradient-*ascent*, the convention of calling it gradient-descent will be used.

3.3.1.1 Two-Channel Gradient Descent

The simplest example of gradient descent is illustrated in a two-channel system in the format of the Mach-Zehnder interferometer shown in Fig. 3.3. For this analysis the move to discrete time will be made, where the superscript m will denote each full iteration of the algorithm. The output of the combiner is focused onto a photodiode that creates a voltage $V(\phi_e^{(m)} + \phi_c^{(m)})$ dependent on the environmental phase $\phi_e^{(m)}$ and control phase applied by the phase-shifter $\phi_c^{(m)}$. Applying a small perturbation $\delta\phi$ to the phase shifter and measuring the associated change in voltage δV is used to approximate the gradient $\nabla V^{(m)} \approx \delta V^{(m)} \delta\phi^{(m)}$. It is assumed that the environmental phase does not change over the time it takes to calculate the change in voltage δV. Given that the gradient points in the direction of maximum increase, travelling along or opposite to it can maximize or minimize the signal respectively. Thus the next step $(m+1)$ of the algorithm applies a new phase $\phi_c^{(m+1)} = \phi_c^{(m)} + g\left(\delta V^{(m)} \delta\phi^{(m)}\right)$ where g is known as the "gain" term and determines how many times the gradient the algorithm should travel. The parameter $\delta\phi$ is known as the perturbation depth and needs to be high enough to create a gradient term above the noise but low enough to not add

significant dither on the signal. In practice both g and $\delta\phi$ are determined experimentally. The time it takes for the algorithm to measure the voltage change and calculate the new set-point is known as the *algorithm speed*, and the time it takes to converge to the maximum is known as the *convergence time*. The convergence time is anywhere from 10-100x slower than the algorithm speed, depending on the choice of the gain and perturbation depth. Proper performance of the algorithm requires that the time-varying environmental phase $\phi_e(t)$ is constant across the derivative measurement and does not vary faster than the convergence time of the algorithm. For a pulsed laser system the maximum algorithm frequency is constrained to $f_{\text{algorithm}} = \frac{1}{2} \times f_{\text{laser}}$ because each algorithm loop requires two measurements of combined intensity. Thus for a 2 kHz laser the maximum algorithm speed is 1 kHz with maximum convergence times around 10 ms, which is usually fast enough to maintain control over environmental drifts.

3.3.1.2 Extension of Gradient Descent to N Amplifiers

For extension to N control parameters ($N + 1$ amplifiers) naively estimating the gradient would require evaluating N partial derivatives $\frac{\delta V}{\delta \phi_i}$ for $i = 1, ..., N$ to generate $\nabla \overline{V}$, slowing the algorithm by N times. However it can be shown that if the dither steps $\delta\phi_i$ are statistically independent variables with zero mean and equal variance then the dithers can be applied simultaneously and the gradient can be approximated by the change in the overall merit function $\delta V = V(\overline{\phi_e} + \overline{\phi_c} + \overline{\delta\phi}) - V(\overline{\phi_e} + \overline{\phi_c})$ times the vector of dithers $\overline{\delta\phi} = [\delta\phi_1, ..., \delta\phi_N]$ in the fashion $\delta V \overline{\delta\phi}$ [101, 102], where the superscript (m) is left off for clarity. This is known as stochastic parallel gradient descent (SPGD), where the stochastic refers to the random distribution of the dithers and the parallel refers to the fact the gradient is calculated all at once. In practice this is implemented by using a constant value $\delta\phi$ as the perturbation depth across all dithers and randomly generating the dither direction such that $\overline{\delta\phi}^{(m)} = \overline{p}^{(m)} \delta\phi$ where $\overline{p}^{(m)}$ is a vector containing -1 or 1, randomly distributed. This parallel implementation maintains the algorithm speed scaling with laser rep-rate mentioned above, but as parameter count increases the convergence time decreases, requiring algorithm modifications and possibly higher laser rep-rate. A example of the SPGD algorithm is given in Eqn. 3.22.

$$
\begin{aligned}
\text{measure} \qquad & V(\overline{\phi_e}^{(m)} + \overline{\phi_c}^{(m)}) \\
\text{perturb phases} \qquad & \overline{\delta\phi}^{(m)} \\
\text{measure} \qquad & V(\overline{\phi_e}^{(m)} + \overline{\phi_c}^{(m)} + \overline{\delta\phi}^{(m)}) \\
\text{calculate approx. gradient} \qquad & \delta V^{(m)} \overline{\delta\phi}^{(m)} \\
\text{set new phase set-point} \qquad & \overline{\phi_c}^{(m+1)} = \overline{\phi_c}^{(m)} + g\left(\delta V^{(m)} \overline{\delta\phi}^{(m)}\right)
\end{aligned}
\tag{3.22}
$$

3.3.1.3 SPGD Modifications for Lower Noise and Faster Convergence

One issue with SPGD arises when the signal is at a maximum or minimum—the measured gradient will always be non-zero due to the derivative approximation using finite step sizes. This can be corrected by using a two-point dither that tests both sides of the current set-point, yielding a gradient of zero when the the signal is at a maxima or minima. The modification to the change in measured voltage $(\delta V)^{(m)}$ at algorithm step m can be written as:

$$
\delta V^{(m)} = V(\phi_c^{(m)} + \phi_e^{(m)} + \bar{\delta\phi}) - V(\phi_c^{(m)} + \phi_e^{(m)} - \bar{\delta\phi}) \tag{3.23}
$$

with simple extension to the gradient as described above.

A second modification is called momentum and can be used to speed convergence or ignore local maxima; it is called momentum because it can be analogized to the effect a massive particle moving in a conservative vector field (where normal SPGD is a massless particle) [103]. This momentum includes some memory of how fast the convergence was moving and in what direction; in practice this is done by adding a history term β to the phase update step.

$$
\overline{\Delta\phi}^{(m+1)} = \overline{\Delta\phi}^{(m)} + \beta\overline{\phi}^{(m-1)} + g\left(\delta V^{(m)} \overline{\delta\phi}^{(m)}\right) \tag{3.24}
$$

This history value $\beta < 1$ will weight a step $m - q$ behind the current step by β^q. The value of β for the step q back to add less than 1% to the current movement can be written as $\beta = \sqrt[q]{0.01}$;

for $q = 5$ this requires $\beta = 0.4$ and for $q = 45$ this requires $\beta = 0.9$. In early iterations of the algorithm, before the history has a chance to build up, the effect of momentum usually needs to be suppressed, usually by waiting a number of algorithm steps before applying the extra term to the update step.

3.3.2 Spectral Filtering for Automated Group Delay Alignment

In principle the output energy, measured as a voltage V after a integration on a photodiode, can be used as a merit function for the group delay alignment as well as the temporal phase. However this would require a secondary SPGD loop with dithers consisting of 2π jumps of each channel phase, significantly complicating the system. Instead, the spectral fringes created by a group-delay mismatch Δt (Eqn. 3.6) can be used to generate a secondary merit function utilizing the phase dithers [104]. Detection of the spectral fringe is done by shifting the carrier frequency of the detected light, usually by spectral filtering, such that a signal is generated that is only optimized when $\Delta t = 0$. This is shown in Fig. 3.5 where the carrier (blue) is locked and a red-shifted spectral component is used to generate a secondary error signal. In this example the carrier is also shown filtered; in practice locking the phase across the whole spectrum locks the phase at the carrier. The group-delay detection sensitivity can be increased by stronger spectral filtering at the cost of reducing the maximum misalignment that can be corrected. The spectral separation between the

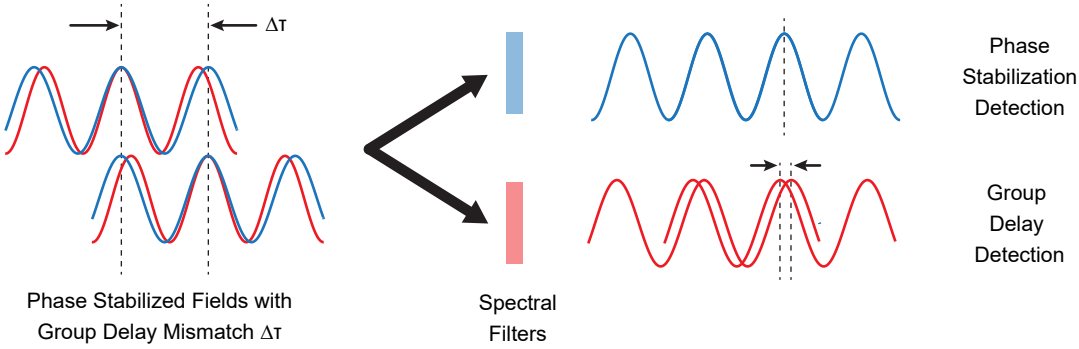

Figure 3.5 : Principles of detection of group delay mismatches, shown for two representative frequencies in an ultrashort pulse. Blue is the carrier and red is a spectrally-shifted signal.

main detector and the filtered detector must be kept within a full spectral fringe to unambiguously optimize to the global maximum. For a rectangular spectrum with width $\Delta\omega$ the largest spectral filtering is $\omega_0 + \frac{\Delta\omega}{2}$. Solving Eqn. 3.6 to put the first spectral fringe minima at this point results in a combining efficiency of 50%, far lower than would ever be seen even with rough initial alignment; in practice then any filtering will remain within a full spectral fringe.

The SPGD phase stabilization dithers can be used to calculate the group-delay gradient by multiplying the vector of the phase dithers $\bar{\delta\phi}^{(m)}$ by the change in the group-delay detector $\delta V_{\text{GD}}^{(m)}$. Treating this as a "slow-loop" that accumulates the group-delay gradient over large number of phase stabilization loops reduces noise, ensures the gradient is calculated while the phase is properly stabilized, and isolates any channel cross talk. The accumulated error signal over M phase stabilization loops is written as $\mathcal{E} = \frac{1}{M}\sum_{i=m}^{m+M} \delta V_{\text{GD}}^{(i)} \times \bar{\delta\phi}^{(i)}$. Zeroing this error signal will require making 2π jumps to channel phase and letting the phase stabilization settle before further optimization. Practical implementation of the 2π jumps will lead to phase stabilization drop-outs and thus cannot be done while temporal combining stabilization is running. Current experimental evidence suggests that the amplifier path length drift is small and fully compensated by the phase shifters after a thermalization time on the order of 1 h, meaning group-delay optimization would only need to be run once at the start of the experiment.

Fig. 3.6 shows how the group delay stabilization would be incorporated into the SPGD phase stabilization loop. The number of phase loops between each group delay jump is shown as 100 in this example but will have to be determined experimentally.

3.3.3 Spatial Filtering for Automatic Angular Alignment

A similar method of error signal generation to group delay involves filtering in the spatial domain, where angular and overlap misalignments cause spatially varying fringes that can be isolated and optimized [105]. Diffraction changes the spatial wavefronts depending on the distance from the beam waist and thus changes the character of the interference fringes, as shown in Fig. 3.7 for an offset x_0 and a angular displacement θ. Notably there are locations where the displacement and

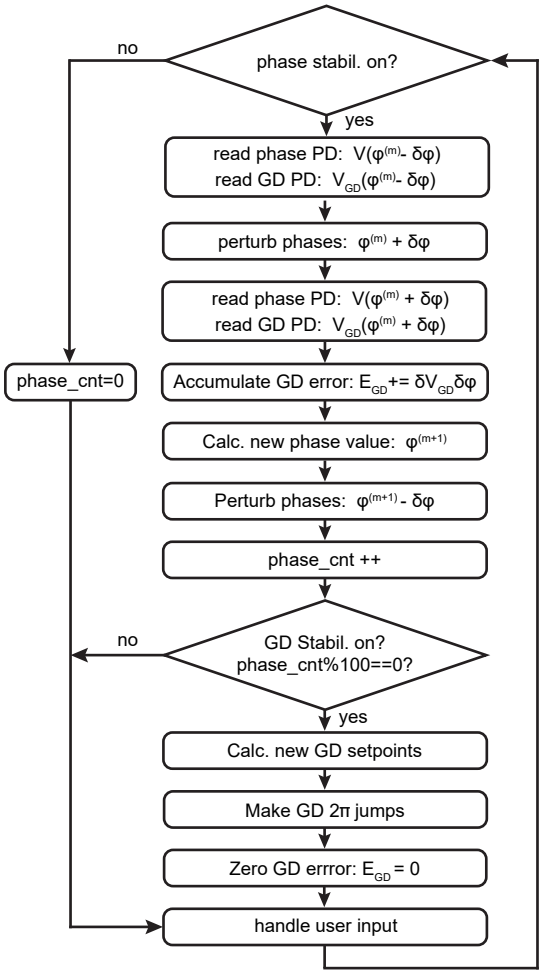

Figure 3.6 : Algorithm flow chart for the group delay (notated GD) optimization incorporated with two-point dither SPGD phase stabilization. The function "handle user input" reads input data from the USB communication to turn phase and group delay stabilization on and off.

angular errors are isolated: (1) at the beam waist (near-field) where the fringes appear only for angular misalignment θ, and (2) several Rayleigh ranges away (far-field) where the fringes appear only for a displacement x_0. Thus the same method of filtering can be applied in near and far field and can generate isolated error signals, using the same phase SPGD dithers as in group-delay alignment. Filtering can be done with a single beam incident on a quadrant photodiode, where processing is done to isolate half the beam in the x-direction and half the beam in the y-direction [106]. The changes to the algorithm are trivial and mimic the group delay algorithm steps in Fig. 3.6. Through this method dither-less control of beam position and angle is available that,

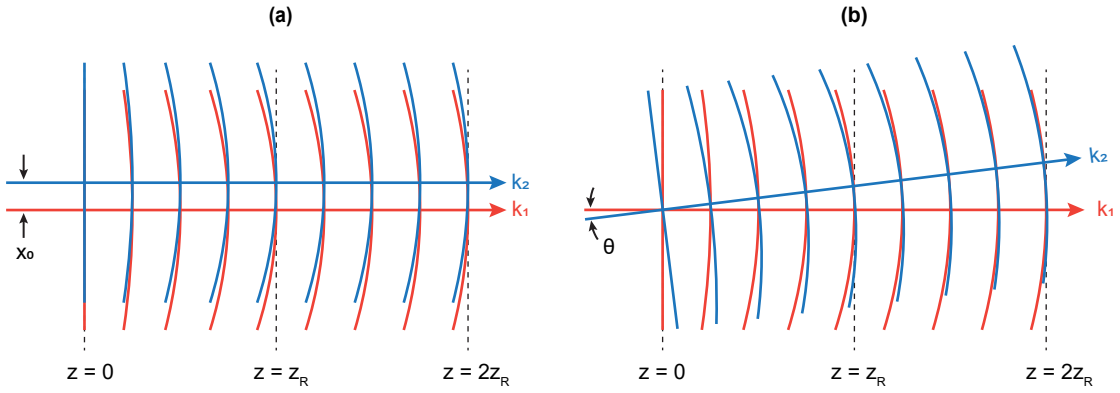

Figure 3.7 : Phase fronts of two co-propagating Gaussian beams showing fringes for: (a) position (near-field) misalignment x_o, and (b) angular (far-field) misalignment θ.

because it does not require any large phase jumps, can be done while stacking is running. Ongoing work involves implementing this method for angular misalignment first, as the tolerances are more restrictive than for beam displacement alignment.

3.3.4 Experimental Characterization of Piezo Response Speed

Proper control of the CBC array requires that the phase shifters applying the changes calculated by the algorithm rise quickly, respond linearly to the applied voltage, and maintain a consistent value. The phase shifters used in this work are piezo mirrors used in double pass and, because of electrical and mechanical limitations they must be experimentally tested to ensure proper operation. In this section two piezo mirrors are tested, a commercial mount (Thorlabs Polaris K1S3P) and a homemade mount consisting of a piezo chip (Thorlabs PA4GKW) glued to a blank on one side (for mounting) and to a small $\phi 1/2$" mirror on the other side.

Several considerations are: (a) the rise time of the piezo, (b) the settling time of the piezos after they rise, (c) any phase shift between the control loop and the piezo and (d) hysteresis. A step response applied to the piezo excites all the resonances of the mechanical structure, leading to oscillations in position. For this reason the frequency of the lowest resonance is often cited as

the bandwidth limit of the piezo, as ramping the voltage at a rate slower than that frequency will not excite the resonance. If the mechanical structure does not have any large resonant frequencies then the rise time of the piezo when a step response is applied will form the speed limit. This is determined by how fast the piezo, which can be modeled as just a capacitor, takes to charge to its final voltage based on the driver current.

The change in piezo voltage vs. time is called the slew rate and can be limited by either the driver electronics or the piezo capacitance. The max slew rate given a driver current I_{driver} and a piezo capacitance C_{piezo} can be written $\frac{dV}{dt} = \frac{I_{\text{driver}}}{C_{\text{piezo}}}$. This can be related to the phase slew rate by considering the maximum piezo stroke L_{max}, the maximum piezo voltage V_{max} and the center wavelength λ.

$$\frac{d\phi}{dt} = \frac{4\pi L_{\text{max}}}{\lambda} \times \frac{I_{\text{driver}}}{C_{\text{piezo}} V_{\text{max}}} \tag{3.25}$$

In practice electronics can easily provide slew rates exceeding the piezo maximum of $1\,\text{V} \cdot \mu\text{s}^{-1}$ (for a 100 mA driver current). For stable phase control the piezo must fully achieve its final value before the next step of the algorithm; at a maximum pulse rate of 10 kHz this leaves 100 µs for the piezo to rise. Equation 3.25 can be rearranged to solve for dt for a given phase change.

$$dt = \frac{\lambda}{4\pi L_{\text{max}}} \times \frac{C_{\text{piezo}} V_{\text{max}}}{I_{\text{driver}}} \times \frac{1}{d\phi} \tag{3.26}$$

An algorithm step will be no larger than a quarter wave (and often much smaller); using the capacitance of the Polaris piezo the rise time is 1.58 µs and for the PA4GKW chip it is 15.7 µs for a $\lambda/4$ at 1035 nm, both fast enough for the required 10 kHz control speed.

Measurement of the resonances can be done with a scanning Michelson interferometer where one arm contains the piezo mirror driven by a function generator and high-voltage amplifier. The output of the interferometer is focused onto a photodiode, viewed on an oscilloscope and used to measure the relative response of the piezo for increasing sinusoidal driving frequencies. To maintain linear operation of the interferometer the amplitude of the driving frequency is kept small and the voltage offset is used to keep the interferometer at the quadrature point. The same setup is

used to test the step response by applying a square wave to the piezo and viewing the rise time and ring-down.

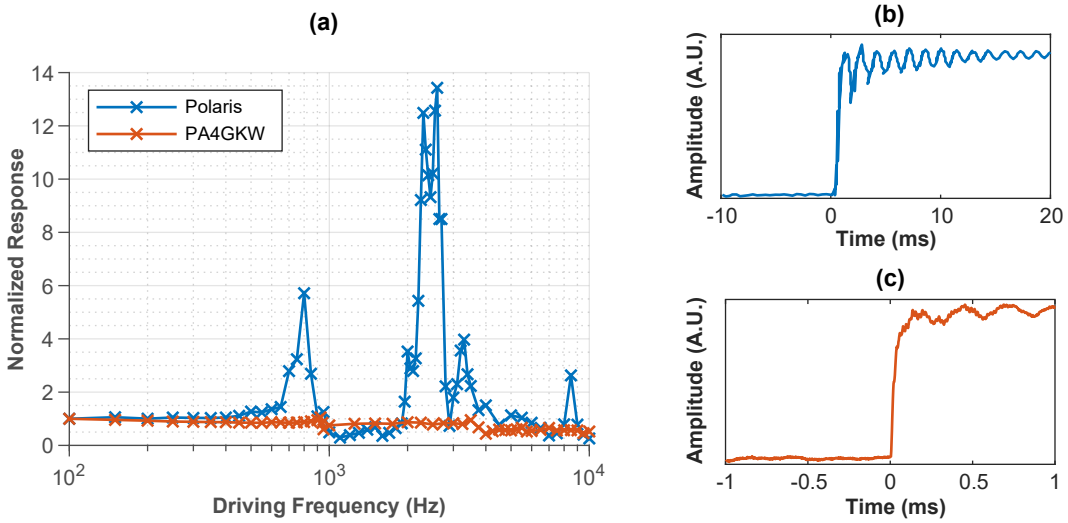

Figure 3.8 : Experimental results of the piezo testing: (a) normalized frequency response, (b) step response for Polaris mount, and (c) step response for the homemade mount. The rise time in (c) is 30 µs, close to the calculated value.

The results of these tests, shown in Fig. 3.8, indicate strong resonances for the Polaris piezo mount and relatively small resonances for the homemade mount. The resonance at 700Hz of the Polaris mount is very clearly seen in the step response which, once it is excited, requires 20 ms to settle. In contrast the homemade mount has a very small resonance at 3 kHz, which causes only small oscillations after the mount has risen. In this case then the true limit of the homemade mount is higher than the small 3 kHz resonance, while the limit of the Polaris mount is the 700 Hz that is strongly excited for any step response impulse. Experimentally large improvements in coherent combining stability were seen when using the homemade mount; for this reason (and the 4x lower cost) this is the preferred phase shifter for our work. The downside is the 5x smaller movement range than the Polaris piezos, which increases likelihood of phase drifts running out of piezo range. As will be shown in the next section, after the amplifiers have come to thermal equilibrium this is not an issue.

The final issue to address is piezo hysteresis, the property that the absolute position depends not just on the voltage applied but the direction it was approached from. When using a model-free

control loop like SPGD the hysteresis appears as a deviation for the optimal calculated algorithm point, mimicking phase noise, and will be automatically corrected for on subsequent iterations.

3.4 4-Channel CBC and 81-Pulse CPSA Experiment

The experimental results of the integrated CBC and CPSA systems are described here for an array of 4 parallel amplifier channels with the same 81→1 pulse stacking design as in Chap. 2. The experiments achieve up to 25 mJ spatially combined with temporal combining efficiency of 70%, matching the low energy results and demonstrating initial CBC scaling. This design is suitable, with small modifications, for up to 12 parallel channels on the 5ft wide table and as such provides the experimental basis for a 100 mJ system and beyond.

3.4.1 Experimental System

The experimental design remains much the same as the overall CPSA system as shown in Fig. 2.16, with the exception that the final CCC amplifier is replaced by an array of four amplifiers as shown in Fig. 3.9. The signal is increased through the pre-amplifiers such that each channel is seeded with 250 μJ; in future experiments with higher channel count another pre-amplifier and AOM will be added. The seed signal is split in sequential PBS and HWP pairs which are incorporated with double-pass delay lines consisting of a translation stage for group-delay alignment and a piezo mirror for phase control. After amplification the beams are collimated with a f=75 mm lens to a beam diameter of $2w_0$ = 1.8 mm which travels through the combining R = T = 50% intensity beamsplitters organized such that sequential splitting of seed at the amplifier input is compensated by the sequential combination of the beams at the output. The beams in the combiner reject ports are expanded and then blocked with beam dumps. After combination the beam is expanded by 2x to 3.6 mm diameter, a 4% reflection is used for diagnostics while the main beam is either measured with an average power meter or sent into the GTI stackers.

To stabilize the energy in the combined port a small fraction of the output signal is integrated

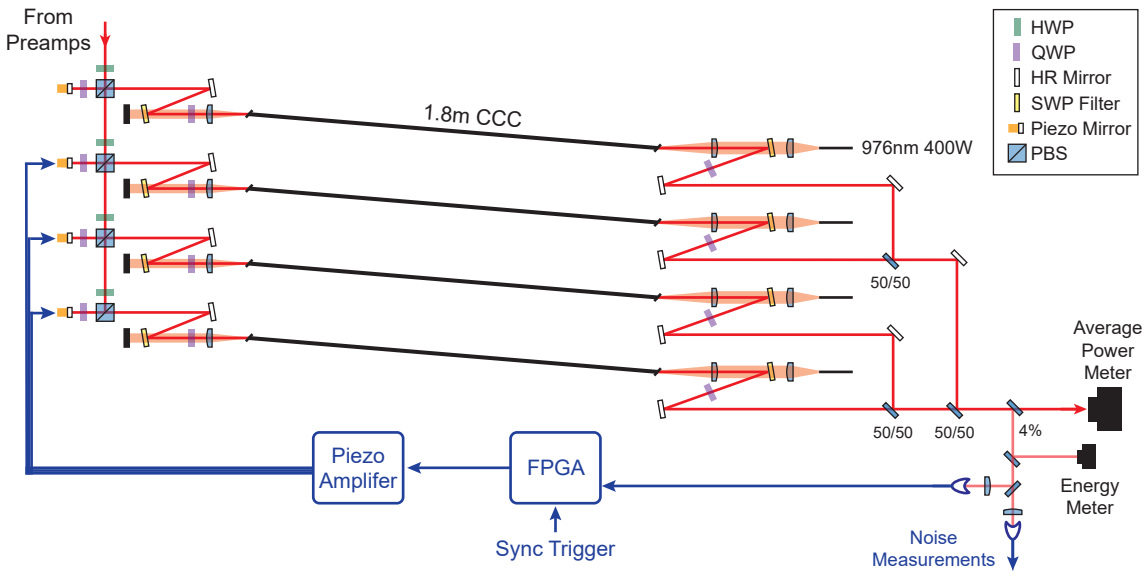

Figure 3.9 : Coherent beam combination addition to the overall CPSA system. The output is either measured with an average power meter (for efficiency measurements) or sent to the stackers to be temporally combined.

on a slow photodiode (Thorlabs DET10A) and read after the burst has passed by a triggered ADC (PMOD AD2). The control system is based on a internally clocked FPGA (CMOD A7) that reads the ADCs, writes the phase to piezos with DACs and runs the stabilization algorithm, which is written in C and compiled to the chip. Jitter between the master FPGA, which is clocked off the oscillator, and the CBC FPGA, which is internally clocked, is less than 10 ns, shorter than the integration time of the photodiode. The use of a secondary FPGA (as opposed to running the algorithm on the master FPGA) allows for on-chip algorithmic control of phase and additionally does not use 1GHz ADC and DAC resources when slower 10 MHz electronics suffice.

3.4.2 Coherent Beam Combining Results

Measurement of CBC stability and efficiency is done after the appropriate beam overlap and pointing alignment tolerances are achieved as described in Sec. 3.2. The rep-rate is 2 kHz, matching the single-channel experiments. For each tested output energy set-point successive amplifiers are pumped (with the others blocked) until they achieve the desired equal-nonlinearity burst, as measured with a 22 GHz photodiode and 50 GHz oscilloscope. Then group-delay optimization is done,

after which the detectors are appropriately attenuated and all the amplifier paths are unblocked, leading to uncontrolled interference. The SPGD loop is engaged, locking channel phases and maximizing interference.

Avg. Ch. Energy	Comb. Eff.	Comb. Energy	Comb. Power	NRMSE
1 mJ	94%	3.8 mJ	7.4 W	0.84%
3 mJ	96%	11.4 mJ	22.3 W	0.81%
5 mJ	95%	19.0 mJ	37.0 W	0.94%
7 mJ	89%	24.9 mJ	48.7 W	1.41%

Table 3.1 : Results from the 4-channel CBC experiment at 2 kHz including total output energy and power.

Efficiency is measured with both a pyroelectric energy meter (Ophir PE10-C) and a thermal average power meter (Newport 818P-300-55), in the locations shown in Fig. 3.9. This allows dual confirmation of efficiency numbers and, at high power, understanding the effects of CW ASE. Calibration is done to relate the energy/power at the measurement locations to the fiber output. The efficiency is then calculated as the power/energy after the last combining element divided by the sum of the outputs of all the amplifiers. The results of increasing energy on combining efficiency are shown in Table 3.1, where high-efficiency spatial combining is maintained up to 7 mJ per channel. The maximum combined energy of 25 mJ represents the largest per-channel energy spatially combined, exceeding the 3.3 mJ / fiber in the 12-amplifier, 8-pulse EDPA experiment [54]. Above 7 mJ / ch non-common deviations from the designed equal-nonlinearity phase profile across amplifiers reduce spatial combining efficiency. The combined noise increases significantly as well, likely due to the presence of multiple local combined energy maxima in the phase landscape that exist when the amplified pulse profiles do not share nonlinear phase profiles. These experiments above 7 mJ / ch are not yet suitable for simultaneous temporal and spatial combining and are left out of these investigations.

Output amplitude stability is measured by splitting a portion of the optical signal used for the FPGA stabilization and measuring it with a secondary slow photodiode (Thorlabs DET10A). The beam is focused onto the diode to remove any effects of spatial noise, and the signal is read on a triggered, computer connected ADC (National Instruments NI-9215) connected to Labview. This

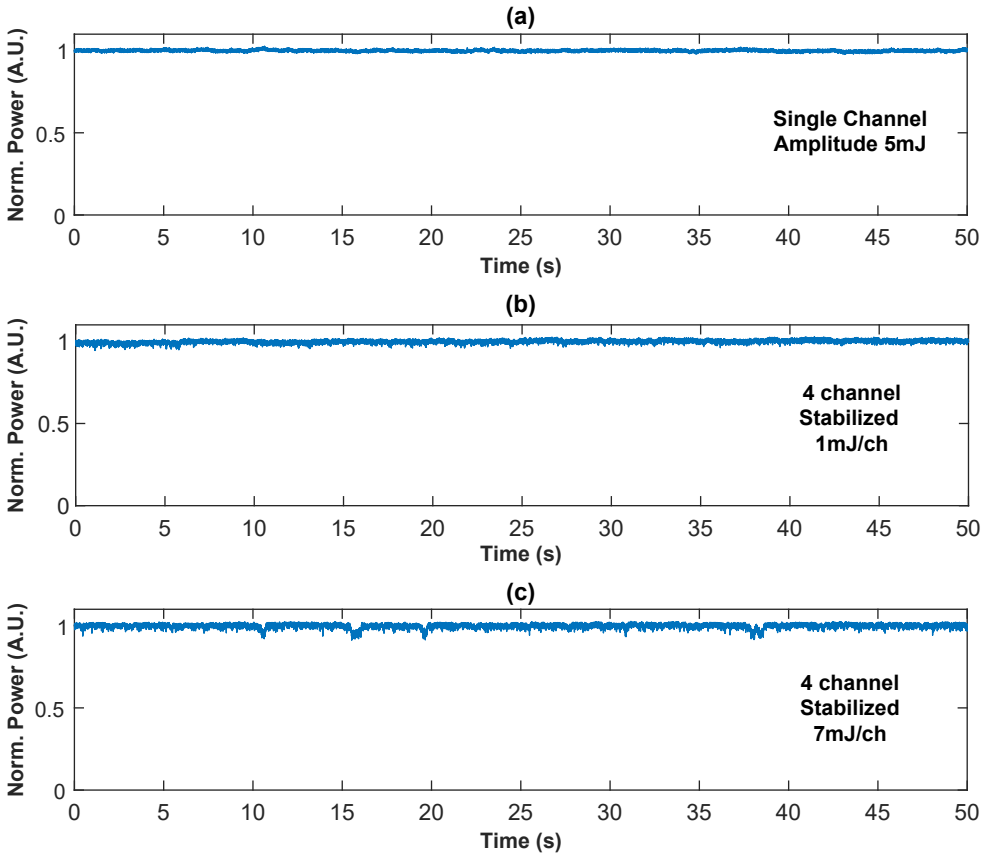

Figure 3.10 : Measured output amplitude of the CBC system: (a) single channel amplitude noise reference, (b) stabilized 4 ch. 1 mJ/ch, and (c) stabilized 4 ch. 7 mJ/ch.

allows for real-time viewing of combined noise statistics as well as saving the measured amplitude of every combined pulse. Examples of stabilized traces are given in Fig. 3.10, comparing the amplitude noise from an amplifier channel 5 mJ to the the stabilized noise for 1 mJ/ch and 7 mJ/ch set-points. Qualitatively the stabilized output noise is higher than the single-channel amplptude limit, with additional small stabilization drop-outs in the 7 mJ/ ch traces. This is likely due to increased phase drift from thermally-induced changes in path length at high pump power that exceed the convergence time of the algorithm. Scaling of pulse rep-rate will increase algorithm speed and convergence time at the cost of adding more heat from higher pumping; proper stabilization at 10 kHz (100 W) will likely require improved amplifier cooling as well.

The output amplitude noise of the spatial combining directly impacts stabilization of the GTI stackers. Quantitative characterization is often done through calculating the normalized RMS er-

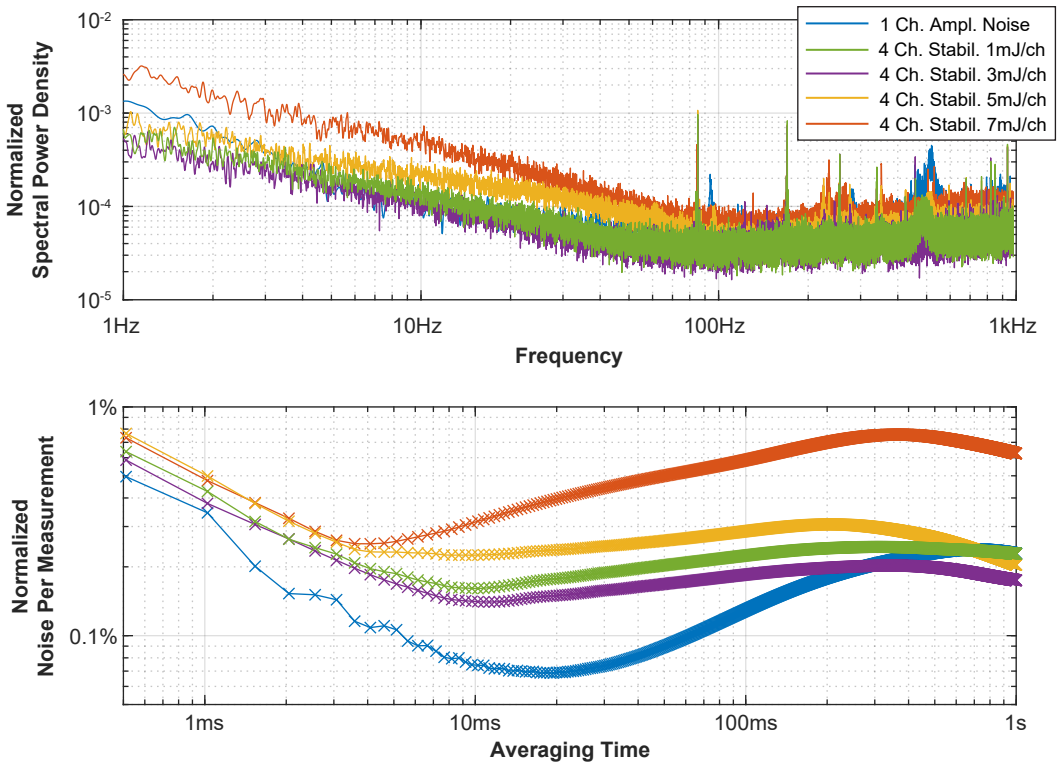

Figure 3.11 : Noise statistics for the output of CBC system: *top* spectral power density calculated using an FFT, *bottom* time-domain noise per measurement calculated with the Allan deviation.

ror (NRMSE) in the fashion NRMSE $= \frac{1}{\bar{x}}\sqrt{\frac{1}{N}\sum_{i=1}^{N}(x_i - \bar{x})^2}$ where the average value of the data set is $\bar{x}$. This metric is best suited to errors with random distribution around a mean, like white noise, and does not differentiate fast noise from slow drifts in the data set. Viewing the spectral or temporal characteristics of the noise provides more accurate diagnostic information; spectral characteristics are viewed through a Fourier transform while temporal information is viewed through the Allan variance [107]. The Allan variance, originally designed for calculating clock drift, calculates the RMS variance of successive differences for different averaging times, which directly relates to the noise seen by stabilization algorithms; additionally the local slope of the data indicates the dominant noise content.

The Fourier transform and the Allan variance are shown in Fig. 3.11. The roughly flat spectral content above 100 Hz coupled with $-1/2$ slope from 500 µs to 10 ms in the Allan variance shows the white noise region. The increase in noise between 10 ms / 100 Hz and 500 ms / 2 Hz is due to

the stabilization algorithm attempting to compensate the phase drift. The increase in noise at the 7 mJ set-point, showing that on the 10 ms to 1 s time scale the stabilization is more noisy than the white-noise limit, indicates incomplete stabilization, corroborating the traces seen in Fig. 3.10.

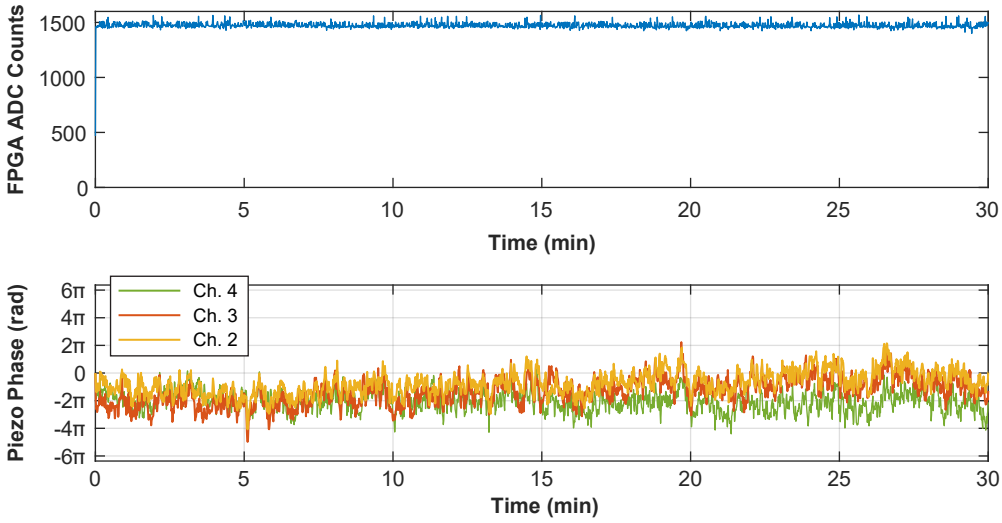

Figure 3.12 : Output data from the CBC FPGA showing stabilization for 30 min at 5 mJ/ch set-point. The vertical scale in the bottom plot is scaled to the maximum phase shifting range.

During stabilization the voltage applied to the piezo phase shifters can be used to estimate the absolute phase being applied to each channel, giving insight to the magnitude of the phase drift slower than the algorithm convergence time. This voltage data can only be queried from the FPGA at 1.2 Hz as the algorithm must pause to communicate data over USB UART, a downside of on-chip stabilization, and limiting insights to slow drift only. An example is given in Fig. 3.12 where the stabilization runs for 30 min at 5 mJ/ch, showing that the compensated drift does not exceed the piezo phase shifter range over this period. This data was taken after the system had thermalized for about 1 h; for stabilization while the system is coming to a stable temperature drifts frequently exceed the range of the phase shifters.

3.4.3 Coherent Temporal Combining Results

Temporal combining alignment follows the general procedure as described in 2.7.1 and efficiency is measured at each spatial combining set-point. The results are summarized in Table 3.2, with an example input burst and stacked trace at 5 mJ/ch given in Fig. 3.13. Temporal combining efficiency remains very similar to the single channel results, indicating no degradation induced by beam combining.

Per Channel Energy	Stacking Efficiency	Stacked NRMSE
1 mJ	77%	0.94%
3 mJ	74%	0.87%
5 mJ	70%	0.99%
7 mJ	70%	2.0%

Table 3.2 : Results of the combined CBC and stacking experiment for different energy levels. Some variance is expected due to daily variations in alignment.

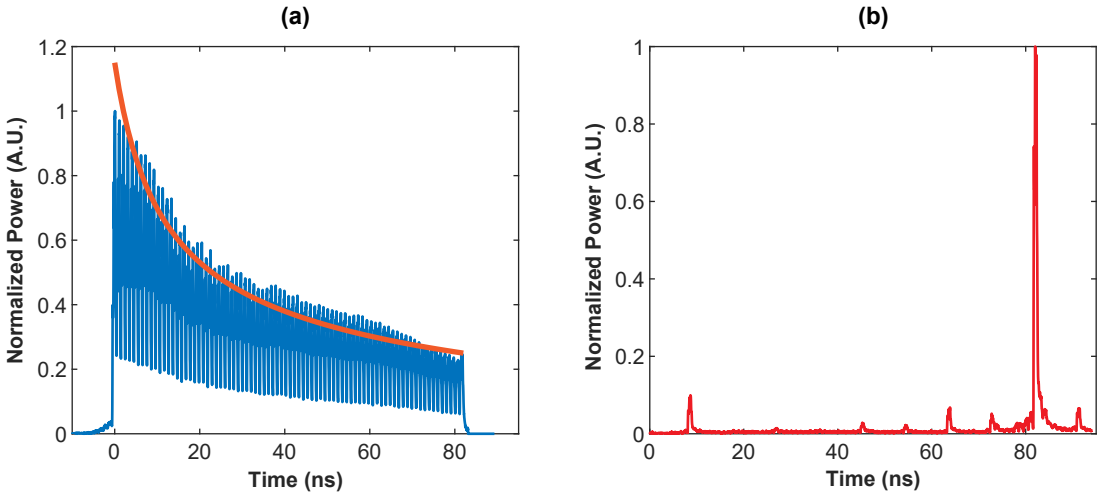

Figure 3.13 : Experimental results for the 5 mJ per channel CBC and CPSA experiment: (a) spatially combined burst containing 19 mJ of energy, shown with the appropriate equal-nonlinear burst shape, and (b) the stacked pulse trace with 70% of the total energy in the 81st pulse

.

The noise for temporal combining is measured by tracking the peak power of the stacked (81st) pulse measured in each loop of the SPGD algorithm stabilizing the stackers. This SPGD loop runs around 100 Hz and is asynchronous due to Ethernet communication with the FPGA board.

Frequency or time domain noise processing cannot be done with asynchronous data, limiting numerical insights to just the NRMSE. The temporal combining NRMSE remains close to the CBC NRMSE until 7 mJ / ch set-point, where it increases from 1.4% from the CBC output to 2.0% from the temporal combining output. This is not unexpected, as the frequency and time domain analysis from the CBC output (Fig. 3.11) shows a significant increase in drift noise in the 10 ms to 1 s region which, as this is within the convergence time of the stacking algorithm, will adversely impact the stacking stabilization. This high stabilization noise will also impact the measured stacking efficiency, which is averaged over several seconds using a 50 GHz sampling oscilloscope.

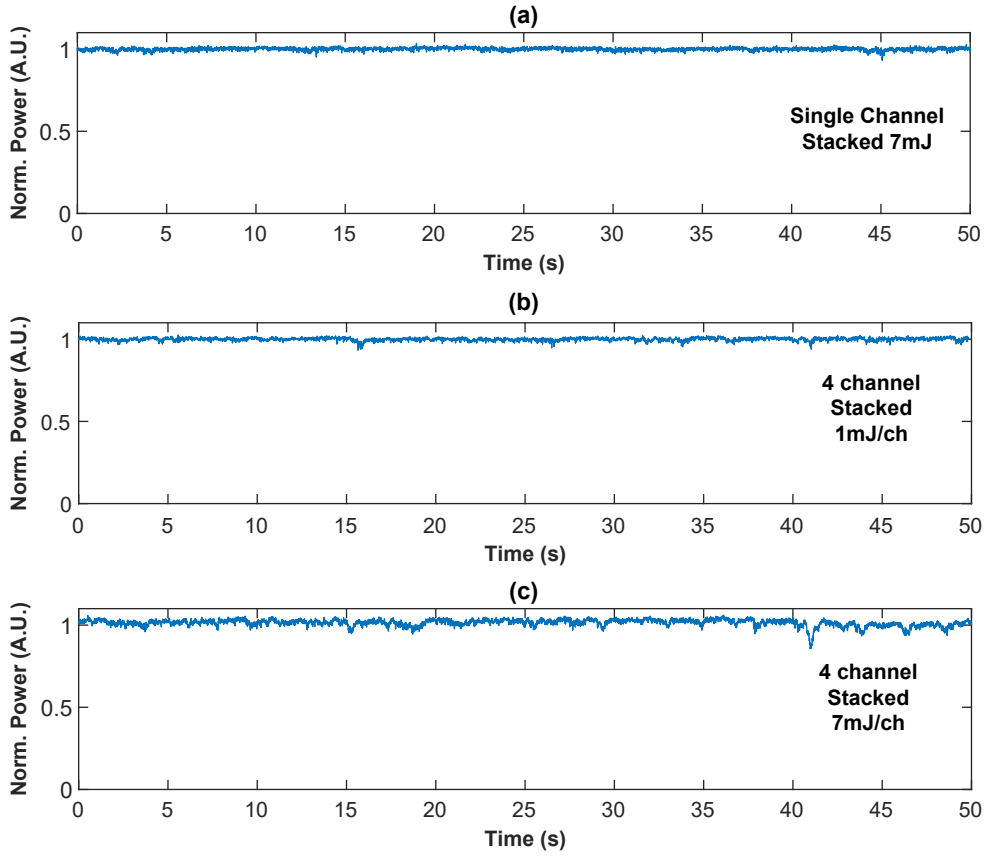

Figure 3.14 : Stabilization results of stacking experiment over 50 s: (a) single-channel stacked at 7 mJ, (b) 4 Ch. stacked at 1 mJ/ch, and (c) 4 Ch. stacked at 7 mJ/ch.

Femtosecond pulses are maintained under simultaneous spatial and temporal combining. Fig. 3.15 shows the autocorrelation trace of the combined output for the 5 mJ / ch experiment. The increase in pulse duration is attributed to re-alignment of the stretcher that was not fully compen-

sated in the compressor, as well as to required oscillator maintenance that changed the spectrum slightly. This is not an aspect of the spatial combining and will be corrected in the future.

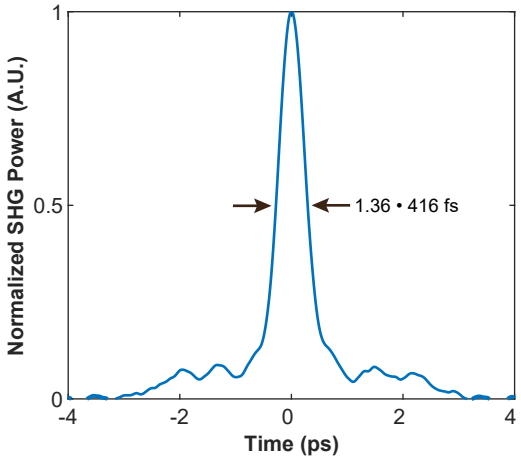

Figure 3.15 : Autocorrelation trace for the simultaneous four-channel CBC and CPSA experiment at 5 mJ / ch.

3.5 Ongoing and Future Work

These results validate simultaneous spatial and temporal combining, showing high efficiency spatial combining to 25 mJ with subsequent temporal combining efficiency matching the single-channel results. The decrease in temporal stabilization quality with increasing spatial stabilization noise gives the tolerable amplitude noise for future spatial combining iterations at higher fiber energy or larger channel count.

The improvements of single-channel stacking discussed in the previous chapter, namely control of the spectral reshaping and increasing the pulse burst length, will have a direct impact on both the spatial and temporal combining quality. Any reduction in overall nonlinear phase will reduce the differential phase accrual in improperly matched amplifiers, increasing the spatial combining efficiency and allowing for operation up to the full stored energy limit of 10 mJ. These improvements will of course also improve pulse compression as well.

An increase in output amplitude stability is essential for further energy and power scaling,

especially since as channel numbers are increased the algorithmic convergence time decreases. Better cooling of the amplifier fibers will reduce the magnitude of the phase noise and will be essential for any power scaling. Increasing algorithm speed by scaling repetition rate only yields increased stability if the higher required pumping does not induce an increase in phase noise—this requires further investigation and will be critical to average power scaling of this system. Work is ongoing with collaborators at Berkeley National Laboratory to apply machine-learning stabilization techniques to spatial combining by generating unique channel information through measuring the amplitude after each beamsplitter. This may allow for much faster algorithmic convergence times even at the current 1 kHz loop speed.

This chapter has shown record scaling of fiber array energy, and with these improvements CBC combined with CPSA will be able to provide up to 100 mJ from 12 amplifiers, leading the way to a future 10 J-class system with only 10^3 parallel channels, a major reduction from the array size required for single-pulse CPA or 8-pulse EDPA.

CHAPTER 4

Generation of Fast Neutrons and Novel Backlighting Technique for Viewing Laser-Plasma Dynamics

The preceding chapters have shown exciting scaling of fiber laser energy to record high per-channel energy levels, an important step in array scaling of ultrashort, high energy, high average power lasers. This chapter presents the first plasma physics experiments from this laser, using the CBC and CPSA system to generate fast neutrons in D_2O, a first from an all-fiber system. Additionally, construction of a novel target backlight providing arbitrary delay, ultrashort, off-band light gives unique imaging capability for this and future experiments. The work shown in this chapter represents critical first steps in the path of CPSA fiber lasers in application to plasma physics.

All plasma experiments are done in collaboration with Nicholas Peskosky. More details about specific applications, target fabrication, and calibration of detectors and confidence of measurements can be found in his thesis [108].

4.1 Neutron Generation in Free-Flowing Liquid Jets Using a High Rep-Rate Fiber Laser

4.1.1 Motivation

Neutrons were first generated from a laser in 1968 [109], and in the 65 years since the yield has increased to more than $10^{12}\,\mathrm{n}\cdot\mathrm{shot}^{-1}$ using 100 kJ facilities like NIF [110]. Unlike conventional

radionucliotide or accelerator tube generated neutrons, laser-driven sources have small emitting area and short pulse duration [111], making them especially applicable to nuclear medicine [112] and imaging [113]. As such, much work has gone into optimizing neutron yield from laser-matter interactions with the goal of creating reliable, bright, high-flux tabletop neutron sources. Femtosecond lasers show the highest yield for a given pulse energy, with an approximate scaling for a pulse energy of E_p given as $Y = 4.1 \times 10^5 \times E_p^{1.65}$ [114], shown in Fig. 4.1 (red-diamonds and red dashed line). The absolute highest yields are generated by long-pulse lasers with massive pulse energy; however, for practical generation of high neutron flux ($\mathrm{n \cdot s^{-1}}$) rep-rate scaling of ultrashort lasers is the most promising approach. The modest yield of $10^4\,\mathrm{n \cdot shot^{-1}}$ from a 100 mJ, 10 kHz femtosecond laser could produce a flux of $10^8\,\mathrm{n \cdot s^{-1}}$, on par with that created in a single shot of a 10 J ultrashort or 600 J nanosecond laser facility.

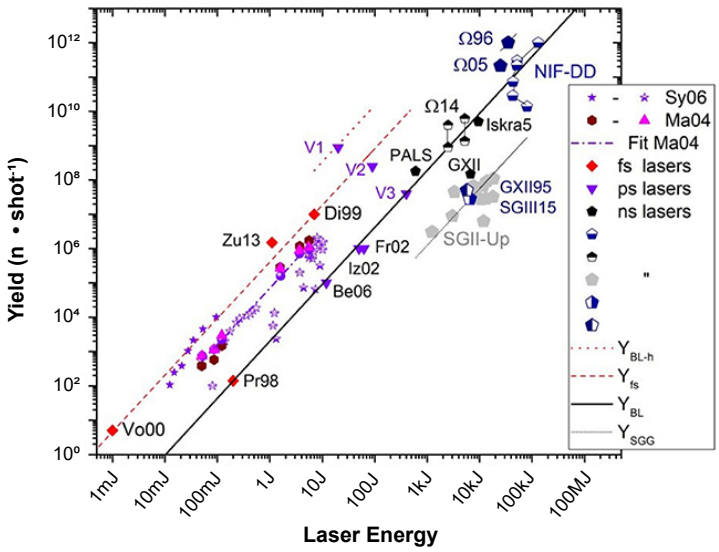

Figure 4.1 : Neutron yield vs. laser energy. The red diamonds and red dashed line show general scaling for femtosecond laser systems. Reprinted from [114]

Scaling rep-rate introduces targetry problems, as most current experiments are designed for low rep-rate or single-shot lasers [115] (for example, the single-use capsules used in exploder-pusher experiments at NIF). The generation mechanism most amenable to high rep-rate targets is laser induced binary fusion of two lighter nuclei, which liberates an energetic neutron in the process, typically done using the $\mathrm{D+D} \rightarrow {}^3\mathrm{He+n(2.45\,MeV)}$ reaction, in which two deuterons fuse to form

helium and yield a characteristic fast neutron [114]. The deuterium-tritium reaction can also be used [116] but, due to inherent radioactivity and proliferation risk, is not done outside properly equipped and permitted laboratories. High rep-rate targets for D-D reactions include deuterated liquids in free-flowing streams [117], sheet targets [118], or synchronized micro-droplets [108].

In this chapter we use the spatio-temporally combined CBC and CPSA laser system for the first, to our knowledge, demonstration of fast neutron generation with an all-fiber laser, building on the work with liquid microjet targets designed for the 480 Hz lambda-cubed (λ^3) laser[1]. We both validate the CPSA demonstration system and investigate the rep-rate scaling of liquid-jet targets to the multi-kHz region, a necessary step in laser and target technology for future tabletop neutron sources.

4.1.2 Experimental Design and Results

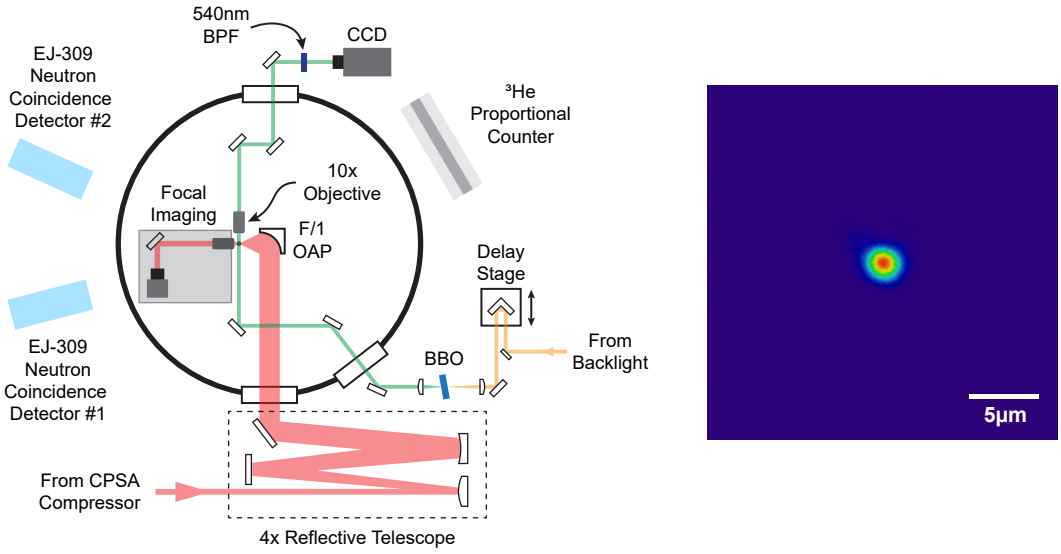

Figure 4.2 : Experimental design for neutron generation and measured focal spot. The focal imaging setup (grey shaded box) consists of a 50x objective and CCD camera which is only used at attenuated power levels and is removed when the experiment is run.

Variable on-target pulse energies are generated by running the CBC system at a consistent 11 mJ, 2 kHz output (3 mJ per channel, 90% effic.) and attenuating the fraction sent to temporal

[1] 18 mJ, 35 fs, 480 Hz cryogenic Ti:Sa centered at 800 nm, also at the University of Michigan

combining with a HWP and TFP combination. Due to daily time constraints inherent in coupling multiple experimental systems, stacking alignment was done quickly, achieving 70% temporal combining efficiency and a 500 fs compressed pulse FWHM. After compression the 6 mm diameter beam is sent to the experiment, shown in Fig. 4.2, where it is expanded to 2.5 cm in a reflective off-axis telescope utilizing spherical mirrors. The beam enters the vacuum chamber through an un-coated window and is focused to a $2w_0 = 4.4\,\mu m$ spot using a F/1 50.8 mm diameter dielectric-coated 90° off-axis parabola (OAP) (Edmund Optics 15-379). Focal imaging is done for a highly attenuated beam using a 50x microscope objective and a CCD camera. The near diffraction-limited beams of the CCC fiber amplifiers combined with the interferometry in CBC and CPSA means a clean, Gaussian focal spot is achieved with no need for adaptive optics. When running the experiment the energy on target is varied between 2 and 4 mJ, leading to a estimated maximum focal spot intensity of $7.2{\times}10^{16}\,W \cdot cm^{-2}$ and an estimated peak power of 5.5 GW. The transmission of the overall system is low due to overfilling one telescope mirror and use of a un-coated window, both of which will be improved in future experiments. Imaging of the target is done with an ultrafast off-band backlight, as described in the next section.

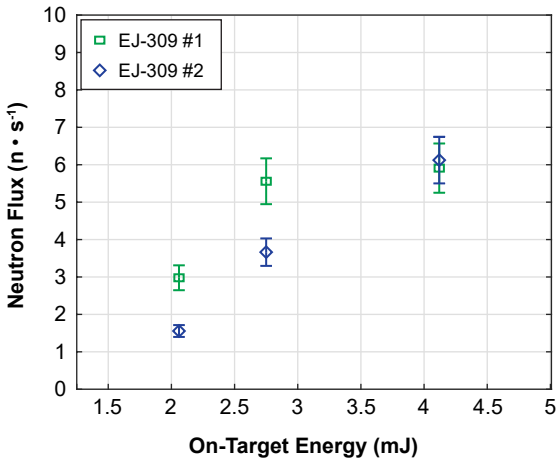

Figure 4.3 : Total neutron flux calculated from EJ-309 detectors vs. on-target pulse energy. Figure courtesy of Nicholas Peskosky.

This target in this work is a free-flowing 15 µm-diameter jet of D_2O flowing at a rate of $240\,\mu L \cdot min^{-1}$. Given scaling data from [114] the expected yields are low, on the order of $10\,n \cdot s^{-1}$,

requiring careful detection to isolate D-D generated neutrons from the cosmogenic neutron background [119]. This is done with two fast-neutron induced proton-recoil detectors (Eljan EJ-309) mounted $\sim$ 11 cm from the focal spot and gated with a photodiode to capture events within 512 ns of the drive pulse arrival. No high-Z shielding was used in order to maximize capture of any produced neutrons, leading to significant γ and x-ray counts; however, the detector remained below the paralyzation level. Use of pulse shape discrimination cuts [120], binning pulse shape parameter (PSP) values of 0.25-0.5 as fast neutron events, isolates detected γ-rays from detected neutrons, as shown in Fig. 4.4. Additionally, a moderated ^{3}He detector and Geiger-Muller counter were used to align the target.

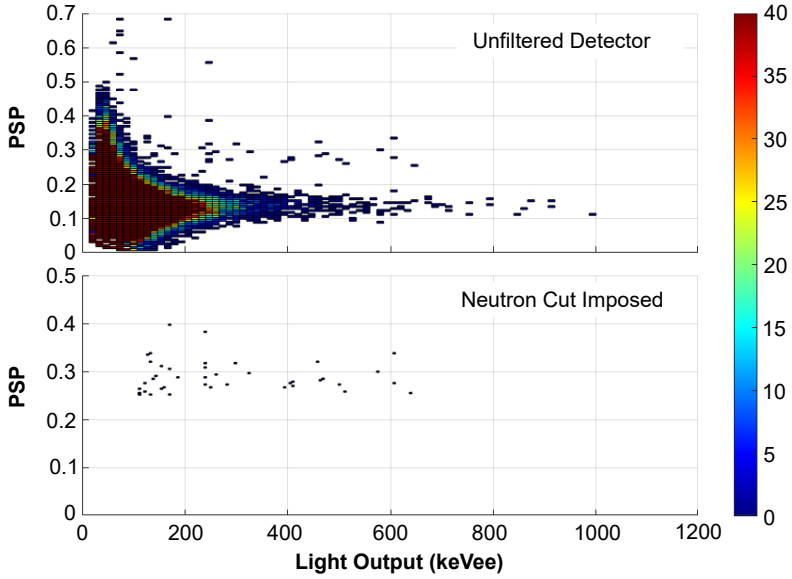

Figure 4.4 : Gated fast neutron counts for EJ-309 #1 detector, shown before (top) and after (bottom) PSP cuts are imposed to isolate neutron events. The results for detector #2 are similar and omitted for brevity. Figure courtesy of Nicholas Peskosky.

At the highest laser energy, coincident neutron events measured over 1725 s in the PSP region of interest register 43 and 31 counts for the #1 and #2 detectors, respectively. Calibration of the background laboratory neutron flux predicts (at worst-case) only 0.0775 background events in the measurement window, giving high confidence that the measured neutron flux is generated from the laser-matter interaction.

4.1.3 Ongoing and Future Work

Improving these results falls into two categories: (1) increasing the peak focal spot irradiance, and (2) improving the targetry to fully optimize yield. The laser has not yet been run at its highest power and fully optimized state; the long pulse duration of 500 fs was due to residual third-order phase resulting from adjustments to the oscillator and stretcher that were not fully compensated in the compressor, and pulse duration has since been returned to near-bandwidth limit of 330 fs. The low-transmission of the telescope is more of a concern and likely is due to imperfect collimation in from the CBC system into the stackers. Proper collimation adjustment will increase stacking efficiency and improve power throughput, increasing peak power towards 40 GW with $5{\times}10^{17}$ W $\cdot$ cm^{-2} focal plane intensities, enough to see significant neutron yield and measure time-of-flight and other diagnostics.

Heating the target to the level where thermonuclear fusion is initiated and neutrons are generated becomes easier as targets shrink. The 15 µm-diameter jet used in this work is quite large compared to targets used in similar work [108], and yields can likely be increased by reducing target size by using micro-vapors created by piezo or surface-acoustic wave devices. Recent work on λ^3 has shown that orbital angular momentum beams at grazing incidence on the same liquid jet target enhance neutron yield by several orders of magnitude [108]; generation of these Hermite-Gauss beams require spiral phase plates matched to the laser wavelength. The phase plate used in the λ^3 experiments is manufactured for 800 nm and would exhibit unacceptable error if used at 1035 nm; we are investigating purchase of an appropriate one for the CPSA laser. With these improvements we expect to see neutron counts above 10^3 n $\cdot$ s^{-1} from the system in the near future.

4.2 Ultrashort, Off-Band, Arbitrary Delay Target Backlighter for Use With CPSA Fiber Laser Drivers

4.2.1 Introduction and Motivation

Ultrashort laser matter interaction experiments present unique imaging difficulties due to micron-scale target sizes, femtosecond dynamics, microsecond ranges of interest and image contrast degradation from plasma self-emission. Imaging schemes generally use a synchronized probe beam to illuminate the target at times before, during and after the driver pulse and seek to identify pre-plasma generation, target dynamics and density profile evolution using techniques from simple shadowgraphy to shearing interferometers [121]. Time-resolved, high spatial resolution experimental data is necessary for both alignment and diagnostics but also for comparing to simulations. One important example is imaging the laser pre-pulse effects on the target, which are experimentally variable and can have large effects on the laser-plasma interaction, to accurately calibrate simulation initial conditions [122].

For experimental campaigns on cutting-edge, low rep-rate lasers data sets are limited by shot number, complicating statistical measurements and requiring complicated schemes to image each target interaction at multiple time steps to get adequate diagnostics [123, 124]. Scaling of drive laser rep-rate opens a regime where statistics and images from large sets of shots can be used to understand and optimize laser and target parameters [125], and to do so at high quality requires a backlighting probe pulse matched to the final laser rep-rate that can produce high-contrast images at all time scales of interest.

A large challenge in diagnostic imaging arises from the varying time scales over which the plasma, and target, evolve. The electron population in the target follows the drive laser pulse, on the order of 10s-100s of femtoseconds, while the ion population can evolve for many nanoseconds after the driver has passed. In high rep-rate systems, ensuring the target has re-formed and reached an equilibrium before the next pulse arrives can require imaging out 10 µs or longer, depending on

the target and the laser rep-rate [115]. Thus the probe for short time-scales must have ultrashort duration matching the drive laser (30-300 fs) and must have delay ability up to 10 µs or longer.

The fastest camera shutter times are 1 ns, meaning that plasma images are taken stroboscopically with an "open" shutter (relative to the femtosecond laser time scale) in a style reminiscent of the famous bullet-through-apple photograph [126]. When imaging the laser-matter interaction, plasma self-emission and driver fundamental scatter will be integrated over the shutter time and at best wash out any image and at worst cause irreparable damage to the camera. Plasma self-emission can come from multiple sources [127] and is often dominated by the second-harmonic generation, as in the grazing-incidence liquid targets used in the neutron generation experiment. Ideal high-contrast, high-resolution plasma imaging is done with an off-band backlight, fully frequency separated from the driver or plasma self emission, with strong bandpass filtering allowing only the probe light to reach the camera.

Current schemes for generating backlight probe pulses fall into three categories: (1) separate part of the drive laser post-compression and shift it through frequency-doubling or Raman-scattering [128], (2) separately amplify a different pulse from the amplifier, using the edge of the oscillator bandwidth to separate from the fundamental [129] or (3) electronically lock a second, off-band laser system to the drive oscillator [127, 130]. The first scheme benefits from simplicity and timing stability, as any jitter only comes only from mounts and air currents, but is limited by free-space delay stages to the region within several nanoseconds of the drive pulse and the second harmonic frequency is not ideal for reasons discussed above. The second approach can readily generate off-band light by exploiting gain narrowing that leads to a drive pulse narrower in spectrum than the oscillator pulse; with proper control the edge of the oscillator spectrum can be amplified to a moderate power, short pulse outside the driver band. Additionally, by picking the next pulse from the oscillator, large scale delay can be introduced, limited in step size by the base oscillator period and ultimately limited in delay by the stability of the oscillator rep-rate. For most solid-state laser systems the base oscillator is 80 MHz, requiring a mechanical delay stage of $\sim$4 m for sub-oscillator period steps of 12.5 ns. The third scheme, electronically locking a full second laser

system to the first, has the highest complexity and lowest stability but provides great flexibility in off-band frequency content and delay range. With the advent of off-the-shelf Yb-based laser systems generation of off-Ti:Sa harmonic 515 nm light (the second harmonic of 1030 nm) at 100 μJ pulse energies is trivial, and the base oscillator can be electronically synchronized to the drive laser rep-rate. This has been reported to generate 160 fs pulses at 515 nm and used to image cryogenic hydrogen jets with high resolution [127, 130]. However, the overall complexity of this system is high and the driver-backlight pulse jitter is at best 230 fs due to the synchronizing electronics.

Here we present the design of a fiber-integrated, ultrashort, off-band backlight providing arbitrary delay capabilities exceeding 1 ms. Wavelength shifting is done using gain-managed nonlinear amplification (GMNA) in a LMA fiber amplifier, which, when frequency doubled, provides down to 40 fs pulses centered at 545 nm, and deriving the seed from the CPSA 1 GHz oscillator allows for electronic delay in steps of 1 ns, requiring only a small 30 cm delay stage for fine adjustment. Changing electronic delay steps is trivially done by sending one-line commands to the FPGA over Ethernet, allowing for integration with any machine-learning laser or target optimization approaches. This design excels when using the CPSA oscillator but the fundamental design works for any ytterbium laser system, such as Yb:YAG thin disks or DPA, at the cost of introducing longer free-space delay lines to compensate for the lower oscillator rep-rates of 80-100 MHz. Fiber integration makes this system simple, environmentally stable and low-cost, making it an important addition to the diagnostic suite for high rep-rate systems.

4.2.2 Design of Fiber Laser Backlight

Shifting the spectrum off-band is done using GMNA, a recently-discovered effect in co-pumped quasi-three level fiber amplifiers that broadens input pulse bandwidth more than 50x while red-shifting central wavelength and preserving quadratic and cubic spectral phase that can be fully compensated in diffraction grating compressors [131]. This has been used to generate 1 μJ pulses at 40 fs from a 30/400 Yb-doped DCF fiber amplifier [132] with potential for further energy scaling. The full description of GMNA is beyond the scope of this thesis but two nuances are important.

First, while GMNA has been hypothesized as a nonlinear attractor (same output spectrum and pulse shape for a large range of inputs), in reality the input pulses must be close to bandwidth limit and should be in the range of 200-800 fs with a center wavelength near 1035 nm. Second, GMNA amplification requires some level of average power saturation in the amplifier, where the gain does not fully recover between pulses (see Sec. 2.2.4), necessitating MHz-level repetition rates. The backlight initial design uses 5 MHz in the GMNA amplifier to match published work, but investigation is needed to see if lowering rep-rate further preserves broad bandwidth and linear chirp for a possible path to increasing individual pulse energy.

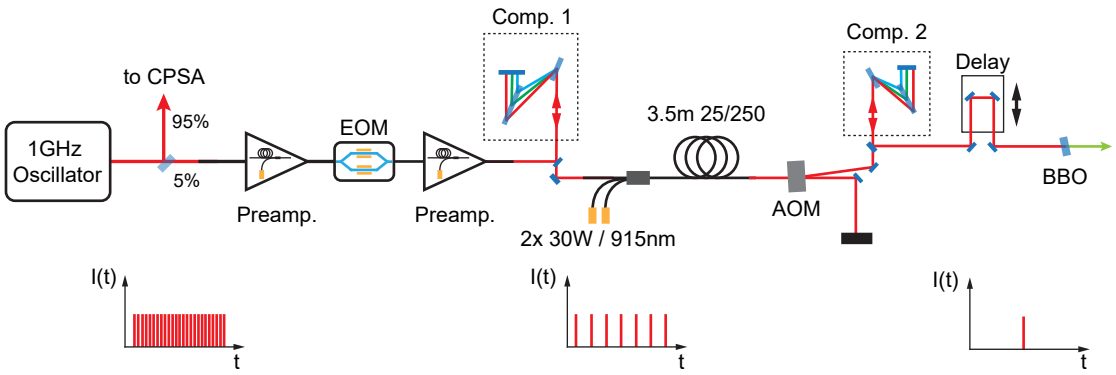

Figure 4.5 : The optical design of the backlighter. The EOM and AOM are fed signals from the FPGA that controls the main system. Compressor 1 can be fiber-integrated using Bragg gratings and circulator, further simplifying the setup.

The full design of the backlight is shown in Fig. 4.5. A small fraction ($\sim$ 5%) of the 1 GHz oscillator output is spectrally filtered with a bandpass filter to 3 nm FWHM centered at 1035 nm before being fiber coupled and delivered to the experimental table. Pulses are then down-counted by a 5 GHz amplitude-EOM to 5 MHz; by changing the pulse picking with this EOM the delay can be varied on steps of 1 ns with no change to the optical path. SMF pre-amplifiers compensate for loss and increase the pulse energy to 200 pJ, after which the delivery fiber dispersion is compensated in a free-space compressor in Treacy configuration using highly-efficient 1000 l·mm^{-1} transmission gratings. The pulses exit the compressor with negative chirp and compress fully over the next 2 m of passive fiber in the pump combiner, entering the GMNA stage at the bandwidth limit. The third order dispersion of the fiber and the compressor add, leading to some features trailing the pulse,

but simulations show that this does not affect GMNA. The GMNA stage consists of a 3.5 m length of 25/250 PM Yb-doped DCF, co-pumped up to 60 W with two fiber-coupled 915 nm diode lasers and, as mentioned above, a pump-combiner is used to eliminate pump alignment and simplify packaging. After amplification the residual pump-through is filtered by a dichroic mirror and then the desired pulse from the 5 MHz train is picked by a quartz-AOM; coarse delay of 200 ns can be done by picking different pulses from the 5 MHz train with this AOM. After the AOM another Treacy compressor using 1000 l·mm^{-1} transmission gratings is traversed, compressing the pulse to 45 fs. The compressed pulse goes through a 30 cm delay line before being focused in 0.5 mm beta-barium borate (BBO) crystal to generate the second-harmonic at 545 nm, necessary to bring the backlight into the sensitivity region of silicon CCD cameras used for plasma imaging. Steering into the chamber is done with protected silver mirrors, and the backlight intensity is increased by focusing it onto the target with a 200 mm focal length lens.

4.2.3 Experimental Results

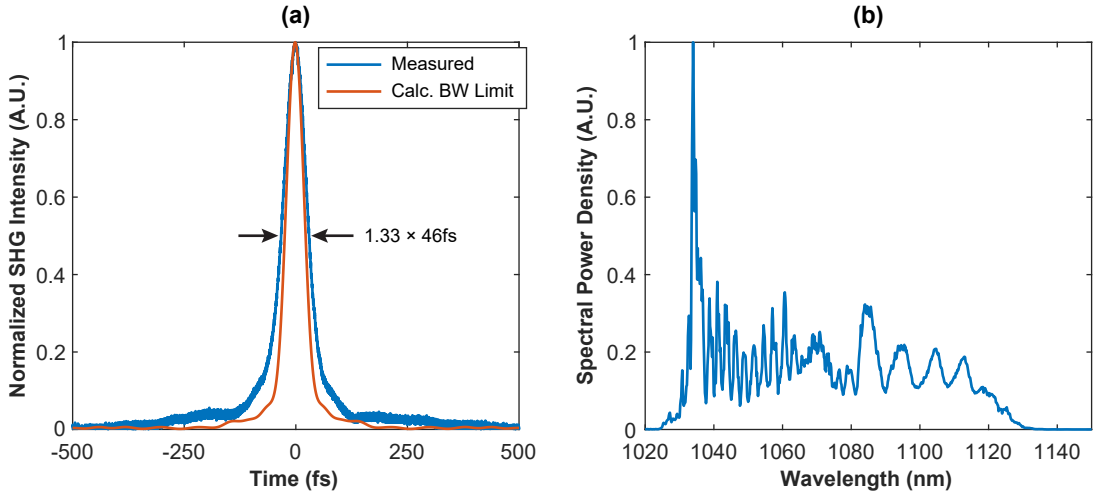

Figure 4.6 : Compressed output of GMNA amplification stage: (a) measured pulse autocorrelation and calculated bandwidth limited autocorrelation, and (b) measured spectrum.

Amplification generates up to 0.6 µJ pulses from the GMNA stage with compressibility to 46 fs. The pulse duration is measured using the same SHG autocorrelator used for the CPSA experiments

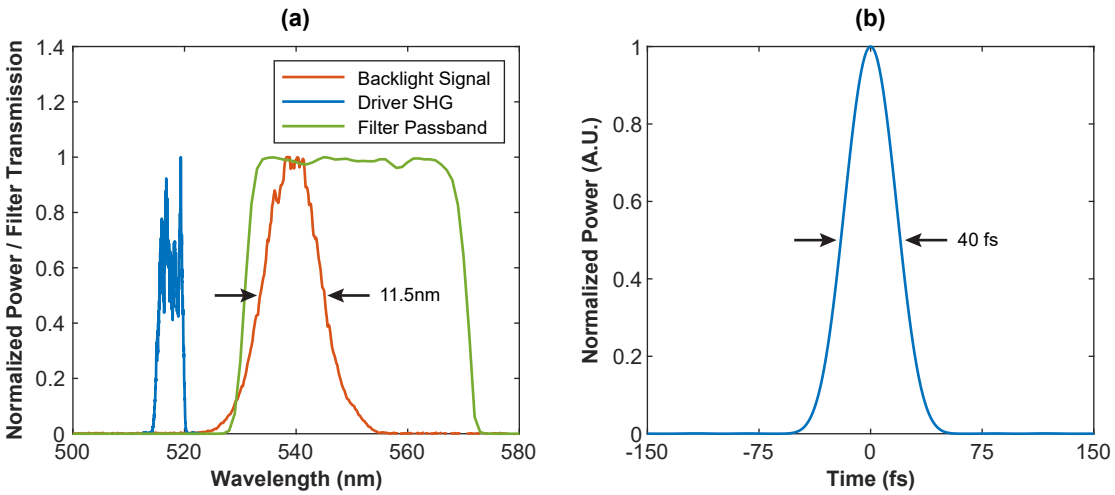

Figure 4.7 : Backlight spectral content: (a) measured second harmonic of the GMNA amplifier overlaid with filter pass-band and calculated second harmonic of the driver, and (b) calculated bandwidth-limited pulse duration.

which is not optimized for pulses this short; the crystal thickness limits the measurable pulse duration to about 40 fs and the delay stage, designed for large scan regions up to 10 ps, is unstable over small scans, creating artifacts seen on the pulse. This measurement provides an estimate of the pulse duration while a shorter-pulse capable autocorrelator is under construction.

We do not have an autocorrelator for green light, so pulse duration must be inferred from the width of the green spectrum; simulations done in SNLO [133] indicate that the 0.5 mm crystal thickness is too long, leading to a slightly longer output pulse than input. Additionally, the use of an achromatic lens after the BBO crystal leads to significant dispersion, spreading the green pulse to an estimated 150 fs. This is done for convenience, and in future iterations a reflective optic will be used for re-collimation. The backlight spectrum and calculated bandwidth-limited pulse duration are shown in Fig. 4.7, showing sufficient shifting off-band. The filter transmission is shown for normal incidence, and with small angle tuning can be adjusted to capture the whole backlight spectral content.

This backlight is used to take images in air of a free-flowing stream of heavy water, in the same setup as shown in Fig. 4.2. The drive laser energy used for this initial proof-of-principle is 1 mJ at 2 kHz, enough to generate a plasma and disrupt the stream but not to create significant radiation.

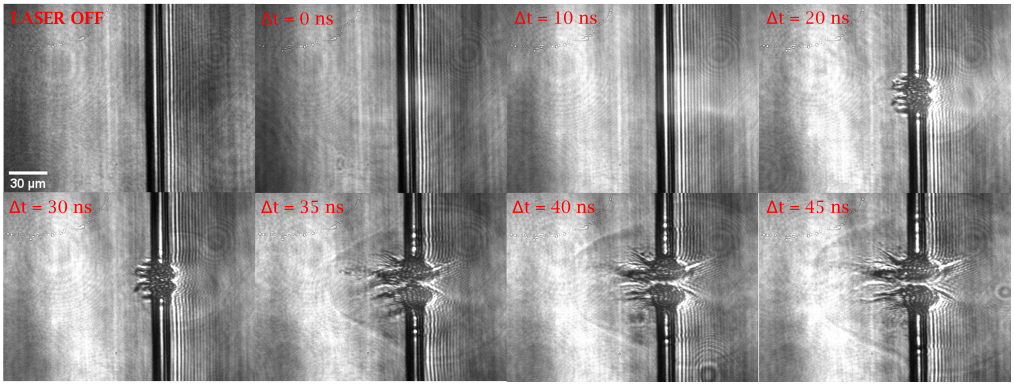

Figure 4.8 : Fine delay images taken by stepping the EOM picked pulse by several nanoseconds, showing the evolution of a shock wave leaving the target.

Imaging is done with a infinity-corrected 10x long-working distance microscope objective (Mitutoyo) and a monochrome 1280x960 CCD (Imaging Source DMK41BU02) with trigger provided from the backlight AOM delay box. Exposure is set to a minimum of 100 µs and electronic gain is set to 36 dB. Plasma self-emission and residual driver is blocked with a 550 nm ± 20 nm bandpass filter (Thorlabs FBH550-40), providing 50 dB of suppression. Primary investigation of the long-time scale dynamics did not require precise calibration of time zero.

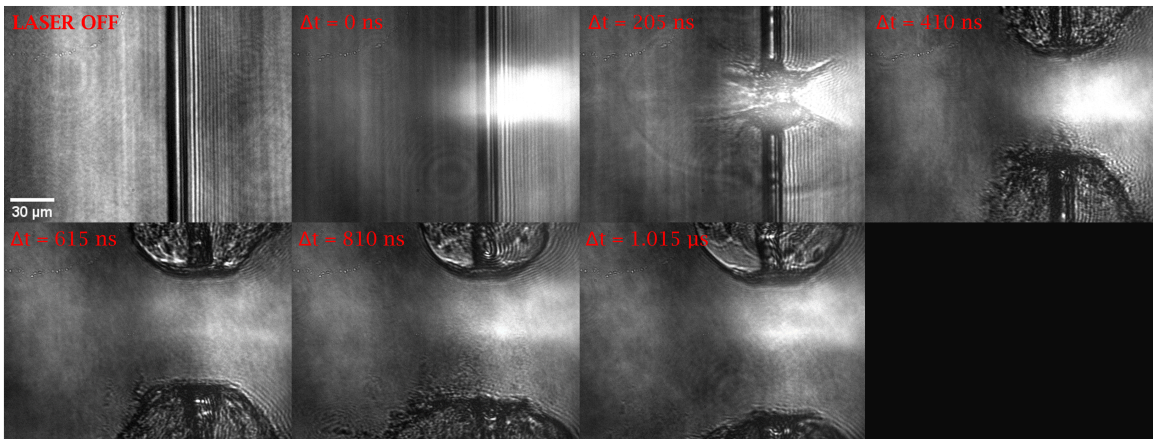

Figure 4.9 : Coarse delay images taken by stepping the AOM window by 200 ns, showing the late time scale evolution of the plasma.

4.2.4 Discussion and Future Work

Fig. 4.8 shows nanosecond scale dynamics evolving after the pulse leaves the target. The shock wave seen in the images reaches a velocity of 2,725 $\pm$ 45 m $\cdot$ s^{-1} at early times before stagnation. This measurement was acquired though stepping the delay with the amplitude EOM in the backlight setup.

Fig. 4.9 shows the later time dynamics of the liquid-laser interaction, generated in 200 ns steps by moving the AOM window to the next pulse. Stagnation of the target stream is likely caused by a thermal pressure wave and and space charge effects that prevents it from re-forming laminar flow until 20 µs post laser interaction (pictures omitted). This indicates the rep-rate ceiling on liquid jet targets to be around 50 kHz, although further investigation is needed to determine if any residual deflected droplets or filaments out of view continue to influence the stream past 20 µs.

Some plasma-self emission is still visible; this will be reduced in proper experiments that are done under vacuum with grazing-incidence targets that preferentially generate driver second-harmonic. Further rejection can be done by utilizing a nanosecond exposure time camera, though these can be prohibitively expensive. Additionally, low pre-pulse contrast has been shown to create pre-plasma and large broadband self-emission in over-dense cryogenic hydrogen targets [127], and it is possible that similar effects are occurring here with the low pre-pulse contrast of the CPSA laser in the over-dense water jet—if true, this will only improve as the CPSA system improves.

Immediate next steps for this experiment include: (1) measuring femtosecond to picosecond dynamics of targets using the manual delay stage, (2) directly measuring the integrated spectral power of the backlight and the plasma emission over the exposure time of the camera to determine self-emission rejection, and (3) measuring the timing jitter of the backlight and drive beam. The first two require using the full CPSA power on the proper target geometry in vacuum. Measuring the integrated spectral power over the camera shutter time will be done by measuring the light that would make it onto the camera with a multi-mode fiber and spectrometer. Through calibration with the known backlight energy the spectral energy density of the self-emission can be calculated, giving a quantitative measure of contrast. Measuring pump-probe jitter must be done with some

type of cross-correlation measurement such as the SHG cross-correlation used for synchronization of pump and probe pulses in OPCPA experiments [134]; other methods exist but require more complicated setups with higher-power drive lasers [130].

For future experiments there are three important improvements: (1) minimization of green pulse duration, (2) monolithic integration of fiber components, and (3) increase of backlight power. The current use of transmissive optics (lenses and widows) after the conversion to green increases pulse duration from an estimated 40 fs to $\sim$150 fs; in the current experiments this does not matter but for imaging fast-time dynamics in the future all lenses will need to be replaced with reflective, off axis mirrors. Additionally, for applications where the backlight pulse duration is very sensitive, doing the conversion to green in the chamber will eliminate any dispersive pulse spreading in the entrance window. To increase system stability and robustness the intermediate compressor can be monolihically integrated using a fiber Bragg grating and circulator. This requires a settled design, as the fiber grating must properly compensate the GDD accrued from pre-amplifier and delivery fibers. The addition of fiber-coupled phase shifters would allow for electronically controlled delay on the femtosecond time scale; using one commercially available 150π phase shifter in double-pass could generate a probe delay of up to 500 fs on demand with 10 fs resolution.

Increasing the backlight energy on target is essential for higher-contrast images at higher driver energies. In the current experiment use of a 1030 nm-optimized isolator after the GMNA stage reduces the pulse energy by almost 50%; an isolator is necessary to prevent backreflections from the plasma entering the amplifier, but a proper broad-bandwidth, high transmission isolator should have transmission of $\sim$90%. Metallic delivery mirrors reduce pulse energy further; replacement with high-reflectivity, low-GDD dielectric mirrors should increase transmission by another 20%. Finally, a proper length BBO crystal will increase conversion efficiency, increasing both the spectral content in the backlight pulse as well as the overall energy. For future energy scaling investigation of different GMNA regimes, specifically at lower rep-rate and higher pumping, could potentially increase output energy up to 10 µJ from this fiber and possibly to 50 µJ from larger-core fibers, bringing the backlight brightness into the regime used for existing hundred-TW laser

experiments.

CHAPTER 5

Conclusion and Outlook

The 38 years since the invention of chirped pulse amplification (CPA) have seen an orders of magnitude increase in focused laser intensities, with high-energy laser pulses used for laboratory astrophysics, acceleration of particles, creation of ultrashort high-brightness x-rays, and more. However, the underlying laser technology providing these high focused intensities cannot scale beyond 1 Hz pulse rates, severely limiting the applications of laser-matter interactions. Next generation laser drivers will require high pulse energy (0.1–10 J) at high repetition rates (10–100 kHz) for practical use. Coherently combined fiber laser arrays are the most promising approach for efficient, high average power systems. For practical array sizes, amplified energy from a single fiber must increased to the storable energy limit of $\sim$10 mJ, requiring use of coherent pulse stacking amplification (CPSA), a time-domain coherent combining technique. CPSA has previously been shown to achieve high efficiency and stability at low powers.

This work demonstrates efficient and stable CPSA at the fiber extractible energy limit, enabling 100x array size reduction, and demonstrates its simultaneous operation with coherent spatial combining of 4 parallel amplifier channels. This work opens a path toward future high-energy, high-power laser systems. Optimization of energy extraction from a saturated fiber amplifier leads to 9.5 mJ extracted in a burst of 81 pulses, and minimization of nonlinear phase accrual in the amplifier allows for this burst to be temporally combined into a 345 fs pulse with 58% efficiency, a record energy in a femtosecond pulse generated by a single-fiber system. Energy scaling through coherent beam combining (CBC) of 4 parallel amplifiers generates up to 25 mJ in an 81-pulse burst

with 90% spatial combining efficiency. Temporal combining of this 25 mJ burst at 70% efficiency represents the most per-fiber energy spatially and temporally combined to date, validating simultaneous CPSA and CBC as a technique enabling practical high-energy and high-power fiber array systems. Investigation of the amplification limits under high saturation suggest lowering nonlinear phase through spectral compensation and modified pulse bursts will improve spatial and temporal combining efficiency, increasing energy per fiber even further. Measurements of coupling of spatial and temporal combination noise shows the limits of stabilization algorithms and establishes amplitude stability criteria. This work demonstrates the first operation of CPSA with coherent spatial combination and directly informs practical future scaling of fiber arrays to the 0.1–10 J energy range.

This system is used for proof-of-principle laser matter interaction experiments using free-flowing liquid jets of deuterated water to show the first ever generation of fast neutrons with a fiber laser driver. These experiments, done at 2 kHz pulse repetition rate, showcase the emerging CPSA laser system capabilities and investigate high repetition rate laser-matter targetry operation, critical for future secondary radiation sources. Images of the laser matter interaction are taken using a novel femtosecond off-band optical probe that provides femtosecond to millisecond arbitrary delay for high resolution, synchronous imaging of late-time target dynamics. This demonstration and developed techniques are a basis for future laser-matter interaction research at repetition rates previously inaccessible by conventional lasers.

Ongoing work in our lab seeks to increase CPSA temporal efficiency to 80-90% at full fiber energy, along with designing fiber that can store even more energy. For applications that require high pre-pulse contrast, novel methods of pulse cleaning that maintain high throughput efficiency and increase contrast by at least 40 dB are being investigated. Similarly, for applications requiring shorter pulse durations, methods of efficient, high energy post-compression are under design and expected to reduce output pulse duration to $\sim$30 fs. Building on the 4-channel CBC system described here, construction has begun of a 12-channel fiber array capable of 100 mJ at up to 1 kW of average power. Future scaling to 10 J of energy with only 10^3 amplifiers is made practical with

the techniques contained in this thesis.

BIBLIOGRAPHY

[1] P. Zhang, S. S. Bulanov, D. Seipt, A. V. Arefiev, and A. G. R. Thomas, "Relativistic plasma physics in supercritical fields," *Physics of Plasmas*, vol. 27, p. 050601, May 2020.

[2] J. Vieira, R. A. Fonseca, and L. O. Silva, "Multidimensional plasma wake excitation in the non-linear blowout regime," *pre-print*, Jul 2020. arXiv:1607.03514 [physics].

[3] A. Gonsalves, K. Nakamura, J. Daniels, C. Benedetti, C. Pieronek, T. de Raadt, S. Steinke, J. Bin, S. Bulanov, J. van Tilborg, C. Geddes, C. Schroeder, C. Tóth, E. Esarey, K. Swanson, L. Fan-Chiang, G. Bagdasarov, N. Bobrova, V. Gasilov, G. Korn, P. Sasorov, and W. Leemans, "Petawatt laser guiding and electron beam acceleration to 8 gev in a laser-heated capillary discharge waveguide," *Physical Review Letters*, vol. 122, p. 084801, Feb 2019.

[4] W. Leemans and E. Esarey, "Laser-driven plasma-wave electron accelerators," *Physics Today*, vol. 62, no. 3, p. 44–49, 2009.

[5] C. Benedetti, S. S. Bulanov, E. Esarey, C. G. R. Geddes, A. J. Gonsalves, A. Huebl, R. Lehe, K. Nakamura, C. B. Schroeder, D. Terzani, J. van Tilborg, M. Turner, J. L. Vay, T. Zhou, F. Albert, J. Bromage, E. M. Campbell, D. H. Froula, J. P. Palastro, J. Zuegel, D. Bruhwiler, N. M. Cook, B. Cros, M. C. Downer, M. Fuchs, B. A. Shadwick, S. J. Gessner, M. J. Hogan, S. M. Hooker, C. Jing, K. Krushelnick, A. G. R. Thomas, W. P. Leemans, A. R. Maier, J. Osterhoff, K. Poder, M. Thevenet, C. Joshi, W. B. Mori, H. M. Milchberg, M. Palmer, J. G. Power, and N. Vafaei-Najafabadi, "Linear colliders based on laser-plasma accelerators," *pre-print*, 2022. arXiv: 2203.08366.

[6] S. Corde, K. Ta Phuoc, G. Lambert, R. Fitour, V. Malka, A. Rousse, A. Beck, and E. Lefebvre, "Femtosecond x rays from laser-plasma accelerators," *Reviews of Modern Physics*, vol. 85, p. 1–48, Jan 2013.

[7] J. M. Cole, D. R. Symes, N. C. Lopes, J. C. Wood, K. Poder, S. Alatabi, S. W. Botchway, P. S. Foster, S. Gratton, S. Johnson, C. Kamperidis, O. Kononenko, M. De Lazzari, C. A. J. Palmer, D. Rusby, J. Sanderson, M. Sandholzer, G. Sarri, Z. Szoke-Kovacs, L. Teboul, J. M. Thompson, J. R. Warwick, H. Westerberg, M. A. Hill, D. P. Norris, S. P. D. Mangles, and Z. Najmudin, "High-resolution μct of a mouse embryo using a compact laser-driven x-ray betatron source," *Proceedings of the National Academy of Sciences*, vol. 115, p. 6335–6340, Jun 2018.

[8] S. V. Bulanov and V. S. Khoroshkov, "Feasibility of using laser ion accelerators in proton therapy," *Plasma Physics Reports*, vol. 28, no. 5, 2002.

[9] Z. Sun, "Review: Production of nuclear medicine radioisotopes with ultra-intense lasers," *AIP Advances*, vol. 11, p. 040701, Apr 2021.

[10] A. E. Siegman, *Lasers*. University Science Books, 1986.

[11] U. Morgner, F. X. Kärtner, S. H. Cho, Y. Chen, H. A. Haus, J. G. Fujimoto, E. P. Ippen, V. Scheuer, G. Angelow, and T. Tschudi, "Sub-two-cycle pulses from a kerr-lens mode-locked ti:sapphire laser," *Optics Letters*, vol. 24, p. 411, Mar 1999.

[12] "https://www.lle.rochester.edu/index.php/1985/03/01/chirped-pulse-amplification/." Accessed: 2023-01-15.

[13] D. Strickland and G. Mourou, "Compression of amplified chirped optical pulses," *Optics Communications*, vol. 56, no. 3, 1985.

[14] A. Dubietis, G. Jonušauskas, and A. Piskarskas, "Powerful femtosecond pulse generation by chirped and stretched pulse parametric amplification in bbo crystal," *Optics Communications*, vol. 88, p. 437–440, Apr 1992.

[15] "https://zeus.engin.umich.edu/about/laser-system/." Accessed: 2023-03-12.

[16] D. M. Pennington, M. D. Perry, B. C. Stuart, R. D. Boyd, J. A. Britten, C. G. Brown, S. M. Herman, J. L. Miller, H. T. Nguyen, B. W. Shore, G. L. Tietbohl, and V. P. Yanovsky, "Petawatt laser system," in *Second International Conference on Solid State Lasers for Application to ICF* (M. L. Andre, ed.), (Paris, France), p. 490–500, Dec 1997.

[17] E. W. Gaul, M. Martinez, J. Blakeney, A. Jochmann, M. Ringuette, D. Hammond, T. Borger, R. Escamilla, S. Douglas, W. Henderson, G. Dyer, A. Erlandson, R. Cross, J. Caird, C. Ebbers, and T. Ditmire, "Demonstration of a 11 petawatt laser based on a hybrid optical parametric chirped pulse amplification/mixed nd:glass amplifier," *Applied Optics*, vol. 49, p. 1676, Mar 2010.

[18] E. Sistrunk, T. Spinka, A. Bayramian, S. Betts, R. Bopp, S. Buck, K. Charron, J. Cupal, R. Deri, M. Drouin, A. Erlandson, E. S. Fulkerson, J. Horner, J. Horacek, J. Jarboe, K. Kasl, D. Kim, E. Koh, L. Koubikova, R. Lanning, W. Maranville, C. Marshall, D. Mason, J. Menapace, P. Miller, P. Mazurek, A. Naylon, J. Novak, D. Peceli, P. Rosso, K. Schaffers, D. Smith, J. Stanley, R. Steele, S. Telford, J. Thoma, D. VanBlarcom, J. Weiss, P. Wegner, B. Rus, and C. Haefner, "All diode-pumped, high-repetition-rate advanced petawatt laser system (hapls)," in *Conference on Lasers and Electro-Optics*, (San Jose, California), p. STh1L.2, OSA, 2017.

[19] P. F. Moulton, "Spectroscopic and laser characteristics of ti:al2o3," *Optical Society of America, Journal, B: Optical Physics*, vol. 3, no. 1, p. 125–133, 1986.

[20] N. A. of Sciences Engineering and Medicine, *Opportunities in Intense Ultrafast Lasers: Reaching for the Brightest Light*. Washington, DC: The National Academies Press, 2018.

[21] A. Bayramian, P. Armstrong, E. Ault, R. Beach, C. Bibeau, J. Caird, R. Campbell, B. Chai, J. Dawson, C. Ebbers, A. Erlandson, Y. Fei, B. Freitas, R. Kent, Z. Liao, T. Ladran, J. Menapace, B. Molander, S. Payne, N. Peterson, M. Randles, K. Schaffers, S. Sutton, J. Tassano, S. Telford, and E. Utterback, "The mercury project: A high average power, gas-cooled laser for inertial fusion energy development," *Fusion Science and Technology*, vol. 52, p. 383–387, Oct 2007.

[22] A. Bayramian, S. Aceves, T. Anklam, K. Baker, E. Bliss, C. Boley, A. Bullington, J. Caird, D. Chen, R. Deri, M. Dunne, A. Erlandson, D. Flowers, M. Henesian, J. Latkowski, K. Manes, W. Molander, E. Moses, T. Piggott, S. Powers, S. Rana, S. Rodriguez, R. Sawicki, K. Schaffers, L. Seppala, M. Spaeth, S. Sutton, and S. Telford, "Compact, efficient laser systems required for laser inertial fusion energy," *Fusion Science and Technology*, vol. 60, p. 28–48, Jul 2011.

[23] C. Guo and S. C. Singh, eds., *Handbook of Laser Technology and Applications: Laser Design and Laser Systems*, vol. 2. Milton: Taylor & Francis Group, 2nd ed., 2021.

[24] K. Nakamura, H.-S. Mao, A. J. Gonsalves, H. Vincenti, D. E. Mittelberger, J. Daniels, A. Magana, C. Toth, and W. P. Leemans, "Diagnostics, control and performance parameters for the bella high repetition rate petawatt class laser," *IEEE Journal of Quantum Electronics*, vol. 53, p. 1–21, Aug 2017.

[25] G. Mourou, B. Brocklesby, T. Tajima, and J. Limpert, "The future is fibre accelerators," *Nature Photonics*, vol. 7, p. 258–261, Apr 2013.

[26] S. Backus, M. Kirchner, R. Lemons, C. Durfee, and M. Murnane, "Direct diode pumped ti:sapphire ultrafast regenerative amplifier system," *Optics Express*, vol. 25, no. 4, p. 3666, 2017.

[27] A. Giesen and J. Speiser, "Fifteen years of work on thin-disk lasers: Results and scaling laws," *IEEE Journal of Selected Topics in Quantum Electronics*, vol. 13, p. 598–609, May 2007.

[28] C. J. Saraceno, F. Emaury, C. Schriber, A. Diebold, M. Hoffmann, M. Golling, T. Südmeyer, and U. Keller, "Toward millijoule-level high-power ultrafast thin-disk oscillators," *IEEE Journal of Selected Topics in Quantum Electronics*, vol. 21, p. 106–123, Jan 2015.

[29] Y. Wang, H. Chi, C. Baumgarten, K. Dehne, A. R. Meadows, A. Davenport, G. Murray, B. A. Reagan, C. S. Menoni, and J. J. Rocca, "1.1 j yb:yag picosecond laser at 1 khz repetition rate," *Optics Letters*, vol. 45, p. 6615, Dec 2020.

[30] E. F. Sistrunk, D. A. Alessi, A. J. Bayramian, K. Chesnut, A. C. Erlandson, T. C. Galvin, D. Gibson, H. Nguyen, B. Reagan, K. I. Schaffers, C. W. Siders, T. M. Spinka, and C. Haefner, "Laser technology development for high peak power lasers achieving kilowatt average power and beyond," in *Short-pulse High-energy Lasers and Ultrafast Optical Technologies* (C. L. Haefner and P. Bakule, eds.), (Prague, Czech Republic), p. 5, SPIE, Apr 2019.

[31] I. Tamer, B. A. Reagan, T. Galvin, F. Batysta, E. Sistrunk, D. Willard, A. Church, H. Neurath, J. Galbraith, G. Huete, and T. Spinka, "1 gw peak power and 100 j pulsed operation of a diode-pumped tm:ylf laser," *Optics Express*, vol. 30, p. 46336, Dec 2022.

[32] T. C. Galvin, A. J. Bayramian, K. D. Chesnut, A. Erlandson, C. W. Siders, E. Sistrunk, T. M. Spinka, and C. Haefner, "Scaling of petawatt-class lasers to multi-khz repetition rates," in *High-Power, High-Energy, and High-Intensity Laser Technology IV* (T. J. Butcher and J. Hein, eds.), (Prague, Czech Republic), p. 1, SPIE, Apr 2019.

[33] E. A. Shcherbakov, V. V. Fomin, A. A. Abramov, A. A. Ferin, D. V. Mochalov, and V. P. Gapontsev, "Industrial grade 100 kw power cw fiber laser," in *Advanced Solid-State Lasers Congress*, (Paris), p. ATh4A.2, OSA, 2013.

[34] H. Stark, J. Buldt, M. Müller, A. Klenke, and J. Limpert, "1 kw, 10 mj, 120 fs coherently combined fiber cpa laser system," *Optics Letters*, vol. 46, p. 969–972, Mar 2021.

[35] S. Chen, *Spectral and Temporal Control of Broadband Pulses to Enable Multi-TW Peak Power Coherently-combined Fiber Laser Arrays*. PhD thesis, University of Michigan, 2021.

[36] A. Brignon, *Coherent laser beam combining*. John Wiley & Sons, 2013.

[37] T. Fan, "Laser beam combining for high-power, high-radiance sources," *IEEE Journal of Selected Topics in Quantum Electronics*, vol. 11, p. 567–577, May 2005.

[38] M. Müller, *The Scaling Limits of Beam-Splitter-Based Coherent Beam Combining*. PhD thesis, Friedrich Schiller University Jena, 2020.

[39] I. Fsaifes, L. Daniault, S. Bellanger, M. Veinhard, J. Bourderionnet, C. Larat, E. Lallier, E. Durand, A. Brignon, and J.-C. Chanteloup, "Coherent beam combining of 61 femtosecond fiber amplifiers," *Optics Express*, vol. 28, p. 20152, Jul 2020.

[40] S. Chen, T. Zhou, Q. Du, D. Wang, A. Gilardi, J.-L. Vay, D. Li, J. van Tilborg, C. Schroeder, E. Esarey, R. Wilcox, and C. Geddes, "Broadband spectral combining of three pulse-shaped fiber amplifiers with 42fs compressed pulse duration," *Optics Express*, vol. 31, p. 12717, Apr 2023.

[41] D. N. Schimpf, J. Limpert, and A. Tünnermann, "Controlling the influence of spm in fiber-based chirped-pulse amplification systems by using an actively shaped parabolic spectrum," *Optics Express*, vol. 15, no. 25, p. 16945, 2007.

[42] N. V. Didenko, A. V. Konyashchenko, A. P. Lutsenko, and S. Y. Tenyakov, "Contrast degradation in a chirped-pulse amplifier due to generation of prepulses by postpulses," *Optics Express*, vol. 16, no. 5, p. 3178, 2008.

[43] D. N. Schimpf, E. Seise, and J. Limpert, "The impact of spectral modulations on the contrast of pulses of nonlinear chirped-pulse amplification systems," *Optics Express*, vol. 16, no. 14, 2008.

[44] G. Agrawal, *Nonlinear Fiber Optics*. Optics and Photonics, Academic Press, 3 ed., 2001.

[45] S. Webster, F. McDonald, A. Villanger, M. Soileau, E. Van Stryland, D. Hagan, B. McIntosh, W. Torruellas, J. Farroni, and K. Tankala, "Optical damage measurements for high peak power ytterbium doped fiber amplifiers," in *Boulder Damage Symposium XXXVII: Annual Symposium on Optical Materials for High Power Lasers* (G. J. Exarhos, A. H. Guenther, K. L. Lewis, D. Ristau, M. Soileau, and C. J. Stolz, eds.), (Boulder, CO), p. 599115, Oct 2005.

[46] S. Zhou, F. W. Wise, and D. G. Ouzounov, "Divided-pulse amplification of ultrashort pulses," *Optics Letters*, vol. 32, no. 7, 2007.

[47] D. G. Ouzounov, S. Zhou, C. Sinclair, and F. W. Wise, "Direct amplification of 3-ps pulses to 80 nj at 50-mhz repetition rate in large-mode-area yb-fiber," in *2007 Conference on Lasers and Electro-Optics (CLEO)*, (Baltimore, MD, USA), p. 1–2, IEEE, May 2007.

[48] Y. Zaouter, F. Guichard, L. Daniault, M. Hanna, F. Morin, C. Hönninger, E. Mottay, F. Druon, and P. Georges, "Femtosecond fiber chirped- and divided-pulse amplification system," *Optics Letters*, vol. 38, p. 106, Jan 2013.

[49] M. Kienel, A. Klenke, T. Eidam, M. Baumgartl, C. Jauregui, J. Limpert, and A. Tünnermann, "Analysis of passively combined divided-pulse amplification as an energy-scaling concept," *Optics Express*, vol. 21, p. 29031, Nov 2013.

[50] M. Kienel, A. Klenke, T. Eidam, S. Hädrich, J. Limpert, and A. Tünnermann, "Energy scaling of femtosecond amplifiers using actively controlled divided-pulse amplification," *Optics Letters*, vol. 39, p. 1049, Feb 2014.

[51] M. Kienel, M. Müller, A. Klenke, T. Eidam, J. Limpert, and A. Tünnermann, "Multidimensional coherent pulse addition of ultrashort laser pulses," *Optics Letters*, vol. 40, p. 522, Feb 2015.

[52] M. Kienel, M. Müller, A. Klenke, J. Limpert, and A. Tünnermann, "12 mj kw-class ultrafast fiber laser system using multidimensional coherent pulse addition," *Optics Letters*, vol. 41, p. 3343, Jul 2016.

[53] H. Stark, M. Müller, M. Kienel, A. Klenke, J. Limpert, and A. Tünnermann, "Electro-optically controlled divided-pulse amplification," *Optics Express*, vol. 25, Jun 2017.

[54] H. Stark, J. Buldt, M. Müller, A. Klenke, A. Tünnermann, and J. Limpert, "23 mj high-power fiber cpa system using electro-optically controlled divided-pulse amplification," *Optics Letters*, vol. 44, no. 22, p. 5529, 2019.

[55] T. Zhou, J. Ruppe, C. Zhu, I.-N. Hu, J. Nees, and A. Galvanauskas, "Coherent pulse stacking amplification using low-finesse gires-tournois interferometers," *Optics Express*, vol. 23, p. 7442, Mar 2015.

[56] J. Ruppe, S. Chen, M. Sheikhsofla, R. Wilcox, J. Nees, and A. Galvanauskas, "Multiplexed coherent pulse stacking of 27 pulses in a 4+1 gti resonator sequence," in *Lasers Congress 2016 (ASSL, LSC, LAC)*, (Boston, Massachusetts), p. AM4A.6, OSA, 2016.

[57] J. Ruppe, H. Pei, M. Sheikhsofla, S. Chen, R. Wilcox, W. Leemans, J. Nees, and A. Galvanauskas, "Coherent pulse stacking amplification – extending chirped pulse amplification by orders of magnitude," in *Conference on Lasers and Electro-Optics*, (San Jose, California), p. SM4I.1, OSA, 2017.

[58] H. Pei, J. Ruppe, S. Chen, M. Sheikhsofla, J. Nees, Y. Yang, R. Wilcox, W. Leemans, and A. Galvanauskas, "Near-complete stored energy extraction from fiber amplifiers in ultrashort ¿10mj energy pulses using coherent pulse stacking amplification (conference presentation)," in *Fiber Lasers XV: Technology and Systems* (I. Hartl and A. L. Carter, eds.), vol. 10512, p. 1051209, SPIE, 2018.

[59] D. Marcuse, "Loss analysis of single-mode fiber splices," *The Bell System Technical Journal*, vol. 56, p. 703–718, May 1977.

[60] C. R. Pollock, *Fundamentals of Optoelectronics*. Chicago, Ill.: Irwin, 1995.

[61] E. Snitzer and C. J. Koester, "Amplification in a fiber laser," *Applied Optics*, vol. 3, no. 10, p. 1182–1186, 1964.

[62] C. Jauregui, J. Limpert, and A. Tünnermann, "High-power fibre lasers," *Nature Photonics*, vol. 7, p. 861–867, Nov 2013.

[63] E. Snitzer, H. Po, F. Hakimi, R. Tumminelli, and B. McCollum, "Double clad, offset core nd fiber laser," in *Optical Fiber Sensors*, (New Orleans, LA), p. PD5, OSA, 1988.

[64] J. P. Koplow, D. A. V. Kliner, and L. Goldberg, "Single-mode operation of a coiled multimode fiber amplifier," *Optics Letters*, vol. 25, p. 442, Apr 2000.

[65] F. Jansen, F. Stutzki, H.-J. Otto, M. Baumgartl, C. Jauregui, J. Limpert, and A. Tünnermann, "The influence of index-depressions in core-pumped yb-doped large pitch fibers," *Optics Express*, vol. 18, p. 26834, Dec 2010.

[66] F. Jansen, F. Stutzki, C. Jauregui, J. Limpert, and A. Tünnermann, "Avoided crossings in photonic crystal fibers," *Optics Express*, vol. 19, p. 13578, Jul 2011.

[67] X. Ma, C. Zhu, I.-N. Hu, A. Kaplan, and A. Galvanauskas, "Single-mode chirally-coupled-core fibers with larger than 50μm diameter cores," *Optics Express*, vol. 22, p. 9206, Apr 2014.

[68] X. Ma, C.-H. Liu, G. Chang, and A. Galvanauskas, "Angular-momentum coupled optical waves in chirally-coupled-core fibers," *Optics Express*, vol. 19, p. 26515, Dec 2011.

[69] J. Limpert, F. Stutzki, F. Jansen, H.-J. Otto, T. Eidam, C. Jauregui, and A. Tünnermann, "Yb-doped large-pitch fibres: effective single-mode operation based on higher-order mode delocalisation," *Light: Science & Applications*, vol. 1, p. e8–e8, Apr 2012.

[70] E. Brockmüller, T. Lange, F. Wellmann, O. Kimmelma, T. Lowder, S. Novotny, R. Lachmayer, J. Neumann, and D. Kracht, "Development of efficient ccc-fiber-based components

for fiber lasers and amplifiers," in *Fiber Lasers XIX: Technology and Systems* (C. Jáuregui-Misas and V. R. Supradeepa, eds.), vol. 11981, p. 1198105, SPIE, 2022. Backup Publisher: International Society for Optics and Photonics.

[71] M. Chen, A. Rainville, M. Kanskar, J. Zhang, O. Kimmelma, A. Nieminen, D. Sipes, B. Schulz, C. Shollenbarger, T. Zhou, R. Wilcox, and A. Galvanauskas, "All-fiber integrated 85um core chirally-coupled core fiber high energy amplifiers for compact coherently combined laser arrays," in *Fiber Lasers XX: Technology and Systems* (V. R. Supradeepa, ed.), vol. 12400, p. 124000I, SPIE, 2023.

[72] R. Paschotta, J. Nilsson, A. Tropper, and D. Hanna, "Ytterbium-doped fiber amplifiers," *IEEE Journal of Quantum Electronics*, vol. 33, p. 1049–1056, Jul 1997.

[73] W. Koechner, *Solid-state laser engineering*. Springer series in optical sciences, New York, NY: Springer, 6th rev. and updated ed ed., 2006.

[74] R. L. Farrow, D. A. V. Kliner, G. R. Hadley, and A. V. Smith, "Peak-power limits on fiber amplifiers imposed by self-focusing," *Optics Letters*, vol. 31, p. 3423, Dec 2006.

[75] E. L. Buckland and R. W. Boyd, "Electrostrictive contribution to the intensity-dependent refractive index of optical fibers," *Optics Letters*, vol. 21, p. 1117, Aug 1996.

[76] L. M. Frantz and J. S. Nodvik, "Theory of pulse propagation in a laser amplifier," *Journal of Applied Physics*, vol. 34, p. 2346–2349, Aug 1963.

[77] M. J. Digonnet, E. Murphy-Chutorian, and D. G. Falquier, "Fundamental limitations of the mccumber relation applied to er-doped silica and other amorphous-host lasers," *IEEE Journal of Quantum Electronics*, vol. 38, p. 1629–1637, Dec 2002.

[78] J. M. Ruppe, *Theoretical and Experimental Foundations of Coherent Pulse Stacking Amplification*. PhD thesis, University of Michigan, 2017.

[79] C. R. Giles and E. Desurvire, "Modeling erbium-doped fiber amplifiers," *Journal of Lightwave Technology*, vol. 9, no. 2, p. 271, 1991.

[80] Q. Han, J. Ning, H. Zhang, and Z. Chen, "Novel shooting algorithm for highly efficient analysis of fiber raman amplifiers," *Journal of Lightwave Technology*, vol. 24, no. 4, 2006.

[81] M. Whittlesey, *Advanced Techniques for Spectral & Temporal Ultrashort Pulse Synthesis in Coherent Pulse Stacking Amplification*. PhD thesis, University of Michigan, 2022.

[82] R. Pantell, M. Digonnet, R. Sadowski, and H. Shaw, "Analysis of nonlinear optical switching in an erbium-doped fiber," *Journal of Lightwave Technology*, vol. 11, p. 1416–1424, Sep 1993.

[83] M. J. Digonnet, R. Sadowski, H. Shaw, and R. Pantell, "Experimental evidence for strong uv transition contribution in the resonant nonlinearity of doped fibers," *Journal of Lightwave Technology*, vol. 15, no. 2, 1997.

[84] J. Arkwright, P. Elango, G. Atkins, T. Whitbread, and J. Digonnet, "Experimental and theoretical analysis of the resonant nonlinearity in ytterbium-doped fiber," *Journal of Lightwave Technology*, vol. 16, p. 798–806, May 1998.

[85] C. Li, Y. Ma, X. Gao, F. Niu, T. Jiang, A. Wang, and Z. Zhang, "1 ghz repetition rate femtosecond yb:fiber laser for direct generation of carrier-envelope offset frequency," *Applied Optics*, vol. 54, p. 8350, Oct 2015.

[86] H. Pei, *High Fidelity Coherent Pulse Stacking Amplification with Intelligent System Controls*. PhD thesis, University of Michigan, 2021.

[87] D. Ristau and T. Gross, "Ion beam sputter coatings for laser technology," in *Optical Systems Design 2005* (C. Amra, N. Kaiser, and H. A. Macleod, eds.), (Jena, Germany), p. 596313, Sep 2005.

[88] R. Uberna, A. Bratcher, and B. G. Tiemann, "Coherent polarization beam combination," *IEEE Journal of Quantum Electronics*, vol. 46, p. 1191–1196, Aug 2010.

[89] T. Zhou, T. Sano, and R. Wilcox, "Coherent combination of ultrashort pulse beams using two diffractive optics," *Optics Letters*, vol. 42, p. 4422, Nov 2017.

[90] E. Seise, A. Klenke, J. Limpert, and A. Tünnermann, "Coherent addition of fiber-amplified ultrashort laser pulses," *Optics Express*, vol. 18, p. 27827, Dec 2010.

[91] A. A. Ishaaya, N. Davidson, L. Shimshi, and A. A. Friesem, "Intracavity coherent addition of gaussian beam distributions using a planar interferometric coupler," *Applied Physics Letters*, vol. 85, p. 2187–2189, Sep 2004.

[92] M. Müller, C. Aleshire, J. Buldt, H. Stark, C. Grebing, A. Klenke, and J. Limpert, "Scaling potential of beam-splitter-based coherent beam combination," *Optics Express*, vol. 29, p. 27900, Aug 2021.

[93] S. J. McNaught, P. A. Thielen, L. N. Adams, J. G. Ho, A. M. Johnson, J. P. Machan, J. E. Rothenberg, C.-C. Shih, D. M. Shimabukuro, M. P. Wacks, M. E. Weber, and G. D. Goodno, "Scalable coherent combining of kilowatt fiber amplifiers into a 2.4-kw beam," *IEEE Journal of Selected Topics in Quantum Electronics*, vol. 20, p. 174–181, Sep 2014.

[94] T. Zhou, Q. Du, T. Sano, R. Wilcox, and W. Leemans, "Two-dimensional combination of eight ultrashort pulsed beams using a diffractive optic pair," *Optics Letters*, vol. 43, p. 3269, Jul 2018.

[95] D. Wang, Q. Du, T. Zhou, D. Li, and R. Wilcox, "Stabilization of the 81-channel coherent beam combination using machine learning," *Optics Express*, vol. 29, p. 5694, Feb 2021.

[96] Q. Du, D. Wang, T. Zhou, A. Gilardi, M. Kiran, B. Mohammed, D. Li, and R. Wilcox, "Experimental beam combining stabilization using machine learning trained while phases drift," *Optics Express*, vol. 30, p. 12639, Apr 2022.

[97] G. D. Goodno, C.-C. Shih, and J. E. Rothenberg, "Perturbative analysis of coherent combining efficiency with mismatched lasers," *Optics Express*, vol. 18, p. 25403, Nov 2010.

[98] I. H. Malitson, "Interspecimen comparison of the refractive index of fused silica," *J. Opt. Soc. Am.*, vol. 55, no. 10, p. 1205–1209, 1965.

[99] T. Hansch and B. Couillaud, "Laser frequency stabilization by polarization spectroscopy of a reflecting reference cavity," *Optics Communications*, vol. 35, p. 441–444, Dec 1980.

[100] T. M. Shay, "Theory of electronically phased coherent beam combination without a reference beam," *Optics Express*, vol. 14, no. 25, 2006.

[101] M. A. Vorontsov, G. W. Carhart, and J. C. Ricklin, "Adaptive phase-distortion correction based on parallel gradient-descent optimization," *Optics Letters*, vol. 22, no. 12, 1997.

[102] M. A. Vorontsov and V. P. Sivokon, "Stochastic parallel-gradient-descent technique for high-resolution wave-front phase-distortion correction," *Journal of the Optical Society of America A*, vol. 15, no. 10, 1998.

[103] N. Qian, "On the momentum term in gradient descent learning algorithms," *Neural Networks*, vol. 12, p. 145–151, Jan 1999.

[104] S. B. Weiss, M. E. Weber, and G. D. Goodno, "Group delay locking of coherently combined broadband lasers," *Optics Letters*, vol. 37, no. 4, 2012.

[105] G. D. Goodno and S. B. Weiss, "Automated co-alignment of coherent fiber laser arrays via active phase-locking," *Optics Express*, vol. 20, no. 14, 2012.

[106] M. Müller, C. Aleshire, A. Klenke, E. Haddad, F. Légaré, A. Tünnermann, and J. Limpert, "10.4 kw coherently combined ultrafast fiber laser," *Optics Letters*, vol. 45, p. 3083, Jun 2020.

[107] D. Allan, "Statistics of atomic frequency standards," *Proceedings of the IEEE*, vol. 54, no. 2, p. 221–230, 1966.

[108] N. J. Peskosky, *Tabletop Fast Neutron Sources Driven by High Repetition Rate Ultrashort Laser Systems*. PhD thesis, University of Michigan, 2023.

[109] N. Basov, P. Kriukov, S. Zakharov, Y. Senatsky, and S. Tchekalin, "Experiments on the observation of neutron emission at a focus of high-power laser radiation on a lithium deuteride surface," *IEEE Journal of Quantum Electronics*, vol. 4, p. 864–867, Nov 1968.

[110] M. J. Rosenberg, A. B. Zylstra, F. H. Séguin, H. G. Rinderknecht, J. A. Frenje, M. Gatu Johnson, H. Sio, C. J. Waugh, N. Sinenian, C. K. Li, R. D. Petrasso, P. W. McKenty, M. Hohenberger, P. B. Radha, J. A. Delettrez, V. Y. Glebov, R. Betti, V. N. Goncharov, J. P. Knauer, T. C. Sangster, S. LePape, A. J. Mackinnon, J. Pino, J. M. McNaney, J. R. Rygg, P. A. Amendt, C. Bellei, L. R. Benedetti, L. Berzak Hopkins, R. M. Bionta, D. T. Casey, L. Divol, M. J. Edwards, S. Glenn, S. H. Glenzer, D. G. Hicks, J. R. Kimbrough, O. L. Landen, J. D. Lindl, T. Ma, A. MacPhee, N. B. Meezan, J. D. Moody, M. J. Moran,

H.-S. Park, B. A. Remington, H. Robey, M. D. Rosen, S. C. Wilks, R. A. Zacharias, H. W. Herrmann, N. M. Hoffman, G. A. Kyrala, R. J. Leeper, R. E. Olson, J. D. Kilkenny, and A. Nikroo, "Investigation of ion kinetic effects in direct-drive exploding-pusher implosions at the nif," *Physics of Plasmas*, vol. 21, p. 122712, Dec 2014.

[111] J. Alvarez, J. Fernández-Tobias, K. Mima, S. Nakai, S. Kar, Y. Kato, and J. Perlado, "Laser driven neutron sources: Characteristics, applications and prospects," *Physics Procedia*, vol. 60, p. 29–38, 2014.

[112] V. Kononov, M. Bokhovko, O. Kononov, N. Soloviev, W. Chu, and D. Nigg, "Accelerator-based fast neutron sources for neutron therapy," *Nuclear Instruments and Methods in Physics Research Section A: Accelerators, Spectrometers, Detectors and Associated Equipment*, vol. 564, p. 525–531, Aug 2006.

[113] R. Mukundan and R. L. Borup, "Visualising liquid water in pem fuel cells using neutron imaging," *Fuel Cells*, vol. 9, p. 499–505, Oct 2009.

[114] J. Krása and D. Klír, "Scaling of laser fusion experiments for dd-neutron yield," *Frontiers in Physics*, vol. 8, p. 310, Sep 2020.

[115] I. Prencipe, J. Fuchs, S. Pascarelli, D. W. Schumacher, R. B. Stephens, N. B. Alexander, R. Briggs, M. Büscher, M. O. Cernaianu, A. Choukourov, M. De Marco, A. Erbe, J. Fassbender, G. Fiquet, P. Fitzsimmons, C. Gheorghiu, J. Hund, L. G. Huang, M. Harmand, N. J. Hartley, A. Irman, T. Kluge, Z. Konopkova, S. Kraft, D. Kraus, V. Leca, D. Margarone, J. Metzkes, K. Nagai, W. Nazarov, P. Lutoslawski, D. Papp, M. Passoni, A. Pelka, J. P. Perin, J. Schulz, M. Smid, C. Spindloe, S. Steinke, R. Torchio, C. Vass, T. Wiste, R. Zaffino, K. Zeil, T. Tschentscher, U. Schramm, and T. E. Cowan, "Targets for high repetition rate laser facilities: needs, challenges and perspectives," *High Power Laser Science and Engineering*, vol. 5, p. e17, 2017.

[116] A. Schwemmlein, C. Stoeckl, C. Forrest, W. Shmayda, S. Regan, and W. Schröder, "First demonstration of a triton beam using target normal sheath acceleration," *Nuclear Instruments and Methods in Physics Research Section B: Beam Interactions with Materials and Atoms*, vol. 522, p. 27–31, Jul 2022.

[117] J. Hah, G. M. Petrov, J. A. Nees, Z.-H. He, M. D. Hammig, K. Krushelnick, and A. G. R. Thomas, "High repetition-rate neutron generation by several-mj, 35 fs pulses interacting with free-flowing d2o," *Applied Physics Letters*, vol. 109, p. 144102, Oct 2016.

[118] J. T. Morrison, S. Feister, K. D. Frische, D. R. Austin, G. K. Ngirmang, N. R. Murphy, C. Orban, E. A. Chowdhury, and W. M. Roquemore, "Mev proton acceleration at khz repetition rate from ultra-intense laser liquid interaction," *New Journal of Physics*, vol. 20, p. 022001, Feb 2018.

[119] B. Aharmim, S. Ahmed, A. Anthony, N. Barros, E. Beier, A. Bellerive, B. Beltran, M. Bergevin, S. Biller, R. Bonventre, K. Boudjemline, M. Boulay, B. Cai, E. Callaghan, J. Caravaca, Y. Chan, D. Chauhan, M. Chen, B. Cleveland, G. Cox, R. Curley, X. Dai, H. Deng, F. Descamps, J. Detwiler, P. Doe, G. Doucas, P.-L. Drouin, M. Dunford, S. Elliott,

H. Evans, G. Ewan, J. Farine, H. Fergani, F. Fleurot, R. Ford, J. Formaggio, N. Gagnon, K. Gilje, J. Goon, K. Graham, E. Guillian, S. Habib, R. Hahn, A. Hallin, E. Hallman, P. Harvey, R. Hazama, W. Heintzelman, J. Heise, R. Helmer, A. Hime, C. Howard, M. Huang, P. Jagam, B. Jamieson, N. Jelley, M. Jerkins, C. Kéfélian, K. Keeter, J. Klein, L. Kormos, M. Kos, A. Krüger, C. Kraus, C. Krauss, T. Kutter, C. Kyba, B. Land, R. Lange, J. Law, I. Lawson, K. Lesko, J. Leslie, I. Levine, J. Loach, R. MacLellan, S. Majerus, H. Mak, J. Maneira, R. Martin, A. Mastbaum, N. McCauley, A. McDonald, S. McGee, M. Miller, B. Monreal, J. Monroe, B. Nickel, A. Noble, H. O'Keeffe, N. Oblath, C. Okada, R. Ollerhead, G. Orebi Gann, S. Oser, R. Ott, S. Peeters, A. Poon, G. Prior, S. Reitzner, K. Rielage, B. Robertson, R. Robertson, M. Schwendener, J. Secrest, S. Seibert, O. Simard, D. Sinclair, P. Skensved, T. Sonley, L. Stonehill, G. Tešić, N. Tolich, T. Tsui, R. Van Berg, B. VanDevender, C. Virtue, B. Wall, D. Waller, H. Wan Chan Tseung, D. Wark, J. Wendland, N. West, J. Wilkerson, J. Wilson, T. Winchester, A. Wright, M. Yeh, F. Zhang, K. Zuber, and S. Collaboration, "Cosmogenic neutron production at the sudbury neutrino observatory," *Physical Review D*, vol. 100, p. 112005, Dec 2019.

[120] T. Marchi, F. Pino, C. L. Fontana, A. Quaranta, E. Zanazzi, M. Vesco, M. Cinausero, N. Daldosso, V. Paterlini, F. Gramegna, S. Moretto, G. Collazuol, M. Degerlier, D. Fabris, and S. M. Carturan, "Optical properties and pulse shape discrimination in siloxane-based scintillation detectors," *Scientific Reports*, vol. 9, p. 9154, Jun 2019.

[121] I. H. Hutchinson, *Principles of plasma diagnostics*. Cambridge; New York: Cambridge University Press, 2nd ed ed., 2002.

[122] S. Le Pape, Y. Y. Tsui, A. Macphee, D. Hey, P. Patel, A. Mackinnon, M. Key, M. Wei, T. Ma, F. N. Beg, R. Stephens, K. Akli, T. Link, L. Van-Woerkom, and R. R. Freeman, "Characterization of the preformed plasma for high-intensity laser-plasma interaction," *Optics Letters*, vol. 34, p. 2997, Oct 2009.

[123] M. C. Kaluza, M. I. K. Santala, J. Schreiber, G. D. Tsakiris, and K. J. Witte, "Time-sequence imaging of relativistic laser–plasma interactions using a novel two-color probe pulse," *Applied Physics B*, vol. 92, p. 475–479, Sep 2008.

[124] Z. E. Davidson, B. Gonzalez-Izquierdo, A. Higginson, K. L. Lancaster, S. D. R. Williamson, M. King, D. Farley, D. Neely, P. McKenna, and R. J. Gray, "An optically multiplexed single-shot time-resolved probe of laser–plasma dynamics," *Optics Express*, vol. 27, p. 4416, Feb 2019.

[125] T. Ma, D. Mariscal, R. Anirudh, T. Bremer, B. Z. Djordjevic, T. Galvin, E. Grace, S. Herriot, S. Jacobs, B. Kailkhura, R. Hollinger, J. Kim, S. Liu, J. Ludwig, D. Neely, J. J. Rocca, G. G. Scott, R. A. Simpson, B. S. Spears, T. S. Spinka, K. Swanson, J. J. Thiagarajan, B. Van Essen, S. Wang, S. C. Wilks, G. J. Williams, J. Zhang, M. C. Herrmann, and C. Haefner, "Accelerating the rate of discovery: toward high-repetition-rate hed science," *Plasma Physics and Controlled Fusion*, vol. 63, p. 104003, Oct 2021.

[126] S. Dowling, "Harold edgerton: The man who froze time," *BBC Future*, 2014.

[127] C. Bernert, S. Assenbaum, F.-E. Brack, T. E. Cowan, C. B. Curry, M. Garten, L. Gaus, M. Gauthier, S. Göde, I. Goethel, S. H. Glenzer, T. Kluge, S. Kraft, F. Kroll, M. Kuntzsch, J. Metzkes-Ng, M. Loeser, L. Obst-Huebl, M. Rehwald, H.-P. Schlenvoigt, C. Schoenwaelder, U. Schramm, M. Siebold, F. Treffert, T. Ziegler, and K. Zeil, "Off-harmonic optical probing of high intensity laser plasma expansion dynamics in solid density hydrogen jets," *Scientific Reports*, vol. 12, p. 7287, May 2022.

[128] S. Patankar, E. T. Gumbrell, T. S. Robinson, H. F. Lowe, S. Giltrap, C. J. Price, N. H. Stuart, P. Kemshall, J. Fyrth, J. Luis, J. W. Skidmore, and R. A. Smith, "Multiwavelength interferometry system for the orion laser facility," *Applied Optics*, vol. 54, p. 10592, Dec 2015.

[129] S. Feister, J. A. Nees, J. T. Morrison, K. D. Frische, C. Orban, E. A. Chowdhury, and W. M. Roquemore, "A novel femtosecond-gated, high-resolution, frequency-shifted shearing interferometry technique for probing pre-plasma expansion in ultra-intense laser experiments," *Review of Scientific Instruments*, vol. 85, p. 11D602, Nov 2014.

[130] T. Ziegler, M. Rehwald, L. Obst, C. Bernert, F.-E. Brack, C. B. Curry, M. Gauthier, S. H. Glenzer, S. Göde, L. Kazak, S. D. Kraft, M. Kuntzsch, M. Loeser, J. Metzkes-Ng, C. Rödel, H.-P. Schlenvoigt, U. Schramm, M. Siebold, J. Tiggesbäumker, S. Wolter, and K. Zeil, "Optical probing of high intensity laser interaction with micron-sized cryogenic hydrogen jets," *Plasma Physics and Controlled Fusion*, vol. 60, p. 074003, Jul 2018.

[131] P. Sidorenko, W. Fu, and F. Wise, "Nonlinear ultrafast fiber amplifiers beyond the gain-narrowing limit," *Optica*, vol. 6, p. 1328, Oct 2019.

[132] P. Sidorenko and F. Wise, "Generation of 1 μj and 40 fs pulses from a large mode area gain-managed nonlinear amplifier," *Optics Letters*, vol. 45, p. 4084, Jul 2020.

[133] "Snlo nonlinear optics code available from a. v. smith, as-photonics, albuquerque, nm."

[134] F. Batysta, R. Antipenkov, J. T. Green, J. A. Naylon, J. Novák, T. Mazanec, P. Hříbek, C. Zervos, P. Bakule, and B. Rus, "Pulse synchronization system for picosecond pulse-pumped opcpa with femtosecond-level relative timing jitter," *Optics Express*, vol. 22, p. 30281, Dec 2014.